Universidade Federal do Rio de Janeiro
Centro de Ciências Matemáticas e da Natureza
Observatório do Valongo

Ph.D. thesis

Alvaro Silva Iribarrem

Relativistic Cosmology Number Densities in Void-Lemaître-Tolman-Bondi Models

Supervisors: Marcelo Byrro Ribeiro & Paola Andreani

2013

Alvaro Silva Iribarrem

Relativistic Cosmology Number Densities in Void-Lemaître-Tolman-Bondi Models

Tese de Doutorado apresentada ao Programa de Pós-graduação em Astronomia do Observatório do Valongo, Universidade Federal do Rio de Janeiro, como requisito parcial à obtenção do título de Doutor em Astronomia.

Orientadores: Prof. Dr. Marcelo Byrro Ribeiro & Dra. Paola Andreani

Rio de Janeiro
Setembro de 2013

Iribarrem, Alvaro S.

Relativistic cosmology number densities
in void-Lemaitre-Tolman-Bondi (LTB) models/ Alvaro Silva Iribarrem- Rio de Janeiro: UFRJ/ OV, 2013

xii, 62f.:il; 30 cm

Orientadores: Marcelo Byrro Ribeiro, Paola Andreani

Tese (Doutorado em Astronomia) - UFRJ/ OV/ Programa de
Pós-graduação em Astronomia, 2013.

Referências Bibliográficas: f: 75-77.

1.Galáxias: distâncias e desvios para o vermelho 2.Cosmologia: teoria
3.Galáxias: evolução 4.Infravermelho: galáxias I. Ribeiro, Marcelo B., Andreani, Paola
II. Universidade Federal do Rio de Janeiro, Observatório do Valongo,
Programa de Pós-graduação em Astronomia, 2013 III. Título.

Abstract

The goal of this work is to compute the number density of far-infrared selected galaxies in both the comoving frame and along the observer's past lightcone of a "giant void" Lemaître-Tolman-Bondi dust model and to compare those results with their counterparts in the standard model of Cosmology, that is, the Friedmann-Lemaître-Robertson-Walker metric with a perfect fluid energy-momentum tensor and a non-vanishing cosmological constant Λ.

We use the blind-selected far-infrared catalogues built on the observations performed with the PACS (*Photodetector Array Camera & Spectrometer*) instrument, onboard the *Herschel* space telescope, as part of the PEP (*PACS evolutionary probe*) survey. Schechter profiles were obtained in redshift bins up to $z \approx 4$, assuming comoving volumes in both the standard and void models, parametrised to fit the current combination of results stemming from the observations of supernovae Ia, the cosmic microwave background radiation, and baryonic acoustic oscillations. We obtained selection functions and defined "consistency functions", from which we computed the differential and integral densities assuming various cosmological distances. We used the Kolmogorov-Smirnov statistics to study the evolution of the consistency functions and its connection to that of the comoving density of sources.

We found that the luminosity functions computed assuming both the standard and void models show in general good agreement. However, the faint-end slope in the void models shows a significant departure from the standard model up to redshift 0.4. We demonstrate that this result is not artificially caused by the LF estimator used, which turns out to be robust under the differences in matter-energy density profiles of the models. The differences found in the LF slopes at the faint-end are due to the variation in the source luminosities, which depend on the geometrical part of the model. It follows that there is a discrepancy between the results found in the standard cosmological model and those in the vold models studied here, with the comoving number density of faint sources smaller in these latter ones then in the former.

Also, we observed similar power-law patterns in the number densities along the past light cone in the void models as the ones found in past works assuming the standard model line element. This could indicate that the observational inhomogeneities found in the past lightcone of both cosmologies are a very general feature, closely related to the expanding spacetimes.

Resumo

O objetivo desse trabalho é calcular a densidade numérica de galáxias selecionadas no infravermelho distante, tanto no referencial comóvel quanto ao longo do cone de luz passado em um modelo de poeira em uma cosmologia de Lemaître-Tolman-Bondi do tipo "vazio gigante", e comparar tais resultados com seus análogos no modelo padrão da cosmologia.

Usamos os catálogos de objetos selecionados por fluxo no infravermelho profundo construídos a partir de observações feitas com o instrumento PACS (*Photodetector Array Camera & Spectrometer*) a bordo do telescópio espacial *Herschel*, como parte do levantamento PEP (*PACS evolutionary probe*). Perfis de Schechter foram obtidos em intervalos de desvio para o vermelho até $z \approx 4$, assumindo volumes comóveis em ambos os modelos padrão e de vazio, parametrizados para ajustar a presente combinação de resultados advindos de observações de supernovas Ia, da radiação cósmica de fundo, e das oscilações acústicas bariônicas. Nós obtemos funções de seleção e definimos "funções de consistência", a partir das quais computamos as densidades diferenciais e integrais supondo várias distâncias cosmológicas. Usamos a estatística de Kolmogorov-Smirnov para estudar a evolução das funções de consistência e sua conexão com a evolução da densidade comóvel.

Concluímos que as funções de luminosidade (FL) calculadas supondo ambos o modelo padrão e o modelo de vazio demostram uma boa concordância em geral. No entanto, a inclinação da parte de baixa luminosidade nos modelos de vazio mostram um significativo descolamento daquela obtida com o modelo padrão, até o desvio para o vermelho 0.4. Nós demonstramos que esse resultado não é causado artificialmente pelo estimador da FL utilizado, que se mostrou robusto quando às diferenças nos perfis de matéria-energia presentes nos modelos. As diferenças encontradas nas inclinações das FL em baixas luminosidades são devidas a variações na luminosidade das fontes, que depende da parte geométrica do modelo. Sendo assim, há uma discrepância entre os resultados encontrados com o modelo padrão e aqueles usando os modelos de vazio estudados aqui, com a densidade numérica comóvel de fontes de baixa luminosidade menores nos segundos, em relação ao primeiro.

Também observamos padrões de lei de potência nas densidades numéricas ao longo do cone de luz passado dos modelos de vazio similares àqueles encontrados em trabalhos passados supondo o elemento de linha do modelo padrão. Isso poderia indicar que as não-homogeneidades encontradas no cone de luz passado em ambas as cosmologias são uma característica bastante geral, intimamente relacionadas aos espaço-tempos em expansão.

Acknowledgements

When I first met Margherita Bonzini, my office mate at the ESO Headquarters in Garching, I told her I was a lucky guy. Indeed, that was how I felt back then, and it never changed. I have many reasons to feel lucky: On top of the list of all the amazing people I could thank in the dissertation for my MSc. degree, I also made so many wonderful new friendships during the course of my Ph.D., without whom these last three years wouldn't have been nearly as bright, productive, and intense as they were. I am indeed very lucky for having that many special people to thank for. In what follows I'll focus only on these recent years: all that I wrote in my dissertation surely still applies, and I feel it properly acknowledges all the support I had up to that point. I will also switch between English and Portuguese. I wish I could write in German, French, Spanish, Italian, and even Mandarin as well, but I'll have to do with only the first two.

Primeiro e mais importante, à minha famlia próxima, de sangue ou de escolha. A minha mãe, Maria Angélica Nascimento Silva, por todas as boas risadas que me proporcionou com sua incrível capacidade de farejar minha presença virtual, mesmo estando do outro lado do Oceano Atlântico. A minha irmã, Iasmim Iribarrem, por continuar sendo a única pessoa a me dizer as verdades que eu precisei ouvir, da maneira que precisavam ser ditas. A Letícia Dutra Ferreira, pela ótima convivência nos quase dois anos que dividimos apartamento em Garching, pela parceria e pela amizade infalíveis. A Bernardo Baeta Neves Strassburg por me acolher no difícil período de readaptação ao modo de vida no Rio, por acreditar na minha capacidade de dar uma contribuição real e relevante aos projetos do Instituto Internacional para a Sustentabilidade e, finalmente, por me fazer voltar a acreditar no nosso poder de mudar o mundo.

To the ones closest to a family I had in Munich: Guillaume Drouart, for the strategically-placed flat near the Theresienwiese where I could, and did, crash after almost every bierfest Munich had in the past couple of years – that is true friendship! Also, for organizing the board game sessions, and for all the great conversations, ranging from geek topics like Animes and videogames to language, politics, philosophy, fiction, and back to the geekness – many of those, probably the most epic ones, had together with Pierre-Yves Lablanche. To Oscar Gonzalez and João da Silva, my

"rat-pack brothers", for all the good laughs we had at the expense of, well, almost everything. To Anna Feltre for being the true heart of our group of friends, with her absolutely irresistible ability to keep everyone's spirits high; and Nora Lützgendorf, for having always been there for me, no matter the size or nature of the issue, and for proving me a german person can sing in Portuguese with perfect brazilian accent if they are motivated enough.

To the great friends I have made or interacted in a meaningful way during the different stages of my Ph.D., Anäelle Maury, Andrea Ribeiro, Andressa Jendreieck, Bruna Vajgel, Carlo Manara, Cédric Collet, Claudia Lagos, Cristiano da Rocha, Dominika Wylezalek, Eduardo Penteado, Eli Bressert, Emille Ishida, Eric Lagadec, Evita Descho, Fei Zhao, Fernanda Queiroz, Gráinne Costigan, Grant Tremblay, Gustavo Henrique Dopke, Guto Correia, Kate Maguire, Leo Huckvale, Lisa Nortmann, Lucas Werneck, Luis Calada, Marcelo Ferreira, Margherita Bonzini, Mariana Januzzi, Mark Westmosquette, Mathieu Isidro, Merrill Scott, Neale Gibson, Nuno Gomes, Peter Scicluna, Rafael Souza, Raquel Yumi Shida, Raul Lopes, Robbin Blokpoel, Sebastian Daemgen, Steve Longmore, Theo Chousinho, Tim Davis, and Ulli Kuchner for all the truly awesome moments we shared.

To both my supervisors, Paola Andreani and Marcelo B. Ribeiro, for their remarkable dedication in guiding me through the process of producing this work, from taking time to hold weekly meetings, to actually sitting with me and discussing even the particular equations and numerical codes I was developing. I wholeheartedly salute you.

To Carlotta Gruppioni, for hosting me for a week at the INAF-Bologna, patiently helping me with the most intricate details of the computation of the luminosity functions used throughout this work. To Amanda R. Lopes, Sean February, Stefano Berta, and William R. Stoeger for their essential contributions to many aspects of the papers on which this thesis is based.

To the staff at the ESO Headquarters with whom I have interacted during my studentship, Bruno Leibundgut, Dietrich Baade, Eric Emsellem, Ferdinando Patat, Jason Spyromilio, Jochen Liske, Michael Hilker, and Nadine Neumayer, for the broad, fertile, and cooperative academic environment they helped to create and maintain.

Finalmente, a Helio Jacques Rocha Pinto, Heloísa Boechat e Silvia Lorenz Martins, por seus papéis fundamentais na estruturação do programa de Doutorado do Observatório do Valongo, que me permitiu continuar a linha de pesquisa que desenvolvi no mestrado.

This work was funded by both CAPES and ESO studentships.

In loving memory of
Shirley Nascimento da Silva

Summary

List of Figures

List of Tables

Introduction

It is often said that the development of General Relativity (GR) was the starting point for modern cosmology. The discovery of the radial recession velocity of extragalactic objects (Hubble 1929) is understood in the context of GR as caused by the expansion of spacetime itself. That is, in this picture the Universe's underlying geometry evolves with cosmic time, changing the way incoming light travels through the null geodesics connecting the sources to our telescopes.

The aim of many studies in observational cosmology is to infer to what extent the geometry of the spacetime contributes to the formation and evolution of the galaxies, the building blocks of the luminous Universe. In practical terms, most of what we can infer about galaxy formation and evolution comes from analyses of redshift surveys. Although the redshift is an observable quantity related to the energy content and geometry of the Universe – *regardless of how we model it* – translating these measurements into distance estimations cannot be performed without assuming a cosmological model. As a consequence, it is clear that any study that involves galaxy distances will be model dependent. This dependency cannot be overcome as long as the distance estimators used in these studies are not directly obtained, but instead derived from redshift measurements.

Results from many independent observations – Hubble parameter estimations from the distances to Cepheids (Freedman et al. 2001), or to massive, passively evolving early-type galaxies (Moresco et al. 2012; Liu et al. 2012), or to extragalactic HII regions (Chávez et al. 2012); luminosity distance-redshift relation stemming from supernovae type Ia (henceforth, simply SNe) surveys, e.g. Riess et al. (1998); Perlmutter et al. (1999); the power spectrum of the cosmic microwave background radiation (CMB), e.g. Komatsu et al. (2011); and the angular size scale obtained from baryonic accoustic oscillation (BAO) studies, e.g. Percival et al. (2010) – fit together in a coherent picture under the cold dark matter model with a non-vanishing cosmological constant (ΛCDM); (e.g. Komatsu et al. 2009), which is now adopted as the standard cosmological model.

The standard model is relatively simple in comparison to other cosmologies, and yields one of the best fits to the combined body of observations (Sollerman et al. 2009). The establishment of it allowed the above-mentioned model-dependency of

galaxy formation and evolution to be reduced to an unavoidable but otherwise less consequential fact: even if the observations depend on the cosmology, because the standard model is so precisely well-defined, it follows that the conclusions about galaxy formation and evolution that we can draw from the data by assuming this cosmology should also be accurate.

One of the observational results, arguably key in selecting the ΛCDM parametrisation for a Friedmann-Lemaître-Robertson-Walker (FLRW) perfect fluid model is the dimming in the redshift-distance relation of supernovae Ia, first obtained independently by Riess et al. (1998) and Perlmutter et al. (1999). In the standard model picture, the extra dimming observed in these standard candles' absolute magnitudes is understood as being caused by the sources being farther away then they would be if the Universe was simply expanding like in the Einstein-de Sitter model. These hypothetical larger distances could then easily be explained by an acceleration of the expansion of the Universe, which has led to the re-introduction of the cosmological constant Λ in the Einstein's field equations, and the further interpretation of it as an exotic fluid, *Dark Energy*, driving this acceleration.

The ΛCDM model still faces a few difficulties though: the coincidence problem, which stems from the lack of explanation to why the best-fit value for the cosmological constant is such that its associated energy density is presently at the same order of magnitude of the rest of the Universe's energy density; the vacuum-energy or the cosmological constant problem (Weinberg 1989), which represents a difference of 120 orders of magnitude between the value for the cosmological constant energy density predicted by the standard model of particles and the one predicted by the standard model of cosmology; a few over-predictions of galaxy counts, like the missing satellites problem (Klypin et al. 1999; Moore et al. 1999), or the more recent dynamical inconsistency in the predictions for the dark matter halo mass of the Galaxy's dwarf spheroidals (Boylan-Kolchin et al. 2012); the baryon fraction of low-mass haloes (Papastergis et al. 2012); the under-density of the local void (Tikhonov & Klypin 2009; Peebles & Nusser 2010); and the uncertainties in the characterization of the equation-of-state parameter w of Dark Energy (Sollerman et al. 2009). In addition, results from Flender & Schwarz (2012) dispute the general validity of the Newtonian perturbation theory over large cosmological volumes, with possible implications for the results obtained from the dark matter halo hierarchical trees of the N-body simulations and its application to explain the observed luminosity functions of galaxies.

Such difficulties have encouraged many authors to investigate viable alternatives to the Dark Energy scenario, like modified gravity (Tsujikawa 2010), the effect of small-scale spatial non-homogeneities of the matter content in the estimation of the cosmological model parameters (Busti & Lima 2012), often called the backreaction

effect on cosmology (Clarkson et al. 2011; Clarkson & Umeh 2011; Clifton et al. 2012; Wiegand & Schwarz 2012), or non-homogeneous cosmological models (Célérier 2007; Bolejko et al. 2011a; Ellis 2011).

Many recent works have advanced our understanding of non-homogeneities and, particularly, within the Lemaître-Tolman-Bondi (LTB) models. From practical questions like those related to possible dimming or brightening of point-like sources due to the narrowness of their observed beams, compared to the typical smoothing scales in standard model simulations (Clarkson et al. 2012), or the possibility of accounting for the anomalous primordial Lithium abundances (Regis & Clarkson 2012), passing through the development of the models themselves (e.g. Hellaby & Alfedeel 2009; Alfedeel & Hellaby 2010; Meures & Bruni 2012; Humphreys et al. 2012; Nishikawa et al. 2012; Bull & Clifton 2012; Valkenburg et al. 2012; Wang & Zhang 2012; Hellaby 2012; Fleury et al. 2013), to several tests and fits to different observations (e.g. February et al. 2010; Bolejko et al. 2011b; Hoyle et al. 2013; Bull et al. 2012; de Putter et al. 2012), much has been done to establish non-homogeneity as a well-grounded modification of the standard cosmology.

The simplest non-homogeneous model assumes an LTB metric having a pressureless (dust) energy-momentum tensor. LTB dust models yield analytical solutions to the Einstein's field equations, e.g. Bonnor (1972), that can be reduced by an appropriate parametrisation to the standard model ones. It is, for example, quite usual to set the free equations allowed in this model in a way that it reduces to the usual Einstein-de Sitter solution at large enough redshifts, enabling the model to naturally fit many CMB constraints. Regardless of the many problems this alternative model shows (Marra & Pääkkönen 2010; Moss et al. 2011; Zhang & Stebbins 2011; Zibin 2011; Planck Collaboration et al. 2013), arguably it remains the simplest and best-studied way to allow for non-homogeneities in the cosmological model.

Garcia-Bellido & Haugbølle (2008, hereafter GBH) proposed a "giant void" parametrisation for the LTB dust model that was able to simultaneously fit the SNe Ia Hubble diagram and some general features of the CMB. The GBH void model is characterised by an under-dense region of Gpc scale around the Galaxy. In it, both the matter density profile Ω_M and the transverse Hubble constant H_0 are functions of the radial coordinate r. [1]

Despite the recent interest in these models, to date no work has aimed at studying galaxy evolution in non-homogeneous cosmologies. One of the main quantities used in Astronomy to trace the evolution of sources with cosmic time is the luminosity function (LF). The luminosity function is a statistical tool to infer the formation and evolution of galaxies, usually computed with complete sets of photometric and/or spectroscopic data. To compute the luminosities of the sources from their observed

[1] See, for example, figure 1 of Zumalacárregui et al. (2012)

fluxes, a luminosity distance must be obtained from the redshift estimation, a step that requires the adoption of a cosmological model. To deal with the incompleteness due to the flux limits, the assumption of *spatial homogeneity* in the distribution is usually made. Spatial homogeneity is defined on hypersurfaces of constant time coordinate, not to be confused with *observational homogeneity* that is defined on the observer's past lightcone.

The spatial homogeneity assumption does not hold for non-homogeneous cosmologies in general. On the other hand, the precision of the current constraints on the cosmological model might be enough to yield an LF that has the same shape in all models allowed by the observations. To investigate this assertion, it is necessary to compute the LF considering one such alternative model, and perform a statistical comparison with the LF obtained assuming the standard model.

Moreover, it has been well-established by observations made at many different wavelengths (some recent examples include van der Burg et al. 2010; Ramos et al. 2011; Cool et al. 2012; Simpson et al. 2012; Patel et al. 2013; and Stefanon & Marchesini 2013), and particularly in the infrared (Babbedge et al. 2006; Caputi et al. 2007; Rodighiero et al. 2010; Magnelli et al. 2011; Heinis et al. 2013), that the LF shows significant evolution with redshift. The currently favoured theory for explaining the shape and redshift evolution of the LF is that the dark matter haloes grow up hierarchically by merging, and that baryonic matter trapped by these haloes condense to form galaxies. Astrophysical processes (gas cooling, high redshift photoionization, feedbacks), are then responsible for reproducing the shape of the luminosity function of galaxies starting from the dark matter halo mass function (Benson et al. 2003). The usual approach in the context of the standard model is either to use semi-analytical models to parameterize these (e.g. Neistein & Weinmann 2010), or to use empirical models (e.g. Yang et al. 2003; Skibba & Sheth 2009; Zehavi et al. 2011) to allocate galaxies as a function of the halo mass, both built on a dark matter hierarchical merger tree created by simulations, like the Millennium simulation (Springel et al. 2005; Boylan-Kolchin et al. 2009).

The total luminosity density, stemming directly from the LF, is a very important tool for assessing star formation rates and the global star formation history of the Universe (Kennicutt 1998; Chary & Elbaz 2001; Franceschini et al. 2001; Xu et al. 2001; Elbaz et al. 2002; Metcalfe et al. 2003; Lagache et al. 2004; Pérez-González et al. 2005; Caputi et al. 2007; Magnelli et al. 2009). It has become increasingly clear in the past few years that in order to account for the rest-frame ultra-violet light absorbed by the dust in the star formation regions it is essential to observe the rest-frame far-infrared (FIR) and sub-mm wavelengths, at which the absorbed light is re-emitted. Only by combining data from the ultra-violet to the FIR can we have a complete view of the energy budget at different epochs, and thus an unbiased

understanding of galaxy evolution. For this reason, it is very important to ascertain that any results stemming from the IR LFs are indeed independent of the underlying cosmology, and how would such results change under cosmologies still allowed by the full set of observations.

In practice the LF is traditionally computed using the comoving volume, which does not stem directly from the observations, but rather is derived from it assuming a cosmological model with a well-defined metric that translates redshifts into distances. The effects of the expanding space-like hypersurfaces can, therefore, be successfully factored out of the observations *up to the limits where the assumed cosmological model holds*.

The last remark is of special importance, because Mustapha et al. (1997) proved that any spherically symmetric set of observations, like redshift surveys, can be fitted simply by the spatial non-homogeneities in a more general cosmological model that assumes an LTB line element and a dust-like energy-momentum tensor, *regardless of any evolution of the sources*. As a consequence, the reported redshift evolution of the LF could, in principle, be caused by a non-homogeneity on the cosmology at the scale of the observations.

The original contribution of this work is based on three papers: Iribarrem et al. (2012, henceforth Paper I), Iribarrem et al. (2013b, henceforth paper II), and Iribarrem et al. (2013a, henceforth Paper III). The first part, Chapter 1, comprises a review of the key theoretical concepts in obtaining the number densities in the past lightcone of the standard model presented in the dissertation for the MSc. degree of Iribarrem (2009), and of the LTB/GBH models presented in Paper II. The text of Section 1.1 is drawn from Paper I, which is the final, published revision of the original paper resulting from that dissertation. This revision was done during the initial months of the Ph.D. and led to advances later included in the other two papers that form the basis of this thesis. The second part, Chapter 2, is based on Paper II, and is about computing FIR Luminosity Functions in both standard and giant void cosmologies. The LFs for the standard model were computed independently and served to check all the LF results in (Gruppioni et al. 2013). The third part, Chapters 3 and 4, is drawn from Paper III. The third part establishes the link between the first two chapters, extending the formalism in the first part to the LTB dust models, and then applying it to the LFs computed in the second part. Two natural follow-ups of this work are foreseen. The first one extends the analysis characterising the fractal dimension of the high redshift relativistic number densities in Conde-Saavendra et al. (2013), to which I contributed the detailing about the use of the LF, to the power-law behavior fit here. The second follow-up entails extending the relativistic mass function analysis in Lopes et al. (2013), to which I contributed in the discussions about the content and format, to the LTB selection

functions obtained in this work.

In Paper II we focused on two questions by restricting the available models to those which are well constrained by a wealth of observations: given that the current observations still allow a certain degree of freedom for the cosmological model, are these constraining enough to yield a robust LF estimation, or are our statistical conclusions still dependent on the model? And how?

To address these questions, one needs at least two different cosmological models, in the sense of a set of equations that are a solution to the Einstein field equations, both parametrised to fit the whole set of available observations. Therefore, for the purpose stated above, the GBH parametrisation of the LTB dust model is sufficient.

We started from the FIR LF which has been recently established by Gruppioni et al. (2013), using combined data obtained on the PACS (Poglitsch et al. 2010), and SPIRE (Griffin et al. 2010) instruments aboard the Herschel (Pilbratt et al. 2010) space telescope, as part of two surveys, *the* PACS *Evolutionary Probe* (PEP; Lutz et al. 2011), and *the* Herschel *Multi-tiered Extragalactic Survey* (HerMES; Oliver et al. 2012). We used this sample because of its wide range of observations spanning from UV to the far-IR and because it is the most complete one in terms of wavelength coverage. In future works we intend to investigate the effect on LF when changing the underlying cosmology as a function of wavelength. The depth of the survey, or the relative depths at different wavelengths may also play a role.

In Gruppioni et al. (2013) we have used the PEP datasets to derive the evolutionary properties of the FIR sources in the standard cosmology. In Paper II, we aimed at using the same catalogues and methodology used by Gruppioni et al. (2013) to assess them in alternative cosmologies. We computed the rest-frame monochromatic 100 μm and 160 μm, together with the total IR LFs in the void models described in Zumalacárregui et al. (2012). We then compared the redshift evolution of the luminosity functions in both standard and void models.

Although Paper II used both the standard and alternative cosmological models, it did not aim at model selection, that is, making a comparison of the models *themselves*. It is common to assume that works which deal with alternative cosmologies always have the goal of testing the models directly.

This work is not about testing alternative cosmologies. Since the beginning of observational cosmology it has been clear that testing a cosmological model using galaxy surveys is extremely difficult because of the degeneracy between the intrinsic evolution of the sources and the relativistic effects caused by the underlying cosmology. Our understanding of galaxies is still far from allowing us to treat them as standard candles. The luminosity functions computed on Paper II depend, by definition, on the cosmological model assumed in its computation, and therefore cannot yield any independent conclusion about which model is the best fit.

Instead, by acknowledging that the computation of the luminosity functions depends on the cosmological model, in Paper II we aimed to assess how robust the luminosity function results are if the effective constraints on the cosmological model, like the Hubble diagram of a survey of standard candles like the SNe Ia, or the power spectrum of the cosmic microwave background (CMB), were imposed. In other words, the main interest of Paper II is on galaxy evolution models, and their possible dependency on the cosmological model but, not on the cosmological models themselves.

Whereas the motivation of Paper II was to probe the implications of the underlying cosmology on the redshift evolution of observable properties of the sources like number count and luminosity, on Paper III we aimed at further studying these implications, specifically, on the characterization of the number density of sources along the past lightcone of the assumed cosmology.

The past lightcone is a direct observable: it is the only region of the Universe's manifold that galaxy redshift surveys probe directly. In computing the densities in the lightcone, we remove the model assumption intrinsic to the usual comoving frame computations. The empirical approach of it, if not as ambitious, shares the same philosophy of the *ideal observational cosmology* programme of Ellis et al. (1985), which aimed at determining the spacetime geometry of the Universe without assuming a cosmological model *a priori*.

This line of work was started by Ribeiro & Stoeger (2003), which connected the relativistic cosmology number counts results summarized in Ellis (1971) to the practical LF results from galaxy redshift surveys. Ribeiro (2005) considered the effect of the expansion of the spacetime in the number densities along the past lightcone leading to the observational non-homogeneities in the spatially homogeneous FLRW model. Rangel Lemos & Ribeiro (2008) expanded on those theoretical results, showing that homogeneous distributions in the past lightcone would lead to spatial non-homogeneity, which contradicts the *Cosmological Principle*.

Albani et al. (2007) combined the results of the first two previous papers to compute such lightcone distributions using the luminosity functions for the CNOC2 survey Lin et al. (1999), confirming the presence of such light cone non-homogeneities. In Paper I we discussed further ways to compare the relativistic effect of the expanding spacetime to the evolution of the sources in the FLRW past lightcone, using the much bigger redshift range in the luminosity functions for the FORS Deep Field survey Gabasch et al. (2004, 2006).

The goal of Paper III was to include non-FLRW spacetimes in the past lightcone studies described above. We specialized the general equations of Ribeiro & Stoeger (2003) to the LTB metric, combining the results from both Ribeiro (1992), and Garcia-Bellido & Haugbølle (2008). Finally, we used the luminosity functions in

Iribarrem et al. (2013b), which were computed assuming the LTB/GBH model from their build-up.

The question we aimed to address in Paper III was the following: are the number densities along the past lightcone, and the characterisation of their power-law behaviour, robust among the standard and void cosmological models cited above? In addition, we discussed the comoving number density in the void models, with possible implications for empirical models like that in, e.g., Gruppioni et al. (2011); Béthermin et al. (2012).

The plan of the thesis is the following: in Chapter 1 we present the theoretical results for computing number densities in both FLRW and LTB models; in Chapter 2 we compute the PEP LFs; in Chapter 3 we compute the FIR comoving densities in both cosmologies, and show that source evolution is also needed on the more general LTB models to fit the observations; in Chapter 4 we compute the relativistic densities, and discuss their power-law behavior as a function of wavelength, cosmology, and density estimator; we summarize our findings in the Conclusions. Appendix A describe the mock catalogues created to test the validity of the LF estimator used in this work.

Chapter 1

Relativistic cosmology number densities in the past light-cone

In this chapter some basic results of relativistic cosmology theory required in this thesis are discussed. Starting from the general results, specialized equations are obtained for both standard and void cosmologies. We start with the general formalism in the context of the ΛCDM model.

1.1 Standard Cosmology: FLRW / ΛCDM model

As far as General Relativity is concerned, the standard model is consists of the FLRW metric having a perfect fluid energy-momentum tensor, and a non-vanishing cosmological constant Λ. An early inflationary phase, together with a hierarchical build-up of dark matter haloes are additions, with varying degrees of observational evidence, necessary to make the model fit all the available data. In this section we aim to obtain the relativistic number densities in the past light-cone defined in this cosmology.

1.1.1 Differential number counts

We begin by writing the FLRW line element as follows,

$$ds^2 = -c^2dt^2 + S^2\left[\frac{dr^2}{1-kr^2} + r^2\left(d\theta^2 + \sin^2\theta\, d\phi^2\right)\right], \tag{1.1}$$

where the time-dependent function $S = S(t)$ is the *cosmic scale factor*, k is the *curvature parameter* ($k = +1, 0, -1$) and c is the light speed. As it is well known, the Einstein's field equations with the metric corresponding to this line element yields the *Friedmann equation*, which, if the *cosmological constant* Λ is included,

may be written as below, *e.g.* Roos (1994),

$$H^2 = \frac{8\pi G\rho_m}{3} + \frac{\Lambda}{3} - \frac{kc^2}{S^2}, \tag{1.2}$$

where ρ_m is the *matter density* and we have assumed the usual definition for the *Hubble function* in terms of the scale factor, as follows,

$$H(t) \equiv \frac{1}{S(t)}\frac{dS(t)}{dt}. \tag{1.3}$$

Let us now define the *vacuum energy density* in terms of the cosmological constant as follows,

$$\rho_\Lambda \equiv \frac{\Lambda}{8\pi G}. \tag{1.4}$$

Remembering that the *critical density* is given by

$$\rho_{0,c} \equiv \frac{3{H_0}^2}{8\pi G}, \tag{1.5}$$

where H_0 is the *Hubble constant*, the following relative-to-critical *density parameters* relations hold,

$$\Omega_0 \equiv \Omega_{m_0} + \Omega_{\Lambda_0} = \frac{\rho_0}{\rho_{0,c}} = \frac{\rho_{m_0}}{\rho_{0,c}} + \frac{\rho_{\Lambda_0}}{\rho_{0,c}}. \tag{1.6}$$

We have used the zero index to indicate observable quantities at the present time. Notice that since Λ is a constant, then $\rho_\Lambda = \rho_{\Lambda_0}$. Considering the definitions (1.6), we can rewrite the Friedmann equation (1.2) at the present time as follows,

$$kc^2 = {H_0}^2{S_0}^2(\Omega_0 - 1). \tag{1.7}$$

In addition, from the law of conservation of energy applied to the zero pressure era we know that,

$$\rho_m \propto S^{-3} \Rightarrow \rho_{m_0} \propto {S_0}^{-3}, \tag{1.8}$$

which leads to,

$$\frac{\rho_m}{\rho_{m_0}} = \frac{{S_0}^3}{S^3} \Rightarrow \Omega_m = \Omega_{m_0}\frac{{S_0}^3}{S^3}. \tag{1.9}$$

The matter density parameter can also be written in terms of the critical density as,

$$\Omega_m = \frac{\rho_m}{\rho_c} = \frac{8\pi G}{3H^2}\,\rho_m. \tag{1.10}$$

We can rewrite equation (1.2) as a first order ordinary differential equation in terms of the scale factor $S(t)$, by using the results in equations (1.3) to (1.10), yielding,

$$\frac{dS}{dt} = H_0 \left[\frac{\Omega_{m_0} {S_0}^3}{S} + \Omega_{\Lambda_0} S^2 - (\Omega_0 - 1) {S_0}^2 \right]^{1/2}. \tag{1.11}$$

This equation can be analytically solved in terms of elliptic integrals or equivalently Jacobi elliptic functions, but since this is not the only differential equation needed in this work, the scale factor S is not obtained directly from it, but as part of a numerical solution for the two coupled equations needed for the analyses presented in this work, namely dS/dr and dN/dr. Next we shall obtain the second differential equation of this system, the one for the cumulative number count N.

Let us write the completely general, *cosmological model independent*, expression derived by Ellis (1971) for the number counts of cosmological sources which takes fully into account relativistic effects, as follows,

$$dN = (d_A)^2 d\Omega [n(-k^a u_a)]_P \, dy, \tag{1.12}$$

where dN is the *number of cosmological sources* in a volume section at a point P down the incoming null geodesic, n is the *number density* of radiating sources per unit of proper volume in a section of a bundle of light rays converging towards the observer and subtending a *solid angle* $d\Omega$ at the observer's position, d_A is the *area distance* of this section from the observer's viewpoint (also known as *angular diameter distance*, *observer area distance* and *corrected luminosity distance*), u^a is the observer's *4-velocity*, k^a is the *tangent vector* along the light rays and y is the *affine parameter distance* down the light cone constituting the bundle (see Ribeiro & Stoeger 2003, §2.1, figure 1). The *number density*, that is, the number of cosmological sources per proper volume unit can be related to matter density ρ_m by means of,

$$n = \frac{\rho_m}{\mathcal{M}_g}. \tag{1.13}$$

where, $\mathcal{M}_g$ is simply the *average galaxy rest mass*, dark matter included.

One should point out that the details of the galaxy mass function and how it evolves with the redshift are imprinted in the observed number density probed by the LF itself.This result implies that for the empirical purposes of the present work this equation is correct to the order of magnitude and must be regarded only as an estimation, meaning that equation (1.13) enables us to connect the theoretical relativistic quantities to the LF data and thus include the redshift evolution of the mass function empirically. However, to actually extract from the LF its implicit galaxy mass function requires some assumption about the function $\mathcal{M}_g(z)$.

For the empirical approach of this paper it is enough to assume a constant average galaxy rest mass with the working value of $\mathcal{M}_g \approx 10^{11}\mathcal{M}_\odot$ based on the estimate by Sparke & Gallagher (2000). Hence, if we use equations (1.9) and (1.10) we can rewrite equation (1.13) as,

$$n = \left(\frac{3\Omega_{m_0}{H_0}^2{S_0}^3}{8\pi G\mathcal{M}_g}\right)\frac{1}{S^3}. \tag{1.14}$$

The past radial null geodesic in the geometry given by metric (1.1) may be written as below,

$$\frac{dt}{dr} = -\left(\frac{S}{c\sqrt{1-kr^2}}\right). \tag{1.15}$$

Since both coordinates t and r are function of the affine parameter y along the past null cone, we have that

$$\frac{dt}{dy} = \frac{dt}{dr}\frac{dr}{dy} = -\left(\frac{S}{c\sqrt{1-kr^2}}\right)\frac{dr}{dy}. \tag{1.16}$$

Assuming now that both source and observer are comoving, then $u^a = c\,{\delta_0}^a$ and the following results hold,

$$-k^a u_a = -c\,k^a g_{0a} = -c\,k^0 = -c\frac{dt}{dy} = \left(\frac{S}{\sqrt{1-kr^2}}\right)\frac{dr}{dy}. \tag{1.17}$$

Noticing that the area distance d_A is defined by means of a relation between the *intrinsically measured* cross-sectional area element $d\sigma$ of the source and the observed solid angle $d\Omega_0$ (Ellis 1971, 2007; Plebański & Krasiński 2006), we have that

$$(d_A)^2 = \frac{d\sigma}{d\Omega} = \frac{S^2r^2(d\theta^2 + \sin^2\theta\,d\phi^2)}{(d\theta^2 + \sin^2\theta\,d\phi^2)} = (Sr)^2. \tag{1.18}$$

We note that for this metric the area distance, a strictly observational distance definition, equals the *proper distance* d_{Pr}, a relativistic one. Considering equation (1.7) and substituting equations (1.14), (1.17) and (1.18) into equation (1.12), in addition to remembering that for radial only dependence $d\Omega_0 = 4\pi$, we are then able to write the number of sources along the past light cone in terms of the radial coordinate r. This quantity is given by the following expression,

$$\frac{dN}{dr} = \left(\frac{3\,c\,\Omega_{m_0}{H_0}^2{S_0}^3}{2G\mathcal{M}_g}\right)\left[\frac{r^2}{\sqrt{c^2 - {H_0}^2{S_0}^2(\Omega_0 - 1)r^2}}\right]. \tag{1.19}$$

We want to solve the differential equations for the scale factor S and the cumulative number counts N, equations (1.11) and (1.19) respectively. A straightforward

approach is to take the radial coordinate r as the independent variable. Since equation (1.11) has its time coordinate implicitly defined in the scale factor, to solve it numerically we need to rewrite that differential equation in such a way that the independent variable becomes explicit. Considering equation (1.7), the null geodesic (1.15) becomes,

$$\frac{dt}{dr} = -\left[\frac{S^2}{c^2 - {H_0}^2 {S_0}^2 (\Omega_0 - 1) r^2}\right]^{\frac{1}{2}}. \tag{1.20}$$

Along the past light cone, we can write the scale factor in terms of the radial coordinate as,

$$\frac{dS}{dr} = \frac{dS}{dt}\frac{dt}{dr}, \tag{1.21}$$

and, thus, we are able to rewrite equation (1.11) in terms of the radial coordinate, as shown below,

$$\frac{dS}{dr} = -H_0 \left[\frac{(\Omega_{\Lambda_0}) S^4 - {S_0}^2 (\Omega_0 - 1) S^2 + (\Omega_{m_0} {S_0}^3) S}{c^2 - {H_0}^2 {S_0}^2 (\Omega_0 - 1) r^2}\right]^{\frac{1}{2}}. \tag{1.22}$$

To find solutions for $S(r)$ we must assume numerical values for Ω_{m_0}, Ω_{Λ_0} and H_0.

The two differential equations (1.19) and (1.22) comprise our numerical problem since they are written in terms of the radial coordinate and can be numerically solved simultaneously, thus enabling us to generate tables for r, S and N. A computer code using the fourth-order Runge-Kutta method is good enough to successfully carry out the numerical tasks. The initial conditions r_0 and N_0 are set to zero, whereas S_0 can be derived considering that as $r \to 0$ the spacetime is approximately Euclidean, that is, $k \approx 0$. This leads, from equation (1.15), to $ct = -r$ and, finally, $S_0 = 1$.

The *redshift* z can be written as

$$1 + z = \frac{S_0}{S}, \tag{1.23}$$

where it is clear that a numerical solution of the scale factor $S(r)$ immediately gives us the numerical solution for $z(r)$. We can derive the *differential number counts* dN/dz by means of the following expression,

$$\frac{dN}{dz} = \frac{dr}{dz}\frac{dN}{dr}, \tag{1.24}$$

with the help of the useful relation,

$$\frac{dr}{dz} = \frac{dr}{dS}\frac{dS}{dz}. \tag{1.25}$$

Numerically, since we build all our quantities using $N(r)$ and $S(r)$, any redshift derivative we wish to evaluate will be similarly written in terms of the radial coor-

dinate derivative of that quantity. The derivatives in equation (1.25) can be taken from definition (1.23) and equation (1.22), enabling us to write,

$$\frac{dr}{dz} = \frac{S^2}{S_0\, H_0}\left[\frac{(\Omega_{\Lambda_0})S^4 - {S_0}^2(\Omega_0 - 1)S^2 + (\Omega_{m_0}{S_0}^3)S}{c^2 - {H_0}^2{S_0}^2(\Omega_0 - 1)r^2}\right]^{-\frac{1}{2}}, \tag{1.26}$$

which, together with equation (1.19), allows us to write equation (1.24) as follows,

$$\frac{dN}{dz} = \left(\frac{3\ c\ \Omega_{m_0}H_0{S_0}^2}{2G\mathcal{M}_g}\right)\left[\frac{r^2a^2}{\sqrt{(\Omega_{\Lambda_0})S^4 - {S_0}^2(\Omega_0 - 1)S^2 + (\Omega_{m_0}{S_0}^3)S}}\right]. \tag{1.27}$$

1.1.2 Number densities

So far we have used only the area distance d_A as distance definition. However, other cosmological distances can, and will, be used later. They can be easily obtained from the area distance by invoking the *Etherington's reciprocity law* (Etherington 1933; Ellis 1971, 2007), which reads as follows,

$$d_L = (1+z)^2 d_A = (1+z)\ d_G. \tag{1.28}$$

Here d_L is the *luminosity distance* and d_G is the *galaxy area distance* (also known as *angular size distance*, *transverse comoving distance* or *proper motion distance*). A fourth distance will also be useful later, the *redshift distance* d_z, defined by the following equation,

$$d_z = \frac{c\ z}{H_0}. \tag{1.29}$$

Although the reciprocity law is independent of any cosmological model, the detailed calculations presented in the previous sections are for FLRW cosmology only, which means that in deriving d_A, d_L, d_G and d_z we write the FLRW expression for d_A and derive the others using the general, model independent, expression (1.28), as well as equation (1.29). Thus, considering equation (1.18) for d_A, together with equation (1.23) and the reciprocity theorem (1.28), it is straightforward to write the other cosmological distances in terms of the scale factor, as follows,

$$d_L = {S_0}^2\left(\frac{r}{S}\right), \tag{1.30}$$

$$d_G = S_0\, r, \tag{1.31}$$

$$d_z = \frac{c}{H_0}\left(\frac{S_0}{S} - 1\right). \tag{1.32}$$

Let us now generically call by d_i a certain observational distance, which can be any one of the four cosmological distances defined above ($i = A, G, L, Z$). The *differential*

density γ_i, gives the number of sources per unit volume located at a certain distance d_i, being defined as follows (Ribeiro 2005),

$$\gamma_i = \frac{1}{4\pi(d_i)^2}\frac{dN}{d(d_i)}, \tag{1.33}$$

while the *integrated differential density*, or simply *integral density*, gives the number of sources per unit volume located anywhere inside the observer's past light cone down to a distance d_i, being written as,

$$\gamma_i^* = \frac{1}{V_i}\int_{V_i} \gamma_i \, dV_i. \tag{1.34}$$

Here V_i is the *observational volume*, defined as,

$$V_i = \frac{4}{3}\pi(d_i)^3. \tag{1.35}$$

These quantities are useful in the determination of whether or not, and at what ranges, a spatially homogeneous cosmological model can or cannot be observationally homogeneous as well (Rangel Lemos & Ribeiro 2008). This is so because these densities behave very differently depending on the distance measurement used in their expressions, that is, they show a clear dependence on the adopted cosmological distance definition. Therefore, as discussed in Rangel Lemos & Ribeiro (2008), these measures are the ones required for the focus of this thesis, that is, they are capable of probing the possible observational inhomogeneity of the number counts, since they were devised to specifically deal with this problem.

From a numerical viewpoint it is preferable to write these two densities above in terms of the redshift. Thus, the differential density may be written as,

$$\gamma_i = \frac{dN}{dz}\left\{4\pi(d_i)^2\,\frac{d(d_i)}{dz}\right\}^{-1}. \tag{1.36}$$

Up to this point, our approach has been completely general. We now specialise the equations to the FLRW model. What remains to be determined are the derivatives of each distance against the redshift. Starting with the area distance d_A, they can be easily obtained from equations (1.18) and (1.23). Then it follows that,

$$\frac{d(d_A)}{dz} = \frac{dS}{dz}\frac{dr}{dS}\frac{d(d_A)}{dr} = -\frac{S^2}{S_0}\left[r + S\left(\frac{dS}{dr}\right)^{-1}\right], \tag{1.37}$$

and, considering equation (1.22), this expression may be rewritten as below,

$$\frac{d(d_A)}{dz} = \frac{S^2}{S_0}\left[\frac{S}{H_0}\sqrt{\frac{c^2 - {H_0}^2{S_0}^2(\Omega_0 - 1)r^2}{(\Omega_{\Lambda_0})S^4 - {S_0}^2(\Omega_0 - 1)S^2 + (\Omega_{m_0}{S_0}^3)S}} - r\right]. \tag{1.38}$$

The other observational distances can be numerically calculated from equation (1.37) if we consider the reciprocity law (1.28). Therefore, we have that,

$$\frac{d(d_L)}{dz} = 2(1+z)d_A + (1+z)^2\frac{d(d_A)}{dz}, \tag{1.39}$$

$$\frac{d(d_G)}{dz} = d_A + (1+z)\frac{d(d_A)}{dz}. \tag{1.40}$$

These two equations can also be rewritten in terms of the scale factor if we consider equations (1.23) and (1.38), yielding,

$$\frac{d(d_L)}{dz} = S_0\left[\frac{S}{H_0}\sqrt{\frac{c^2 - {H_0}^2{S_0}^2(\Omega_0 - 1)r^2}{(\Omega_{\Lambda_0})S^4 - {S_0}^2(\Omega_0 - 1)S^2 + (\Omega_{m_0}{S_0}^3)S}} + r\right], \tag{1.41}$$

$$\frac{d(d_G)}{dz} = \frac{a^2}{H_0}\sqrt{\frac{c^2 - {H_0}^2{S_0}^2(\Omega_0 - 1)r^2}{(\Omega_{\Lambda_0})S^4 - {S_0}^2(\Omega_0 - 1)S^2 + (\Omega_{m_0}{S_0}^3)S}}. \tag{1.42}$$

A final point still needs to be discussed. The integral density (1.34) is a result of integrating γ_i over a radial volume. The simplest way of numerically deriving it is shown in what follows. Let us differentiate γ_i^* in terms of the volume, so that,

$$\frac{d\left(\gamma_i^* V_i\right)}{dV_i} = \gamma_i. \tag{1.43}$$

Considering equation (1.33), this result leads to the following expression,

$$\frac{d\left(\gamma_i^* V_i\right)}{dz} = \frac{d\left(\gamma_i^* V_i\right)}{dV_i}\frac{dV_i}{dz} = \gamma_i\frac{dV_i}{dz} = \frac{dN}{dz}. \tag{1.44}$$

Similarly, it is simple to conclude that,

$$\frac{d\left(\gamma_i^* V_i\right)}{dr} = \frac{dN}{dr}. \tag{1.45}$$

Finally, from the definitions of γ_i and γ_i^*, it is easy to show that the following expression holds,

$$\gamma_i^* = \frac{N}{V_i}. \tag{1.46}$$

The numerical solution of equation (1.19) together with the numerical determination of all distances, as given by equations (1.18), (1.30), (1.31), (1.32), allow us to

calculate the volume (1.35) and evaluate γ_i^*. These results fully determine the numerical problem for the cosmological model under study.

1.1.3 Volumes

Most cosmological densities obtained from astronomical observations assume the *comoving volume*, whereas densities derived from theory often assume the *local*, or *proper*, *volume*. The luminosity function, for instance, is nowadays always obtained from galaxy catalogues by assuming the comoving volume in its calculation. So, we are only able to compare those observationally derived parameters with theory if we carry out a conversion of volume units. From metric (1.1) it is obvious that,

$$dV_{_{Pr}} = \frac{S^3}{\sqrt{1-kr^2}}\, r^2\, dr\, \sin\theta\, d\theta\, d\phi = S^3 dV_{_C}, \tag{1.47}$$

This equation clearly defines the conversion factor between these two volume definitions in terms of the numerical scheme developed above.

1.2 Giant void Cosmology: LTB / CGBH model

Garcia-Bellido & Haugbølle (2008, hereafter GBH) have shown that an LTB dust model could be parametrised to fit successfully and simultaneously many independent observations without the inclusion of a cosmological constant. The extra dimming of distant SNe Ia, compared to their expected observed fluxes in a flat, spatially homogeneous Einstein-de Sitter (EdS) universe is then understood not as being caused by an acceleration of the expansion rate, but rather as an extra blueshift of the incoming light caused by a non-homogeneous matter distribution in the line of sight.

This so-called void model is characterised by an effective under-dense region of Gpc scale around the Milky Way, as opposed to the average spatial homogeneity supposed to hold at that scale by the standard model. In this under-dense region, both the matter density profile $\Omega_{_M}$ and the transverse Hubble constant H_0 are functions of the radial coordinate r.

At high enough redshifts however, the model is made to converge to an EdS-like solution, making the non-homogeneity a localized property of the model and naturally reconciling it with the observed degree of isotropy in the cosmic microwave background radiation. The use of a pressure-less (dust) energy-momentum tensor, as opposed to the perfect fluid one allowed in the standard model, is required in order to obtain an exact solution for Einstein's field equations assuming the LTB line element. At early epochs (high redshifts), the radiation dominated the Universe's

energy budget, and the pressure term was relevant, but as discussed before, at these scales, the LTB model is made to converge to the EdS solution by the GBH parameterization. At later epochs (low redshifts), radiation pressure is negligible, and so the use of a dust energy-momentum tensor is well justified. Geometrically, the LTB dust model is an analytical solution for Einstein's field equations, and arguably the simplest way to release the spatial homogeneity assumption present in the standard model of cosmology.

Spatial homogeneity is, nevertheless, a symmetry assumption that greatly simplifies the model. Removing it will unavoidably increase the degrees of freedom of the model. Because of this, even the most constrained parametrisations of the LTB models still show an increased number of free parameters compared to the standard model. Since the quality of the combined fits to the observations these alternative models can produce is similar to that produced by the standard model, any analysis that penalizes a greater degree of freedom of a model, like those used in Zumalacárregui et al. (2012) and de Putter et al. (2012), will disfavour such parameterization of the LTB model in comparison to ΛCDM.

In the empirical approach of Albani et al. (2007), the number densities along the observer's past lightcone were computed from the LF data using different relativistic cosmology distance definition. These distances are defined in the same cosmological model as the one assumed to build the LF. In this sense no assumption on the redshift evolution of the sources is made. The methodology is completely empirical.

The number densities used in this work, as defined in Ribeiro (2005), are able to probe the geometrical effect of the expansion of Universe on the homogeneity of the distribution of the sources along the observer's past lightcone. This effect depends on the distance definition used in computing these densities, which in turn depends on the line element of the cosmological model assumed.

In this section we connect the key results from Ribeiro (1992, henceforth R92) for the number count of sources in the LTB metric to the parametrisation advanced by Garcia-Bellido & Haugbølle (2008) for that cosmology. The goal here is to compute the above mentioned number densities in the giant void parametrisation of the LTB model. Dotted quantities refer to time-coordinate derivatives and primed ones refer to radial-coordinate derivatives.

1.2.1 Differential number counts

We started by writing the line element for the LTB model following Bonnor (1972)

$$ds^2 = -c^2dt^2 + \frac{A'^2(r,t)}{f^2(r)}dr^2 + A^2(r,t)d\Omega^2, \tag{1.48}$$

where $d\Omega^2 = d\theta^2 + \sin^2\theta\, d\phi^2$, with $f(r)$ an arbitrary function, and $A(r,t)$ being analogous to the scale factor in the FLRW metric. Assuming a pressure-less (dust) matter content with $\rho_{_M}$ proper density, it can be shown that the Einstein's field equations for that line element can be combined to yield (R92)

$$8\pi G\rho_{_M} = \frac{F'}{2A'A^2}, \tag{1.49}$$

where $F(r)$ is another arbitrary function, and G is the gravitational constant. Starting from the general expression for the number count of sources derived by Ellis (1971), R92 obtained

$$dN = 4\pi\, n\, \frac{A'A^2}{f}\, dr, \tag{1.50}$$

where n is the number density per unit proper volume, and N the total number of sources on the past lightcone. Following R92 we wrote,

$$n = \frac{F'}{16\pi G\, \mathcal{M}_g\, A'A^2}. \tag{1.51}$$

Combining the last two equations we obtained,

$$\frac{dN}{dr} = \frac{1}{4G\, \mathcal{M}_g}\, \frac{F'}{f}. \tag{1.52}$$

The last equation is essentially a version of the result of Ellis (1971), specialized to the LTB past null geodesic. Next, we further specialized it to use the GBH parametrisation for their constrained model, and the best fit values obtained by Zumalacárregui et al. (2012) in a simultaneous analysis of SNe Ia, CMB and BAO data.

It is straightforward to relate $f(r)$ to the spatial curvature parameter $k(r)$ in GBH by writing

$$f(r) = \sqrt{1 - k(r)}. \tag{1.53}$$

The boundary condition equations listed in GBH read,

$$H_{_T}(r,t) = \frac{\dot{A}(r,t)}{A(r,t)}, \tag{1.54}$$

$$F(r) = 2\,\Omega_{_M}(r)\, H_0^2(r)\, r^3, \tag{1.55}$$

$$k(r) = -[1 - \Omega_{_M}(r)]\, H_0^2(r)\, r^2, \tag{1.56}$$

with the gauge choice $A(r,0) = r$ included, $H_{_T}$ being the transverse Hubble rate (see below), with $H_0(r) = H_{_T}(r,0)$, and $\Omega_{_M}(r)$ the dimensionless matter density

parameter, defined relative to the integrated critical density in the comoving volume,

$$\bar{\rho}_C(r) = \frac{3\,H_0^2(r)}{8\pi\,G}, \tag{1.57}$$

as $\Omega_M(r) = \rho_M(r)/\bar{\rho}_C(r)$. Note that the curvature parameter $k(r)$ is not constant in the GBH parametrisation, but depending on the radial coordinate r and the shape of the matter density parameter $\Omega_M(r)$, it can assume positive, negative or zero values.

Because of its dependence on the cosmic time, the LTB geometry possesses radial expansion rate and scale factor that are in general different from their transverse counterparts. The present-time transverse Hubble parameter, $H_0(r)$, in the constrained version of the GBH model is parametrised as,

$$H_0(r) = H_{in} \sum_{j=0}^{\infty} \frac{2\,[1-\Omega_M(r)]^j}{(2j+1)(2j+3)}, \tag{1.58}$$

where H_{in} is the transverse Hubble constant at the center of the void. Equations (1.53), (1.56), and (1.58) can be readily combined to yield

$$f(r) = \sqrt{1 + [1-\Omega_M(r)] \left\{ \sum_{j=0}^{\infty} \frac{2\,[1-\Omega_M(r)]^j}{(2j+1)(2j+3)} \right\}^2 {H_{in}}^2 r^2}. \tag{1.59}$$

Combining Eqs. (1.55), and (1.58) we can write the $F(r)$ function for the constrained model as

$$F(r) = H_{in} \left\{ \sum_{j=0}^{\infty} \frac{2\,[1-\Omega_M(r)]^j}{(2j+1)(2j+3)} \right\} \Omega_M(r)\, r^3, \tag{1.60}$$

where the dimensionless matter density parameter $\Omega_M(r)$ in the GBH model becomes

$$\Omega_M(r) = \Omega_{out} + (\Omega_{in} - \Omega_{out}) \left\{ \frac{1 - \tanh[(r-R)/2\Delta R]}{1 + \tanh[R/2\Delta R]} \right\}. \tag{1.61}$$

Here Ω_{in} is the density parameter at the center of the void, Ω_{out} the asymptotic density parameter at large comoving distances, R is the size of the underdense region, and ΔR the width of the transition between the central void and the exterior homogeneous region. These parameters completely determine the model. In the standard model both the matter density parameter and the Hubble parameter do not depend on the radial coordinate. In all the standard model computations done in this work we use $\Omega_M = 0.27$, $\Omega_\Lambda = 0.73$, and $H_0 = 71$ km s^{-1} Mpc^{-1} as obtained in Komatsu et al. (2011). Figure 1.1 shows the comparison of the evolution of the matter density parameter in the standard and in the void cosmologies.

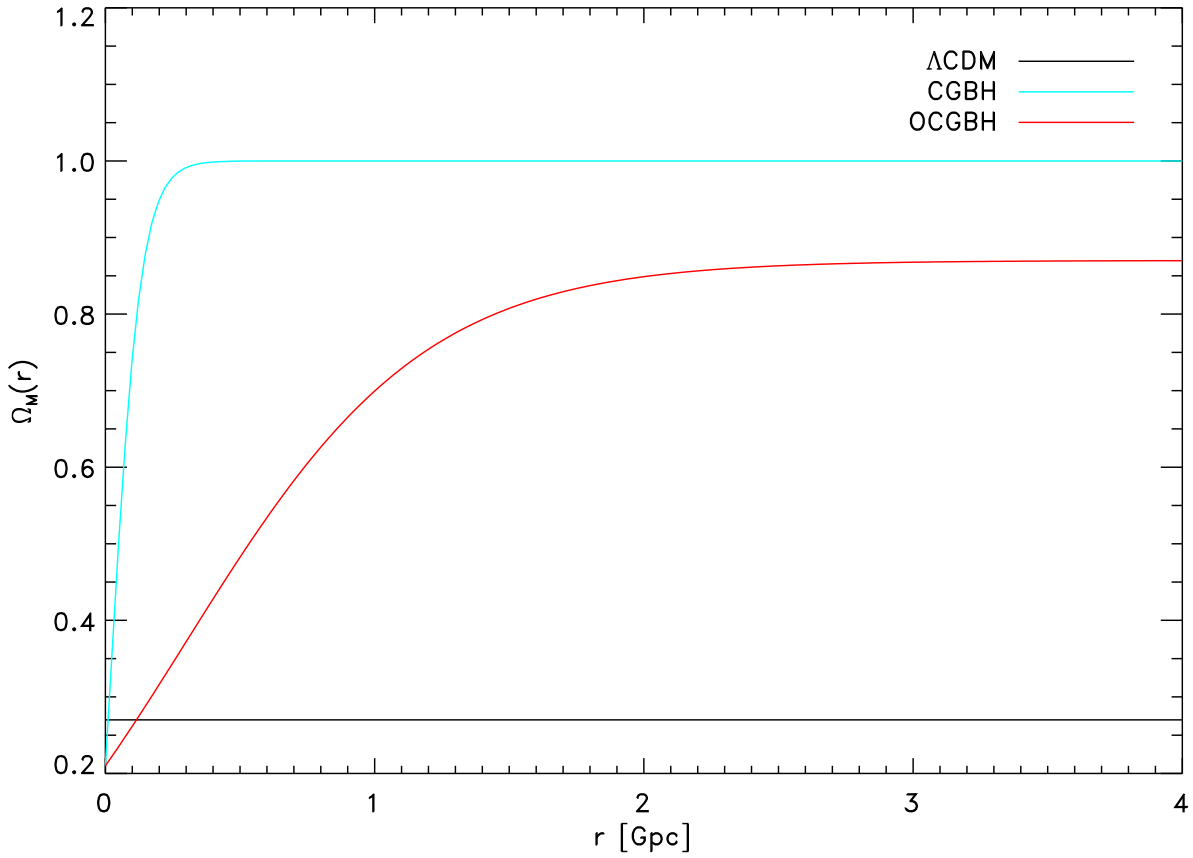

Figure 1.1: Present-time ($t=t_0$) matter density parameters in the standard (ΛCDM, black line) and the void (GBH) cosmological models (red and cyan lines).

Table 1.1: Best fit values for the LTB/CGBH models (Zumalacárregui et al. 2012).

Model parameter	CGBH	OCGBH
H_{in}	66.0 ± 1.4	71.1 ± 2.8
Ω_{in}	0.22 ± 0.4	0.22 ± 0.4
R [Gpc]	$0.18\ ^{+0.64}_{-0.18}$	$0.20\ ^{+0.87}_{-0.19}$
ΔR [Gpc]	$2.56\ ^{+0.28}_{-0.24}$	$1.33\ ^{+0.36}_{-0.32}$
Ω_{out}	1	0.86 ± 0.03

Because of the generality of the evolution of $A(r,t)$ in the LTB models, the time coordinate t_{bb}, at which $A(r,t_{bb})$ reduces to zero, can, in general, assume different values for different comoving distances from the center of the under-dense region, r. This leads to different measurements for the elapsed time since the Big Bang, $t_{bb}(r)$, depending on the position of the observer in the void. Setting this extra degree of freedom for the big-bang time in order to make it simultaneous (same value for all observers) yields the constrained version of the GBH model, or CGBH model.

The best fit values we use in this work were obtained in Zumalacárregui et al. (2012), considering both an asymptotically flat CGBH model with $\Omega_{out} = 1$ and an open CGBH model (OCGBH) with $\Omega_{out} = 0.87$ which the authors show to better fit the CMB constraints. Table 1.1 reproduces these values.

With these values, $f(r)$, $F(r)$, and $\Omega_M(r)$ can be computed through Eqs. (1.59) - (1.61) for each comoving distance r. The radial derivative $F'(r)$ can be obtained numerically through central difference quotients, $F(r) \approx \lim_{\Delta r \ll r} \Delta F/\Delta r$, which in turn allow the values of dN/dr to be computed through Eq. (1.52).

The generalized scale factor $A(r,t)$ can be computed in parametric form as

$$A(r,t) = \frac{\Omega_M(r)}{2[1-\Omega_M(r)]^{3/2}}[\cosh(\eta) - 1]\, A_0(r), \tag{1.62}$$

where $A_0(r)$ is its value at $t = t_0$, and the parameter η advances the iteration of the numerical solution given r, t, $H_0(r)$, and $\Omega_M(r)$ as follows:

$$\sinh(\eta) - \eta = 2\,\frac{[1-\Omega_M(r)]^{3/2}}{\Omega_M(r)}\, H_0(r)\, t. \tag{1.63}$$

To obtain the $r(z)$ and $t(z)$ relations in this cosmology, we start with the radial null-geodesic equation, which can be written by making $ds^2 = d\Omega^2 = 0$, yielding

$$\frac{dt}{dr} = -\frac{A'(r,t)}{\sqrt{1-k(r)}}, \tag{1.64}$$

where the minus sign is set for incoming light. The redshift can be related to the radial coordinate in this model following Bondi (1947); Ribeiro (1992); Plebański &

Krasiński (2006); Enqvist & Mattsson (2007),

$$\frac{dr}{dz} = \frac{1}{1+z}\frac{f}{\dot{A}'}, \tag{1.65}$$

which combined with Eq. (1.64) yields,

$$\frac{dt}{dz} = -\frac{1}{1+z}\frac{A'}{\dot{A}'}. \tag{1.66}$$

All the first and second order derivatives of $A(r,t)$ can computed from Eq. (1.62) by means of central difference quotients, allowing Eqs. (1.65) and (1.66) to be solved numerically. This yields the look-back time and radial distance tables: $t(z)$ and $r(z)$.

We then combined Eqs. (1.52) and (1.65) as,

$$\frac{dN}{dz} = \frac{1}{4G\,\mathcal{M}_g}\frac{F'[r(z)]}{(1+z)\,\dot{A}'[r(z),t(z)]}, \tag{1.67}$$

and computed the differential number count dN/dz for each value of z in the $r(z)$, and $t(z)$ tables. A comparison between the estimates for this quantity in the ΛCDM and both CGBH parametrisations in Zumalacárregui et al. (2012) can be found in figure 1.2.

1.2.2 Volumes

Starting from the definition given in Eq. (1.18), it is straightforward to show that for the LTB metric in Eq. (1.48) the angular diameter distance is given by $d_A(z) = A[r(z),t(z)]$. With this result, we can use Eq. (1.28) to compute the luminosity distance $d_L(z)$, and galaxy area distance $d_G(z)$. It is worth noting that the comoving distance r is not, *in general*, equal to the galaxy area distance d_G, as it is in FLRW models, see Eq. (1.31). As a consequence, an LTB model with its luminosity distance-redshift relation constrained to fit the Hubble diagram for SNe Ia could still yield comoving distances, and therefore volumes, significantly different from those obtained in the standard model.

The additional constraint imposed by the measurements of the BAO(e.g. Percival et al. 2010; Reid et al. 2012) appears to pin down the comoving distance quite effectively up to intermediate redshifts, and it turns out that the difference in these distances computed in the ΛCDM and the GBH models is never larger than 10% at $z = 1$. However, r computed in the CGBH model at $z = 5$ is approximately 12% smaller, and $\approx 17\%$ in the open CGBH model.

The non-linear nature of the equations relating distances to volumes and luminosities, in particular for high-redshift sources, must also be considered. At redshift $z = 0.4$, for example, the luminosity distances computed in the void models CGBH

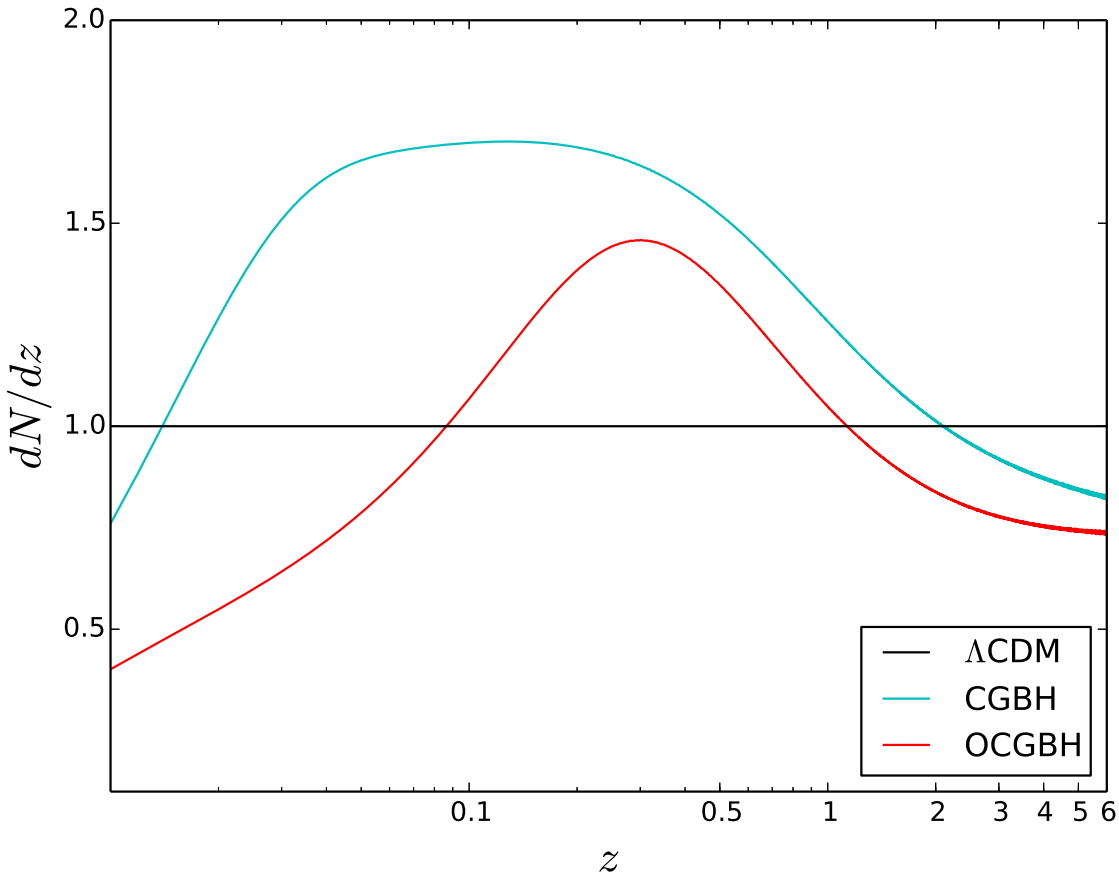

Figure 1.2: Differential number count estimates within the past lightcone of the three cosmological models used in the present work, with respect to the values for the ΛCDM model.

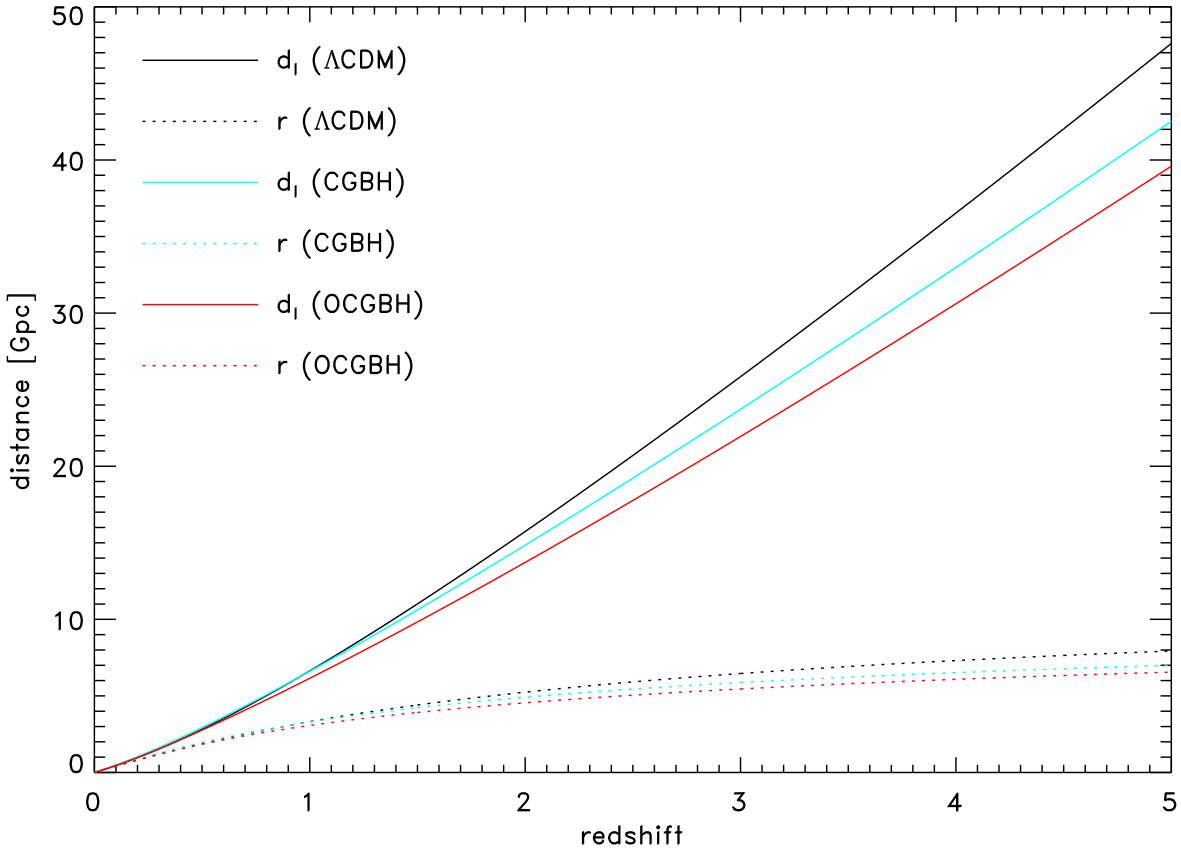

Figure 1.3: Luminosity (solid lines) and comoving distances (dotted lines) versus the redshift in the standard (ΛCDM) and the void (GBH) cosmological models. Up to redshift $z \approx 1$ distances in the constrained, flat void model (CGBH) follow very closely their standard model counterparts, but even in the case of the best-fit parameters in Zumalacárregui et al. (2012) yield increasingly different distances with the redshift.

and OCGBH respectively, are 4.90% and 0.92% shorter then the standard model distances, whereas the comoving distances in the void models are 4.88% and 0.96% shorter when compared to the standard model value. Such differences correspond to an extra dimming in luminosities equal to 10.04% in the CGBH model and 1.85% in the OCGBH model. The corresponding reduction in volumes is 15.35% and 2.84% for the CGBH and OCGBH models.

When compared to the standard model, these non-linearities can make small discrepancies in luminosity and comoving distances caused by the central underdensity in GBH models and can result in non-negligible differences in the shape of the LF.

This can be understood by looking at Fig. 1.3, where the luminosity distance and the comoving distance are plotted against the redshift. For any given redshift z', consider the differences $\Delta d_L(z')$ and $\Delta r(z')$ between the distances computed in the standard model and those in the void models. Both differences depend on

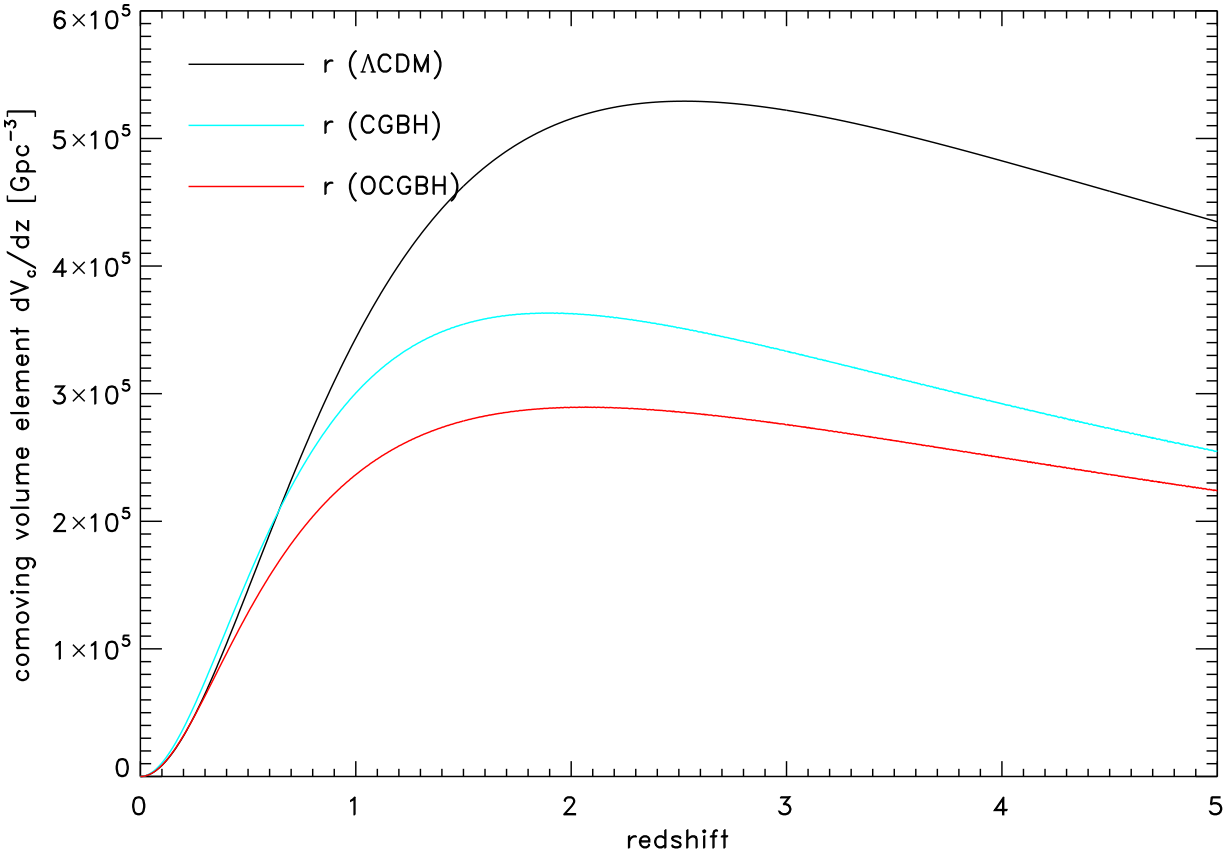

Figure 1.4: Comoving volume elements in the standard (ΛCDM) and the void (GBH) cosmological models. The quantities in the void models adopted here evolve with the redshift in a similar way to the standard model up to redshift approximately 0.6, then their values become consistently lower than in the ΛCDM model.

the redshift and do not, in general, cancel out or even yield a constant volume-to-luminosity ratio as a function of the redshift. As a result, the number of sources in each luminosity bin might change because of differences in the luminosities.

Additionally, the weight $1/V_{max}$ that each source adds to the LF in that bin will not be the same, leading to a LF value in that luminosity bin in the void model that is different from the one in the standard model, even if the sources inside the bin are the same. Figure 1.4 shows the comoving volume element in the different cosmologies adopted here.

Such differences in the estimated value for the LF in each luminosity bin will not, in general, be the same. As a consequence, not only the normalization but also the shape of the LF might change from one cosmology to another.

1.2.3 Number densities

With the differential number counts dN/dz computed in §1.2.1, we can compute the relativistic *differential number densities* γ_i, the number of sources per unit volume in a spherical shell at redshift z, for each distance d_i in $i = [A, G, L, z]$ discussed in §1.2.2, in the LTB/CBG models using the general result in Eq. 1.36.

The *integral number densities* γ_i^*, i.e. the number of sources per unit volume located inside the observer's past lightcone down to redshift z, can be computed for each distance definition d_i using Eq. 1.46.

Results for the various γ_i and γ_i^* in the different cosmologies considered in this work are plotted in figures 1.5 and 1.6. We note that even among the feasible cosmological models the differential and integral number densities show noticeable, even if apparently small to the eye, differences in all distance definitions used. These differences may actually be observed, depending on the precision achieved by a galaxy survey. It follows to check whether this purely geometrical effect can be detected on the LF for the PEP survey computed next.

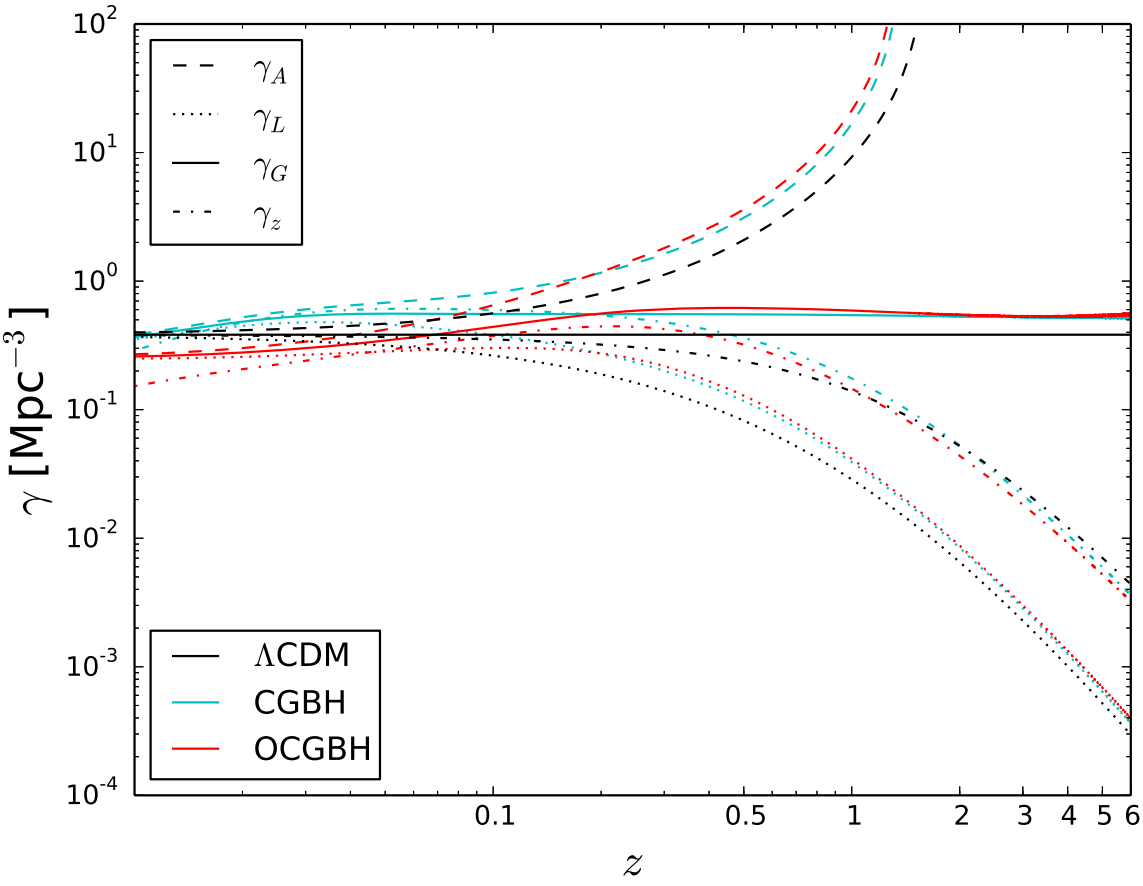

Figure 1.5: Redshift evolution of the relativistic differential densities for the three cosmological models used in the present work. Different curves correspond to the computations performed with respect to different distance estimators along the observer's past cone (d_A, d_L, d_G, and dz).

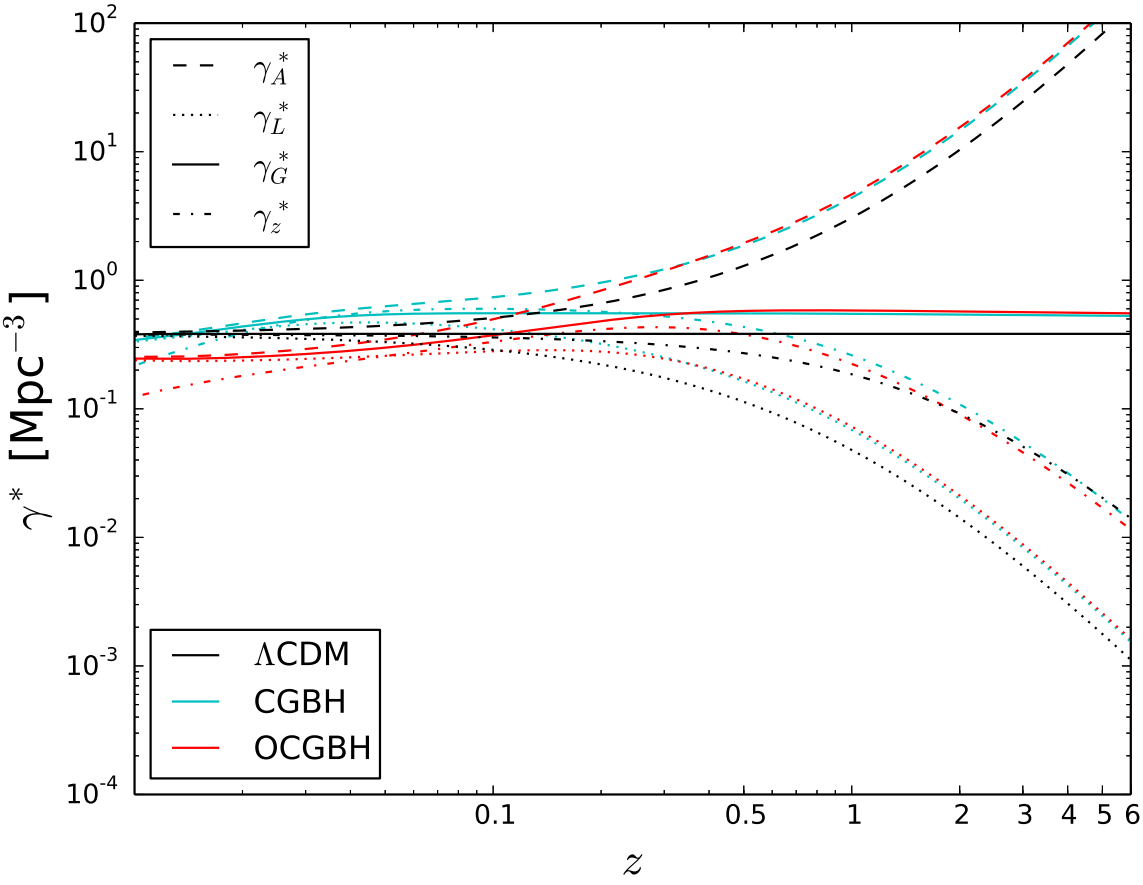

Figure 1.6: Integral of the functions shown in Fig. 1.5. The curves show the evolution of the relativistic integral densities for the three cosmological models used in the present work as a function of the different distances.

Chapter 2

Luminosity functions

In this chapter we present and discuss the main results and equations in deriving the LFs, which are susceptible to a change in the underlying cosmology.

2.1 The *Herschel*/PACS Evolutionary Probe (PEP) multi-wavelength samples

We use from the multi-wavelength catalogues described in (Berta et al. 2011). The sources in these catalogues were blindly selected in the following fields (effective areas): GOODS-N (300 arcmin^2), GOODS-S (300 arcmin^2), COSMOS (2.04 deg^2), and ECDF-S (700 arcmin^2), as part of the PEP survey in the 100 and 160 μm filters of Herschel/PACS. The number of sources detected and the 3-σ flux limits of this dataset are, in the 100 and 160 μm passbands, respectively: 291 sources down to 3.0 mJy, and 316 sources down to 5.7 mJy for GOODS-N; 717 down to 1.2 mJy, and 867 sources down to 2.4 mJy for GOODS-S; 5355 sources down to 5.0 mJy, and 5105 sources down to 10.2 mJy for COSMOS; and finally, 813 sources down to 4.5 mJy, and 688 sources down to 8.5 mJy for ECDF-S. For each of these fields, in each band individually, incompleteness corrections for the number counts were computed by the authors using simulations.

The semi-empirical spectral energy distribution (SED) models of Gruppioni et al. (2010) that expand on the models of Polletta et al. (2007) were used to fit the photometry of the objects using the LePhare code (Arnouts et al. 1999; Ilbert et al. 2006). The code has an output for each successfully fit source of a file with synthetic AB magnitudes m_ν in the wavelength range of the combined optical/NIR + FIR models. From this, we compute the spectral density of flux $f(\nu)$ as

$$f(\nu) = 10^{(23.9-m_\nu)/2.5}. \tag{2.1}$$

Sources without a redshift determination were removed from the catalogues, but no further redshift-based selection rule have been applied. In the GOODS-N redshift completeness is 100% within the ACS area (Berta et al. 2010), of which 70% of the redshifts being spectroscopic. These figures are 100 (80)% for the GOODS-S, within the MUSIC (Grazian et al. 2006; Santini et al. 2012) area; 93 (40)% for the COSMOS; and 88 (25)% for the ECDF-S fields. Non-detections in the 100 and 160 μm filters were also removed. Our final combined samples have 5039 sources in the 100 μm band (183 in the GOODS-N, 468 in the GOODS-S, 3817 in the COSMOS, and 578 in the ECDF-S fields); and 5074 sources in the 160 μm band (197 in the GOODS-N, 492 in the GOODS-S, 3849 in the COSMOS, and 547 in the ECDF-S fields). Approximately 40% of these sources were best fit by typical spiral SED templates, 7% of those were best fit by starburst templates, another 7% were found to be luminous IR galaxies, and 46% were best fit by obscured, or low-luminosity AGN templates. For a more complete description of the dataset used in this work, see Gruppioni et al. (2013).

We computed the rest-frame total IR luminosity of each source using its best fit SED $f(\nu)$ by means of

$$L_{IR} = 4\pi\,(1+z)\,d_L(z)^2 \int_{8\mu m}^{1000\mu m} f(\nu)d\nu\,, \tag{2.2}$$

Whereas, the rest-frame luminosity related to the observed flux f_R at a given band R can be obtained with

$$L_R = 4\pi\,\nu_R\,k_R\,f_R\,d_L(z)^2, \tag{2.3}$$

where d_L is the luminosity distance in a particular cosmological model, ν_R is the effective frequency of the filter at the observer's frame (corresponding to wavelengths approximately 100 and 160 μm for the PACS bands considered in the present work), and k_R is the k correction between the observed frame flux f_R in the R band and its rest-frame flux, at redshift z.

Because this paper deals with more than one underlying metric, it is important to note that, even though the relation between the cosmological redshift and the cosmological distances depend on the metric, thus affecting, for example, maximum redshift estimates, the redshift itself, and its effect on the SED of the sources, is directly measurable. Therefore, even though the rest-frame luminosities themselves depend on the cosmological model, the k-correction values depend only on the redshift measurements. It is when translating the measured redshift to an actual distance that a metric for the underlying spacetime is needed.

2.2 k corrections

In the following discussion, all quantities are written in frequency units. Primes are used to mark quantities evaluated at the *source's rest frame*. We follow closely the derivation in Hogg et al. (2002), but write the resulting k correction in terms of fluxes instead of magnitudes.

The effect of the expansion of the metric over the frequencies of the light arriving from each source is

$$\nu' = (1+z)\nu, \tag{2.4}$$

where ν' are rest-frame frequencies measured by an observer in a comoving frame with the source and ν are observed frequencies measured by an observer that is receding in relation to the source at a redshift z.

Fitting a SED template to the measured photometry for a given source yields a model for its observed spectral density of flux $f(\nu)$ over a range of observed-frame frequencies. With that in hand, one can then compute the spectral density of flux f_{R} as measured by a given filter $R(\nu)$ in the observed-frame by means of the dimensionless convolution to ensure $f(\nu)$ and f_{R} are both written in the same units,

$$f_{R} = \int f(\nu)\, R(\nu)\, \frac{d\nu}{\nu}. \tag{2.5}$$

To correctly account for the expansion effects when computing the rest-frame spectral density of flux f'_{R} on the same passband R, one must first redshift the filter function $R(\nu)\ f(\nu)$ in the observed-frame back to the source's rest-frame frequencies $f(\nu')$. Given the source's measured redshift z, this can be done by means of Eq. (2.4), which yields $R(\nu') = R[(1+z)\nu]$. The rest frame $R(\nu')$, can then be convolved with the observed frame $f(\nu)$ to yield the spectral density of flux measured by the passband R at the source's rest frame as

$$f'_{R} = \int f(\nu)\, R[(1+z)\nu]\, \frac{d\nu}{\nu}. \tag{2.6}$$

Once f'_{R} is obtained, the k correction expressed in terms of densities of fluxes is then

$$k_{R} = \frac{f_{R}}{f'_{R}}. \tag{2.7}$$

We note that a similar expression is used by Blanton & Roweis (2007), based on the derivation for the k correction expressed in terms of magnitudes given in Hogg et al. (2002).

Next, we describe the use of the $1/V_{max}$ estimator, (Schmidt 1968), in the computation of the LF of the samples.

2.3 $1/V_{max}$ estimator

The $1/V_{max}$ (Schmidt 1968; Johnston 2011) estimator for the LF has the advantage of not assuming a parametric form in its calculation. It also yields directly the comoving number density normalisation. Recent results from Smith (2012) show that large-scale density variations can introduce systematic errors in the subsequent fitting of the parameters. Since we are dealing with different cosmological models that predict different density parameter evolutions, it is important to check how dependent the method itself is on the cosmology. We report in Appendix A how we built mock catalogues to check the effects of density variation, similar to what is done in Takeuchi et al. (2000), and check that this methodology is adequate for the purpose of the paper.

To compute the LF values using this method, we started by dividing each sample in redshift intervals Δz with centre values $\bar{z}$, and in luminosity bins ΔL with centre values $\bar{L}$. For each source in each ($\bar{z}$,$\bar{L}$) bin, we computed the maximum redshift at which it would still be included in the survey. Given the corresponding flux limit for the field where the source was detected ($f_{R,lim}$; Berta et al. 2011), its measured flux at that filter R (f_R) and its redshift (z) the highest redshift at which that source would still be included (ζ) can be obtained by means of the following relation[1],

$$f_{R,lim} = \left[\frac{d_L(z)}{d_L(\zeta)}\right]^2 f_R. \tag{2.8}$$

If the maximum redshift for a given source is outside the redshift interval it originally belongs to, we use the upper limit of this interval z_h as the maximum redshift instead. That is,

$$z_{max} = \min(z_h, \zeta). \tag{2.9}$$

The maximum comoving volume V_{max} enclosing each source is then

$$V_{max} = \sum_k \frac{S_k}{3} \int_{z_l}^{z_{max}} w_k(z)\, r(z)^2 \frac{dr}{dz} dz, \tag{2.10}$$

where the sum is over the k fields where the source would have been included; S_k is the area of the field where the source was detected, z_l the lower limit of the redshift interval at which the source is located, and $w_k(z)$ the incompleteness correction for the effective area of the source, corresponding to its computed flux, as a function of the redshift.

Although these corrections are computed from local simulations (z=0), and, therefore, they do not assume any cosmological model, the computed flux of each

[1]Since we are dealing with two observed-frame quantities, there is no need to include any k-corrections in the Eq. (2.8).

source as a function of the redshift depends on its luminosity distance, which may change with the cosmological model assumed. In addition to this implicit effect, the radial comoving distance r and its redshift derivative dr/dz also depend explicitly on the cosmology.

For each luminosity bin centred around $\bar{L}$ in each redshift interval centred around $\bar{z}$, we computed the $1/V_{max}$ estimator for the luminosity function in that bin $\phi_{\bar{z},\bar{L}}$ as

$$\phi_{\bar{z},\bar{L}} = \frac{1}{(\Delta L)_{\bar{L}}} \sum_{i=1}^{N_{\bar{z},\bar{L}}} \frac{1}{V_{max}^{i}}, \tag{2.11}$$

where $(\Delta L)_{\bar{L}}$ is the length of the luminosity bin centred on $\bar{L}$, and $N_{\bar{z},\bar{L}}$ the number of sources inside that luminosity bin and redshift interval.

Assuming Poisson uncertainties, the error bars $\delta\phi$ can be estimated simply by

$$\delta\phi_{\bar{z},\bar{L}} = \frac{1}{(\Delta L)_{\bar{L}}} \sqrt{\sum_{i=1}^{N_{\bar{z},\bar{L}}} \left(\frac{1}{V_{max}^{i}}\right)^{2}}. \tag{2.12}$$

2.4 Redshift evolution of the Schechter parameters

We computed the rest-frame monochromatic and total IR luminosity LF for sources in the combined fields, blind selected in the 100 μm and 160 μm bands, using the non-parametric $1/V_{max}$ method, both in the standard model and the GBH void models. The LF values are listed in Tables 2.1-2.12, up to redshifts $z \approx 3$ for the monochromatic LFs and up to $z \approx 4$ for the total IR ones.

We use the same binning in luminosity and redshift as in Gruppioni et al. (2013). The average values for the redshift intervals are 0.2, 0.6, 1.0, 1.5, 2.1, and 3.0, for the monochromatic LFs, and 0.2, 0.4, 0.5, 0.7, 0.9, 1.1, 1.5, 1.9, 2.2, 2.8, and 3.6 for the total IR LFs. The effective wavelengths will be 60 and 90 μm in the rest-frame LF. Because of the lack of enough $1/\mathrm{V}_{max}$ LF points to fit a Schechter function in the higher redshift bins, our analyses of the monochromatic luminosity functions are limited to intervals $\bar{z} \leq 3$. As a consistency check we compared our results for the standard model with those of Gruppioni et al. and the agreement is excellent.

The monochromatic and the total luminosity LFs are shown in Figs. 2.1-2.4 for the three cosmologies considered in this paper. When comparing the values in each luminosity bin it is clear that in void cosmologies the density is lower at the lowest luminosities. While at redshift larger than 0.8 the incompleteness at low luminosities does not allow any firm conclusion to be drawn, in the two lowest redshift bins the void models show LF values up to an order of magnitude lower than their ΛCDM

counterpart at L$\leq 10^{10}$L$_\odot$.

The resulting differences in the LF computed in the different models show up at the faint luminosity end of the luminosity functions. We use the Schechter analytical profile (Schechter 1976),

$$\varphi(L) = \frac{\phi^*}{L^*} \left(\frac{L}{L^*}\right)^{\alpha} e^{-L/L^*} = \varphi^* \left(\frac{L}{L^*}\right)^{\alpha} e^{-L/L^*}, \tag{2.13}$$

and fit it to the $1/V_{max}$ points over the ($\bar{z}$,$\bar{L}$) bins, where ϕ^* is the comoving number density normalisation, L^* the characteristic luminosity and α the faint-end slope, using the IDL routine MPFITFUN (Markwardt 2009) based on the Levenberg-Marquardt algorithm (Moré 1978). For each best-fit parameter, its formal 1-σ uncertainty is obtained by taking the square root of its corresponding element in the diagonal of the 3x3 covariance matrix of the fitting procedure, e.g., Richter (1995).

Since we are primarily interested in checking possible changes in the LF caused by the underlying cosmologies, we chose to use the classical Schechter function instead of the double exponential function (Saunders et al. 1990). The latter fits the FIR LF bright-end better, but the Schechter function has fewer free parameters that allows it to fit higher redshift intervals where the number of data points is small.

First we check for any variation of the α parameter with redshift, and find that it is consistent with no evolution. We test the incompleteness using the V_e/V_a tests (Avni & Bahcall 1980). A given ($\bar{z}$,$\bar{L}$) bin is considered complete by this test if its V_e/V_a value is 1/2. We find that the 1/V$_{max}$ LF points do not suffer from significant incompleteness at $\bar{z} = 0.2$, where the V_e/V_a values in the lowest luminosity bins of the monochromatic luminosity functions are 0.6 $\pm$ 0.1 and 0.5 $\pm$ 0.1 for the rest-frame 100 and 160 μm, respectively. These values become 0.15 $\pm$ 0.09 and 0.22 $\pm$ 0.03 at $\bar{z} = 1$, and 0.12 $\pm$ 0.05 and 0.11 $\pm$ 0.04 at $\bar{z} = 3$.

This is because at higher redshifts the flux limit of the observations corresponds to increasingly different luminosity limits, depending on the SED of the sources, leading to an incompleteness in the lower luminosity bins that is dependent on the galaxy type (Ilbert et al. 2004). Because of this we chose to fix the α parameter to its value in the lower redshift interval in the fits presented in Tables 2.13-2.16. We plot the redshift evolution of these two parameters in Fig. 2.5.

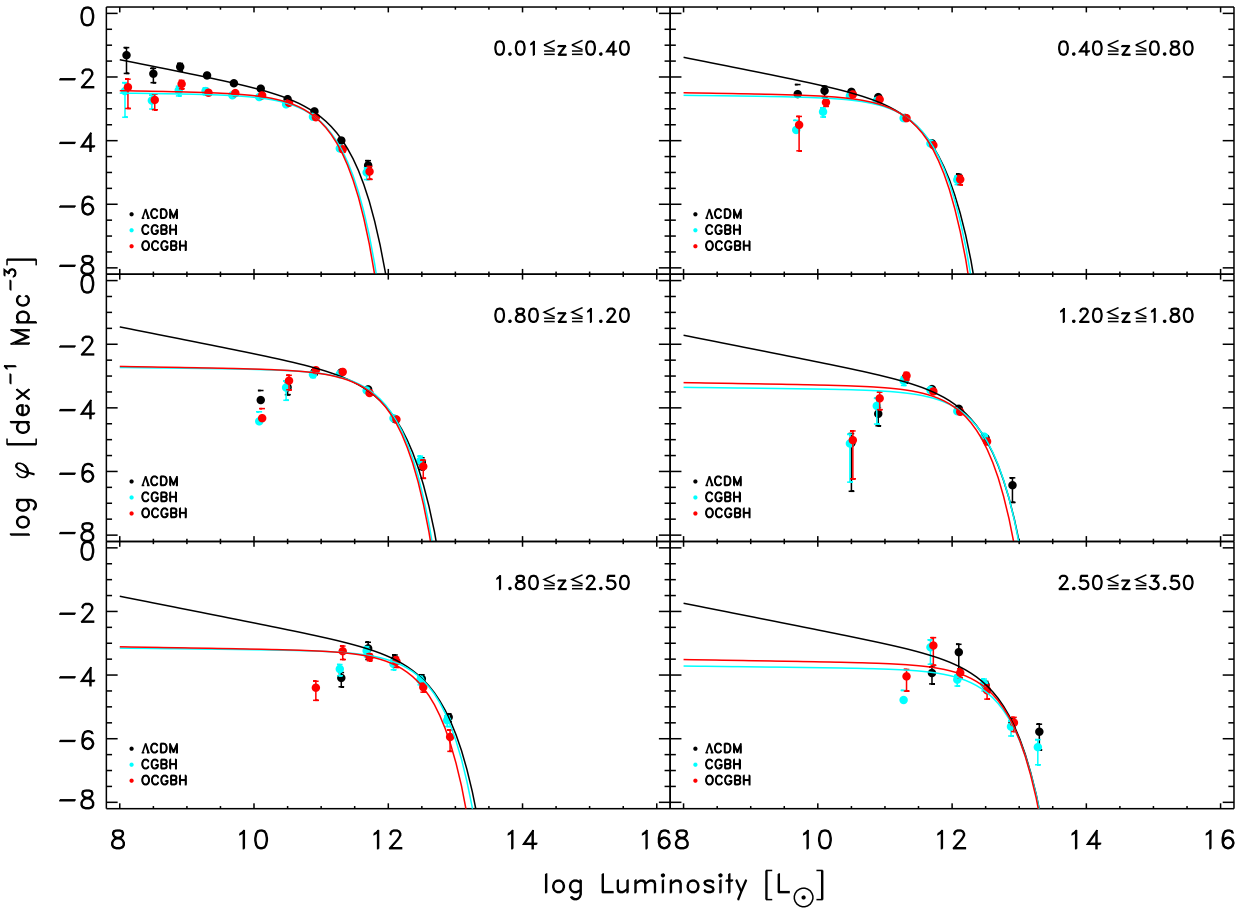

Figure 2.1: Luminosity functions derived in the standard (ΛCDM) (black dots) and the void (GBH) cosmological models (red and cyan dots). We show also the best-fit Schechter profiles to the rest-frame 100 μm $1/V_{max}$ corresponding to effective wavelengths of 60 μm.

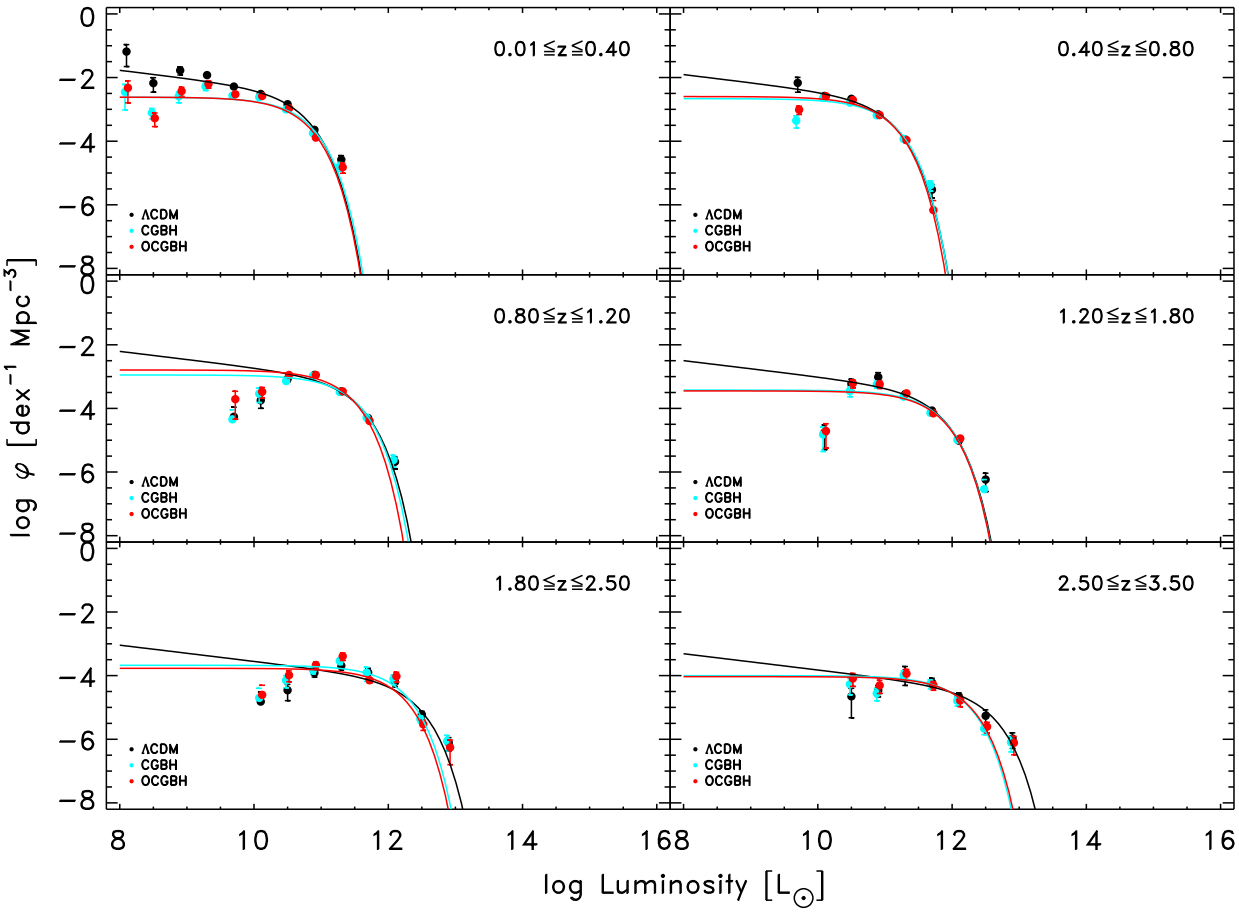

Figure 2.2: As Figure 2.1 for the rest-frame 160 μm $1/V_{max}$ luminosity functions. Here the effective wavelength is 90μm.

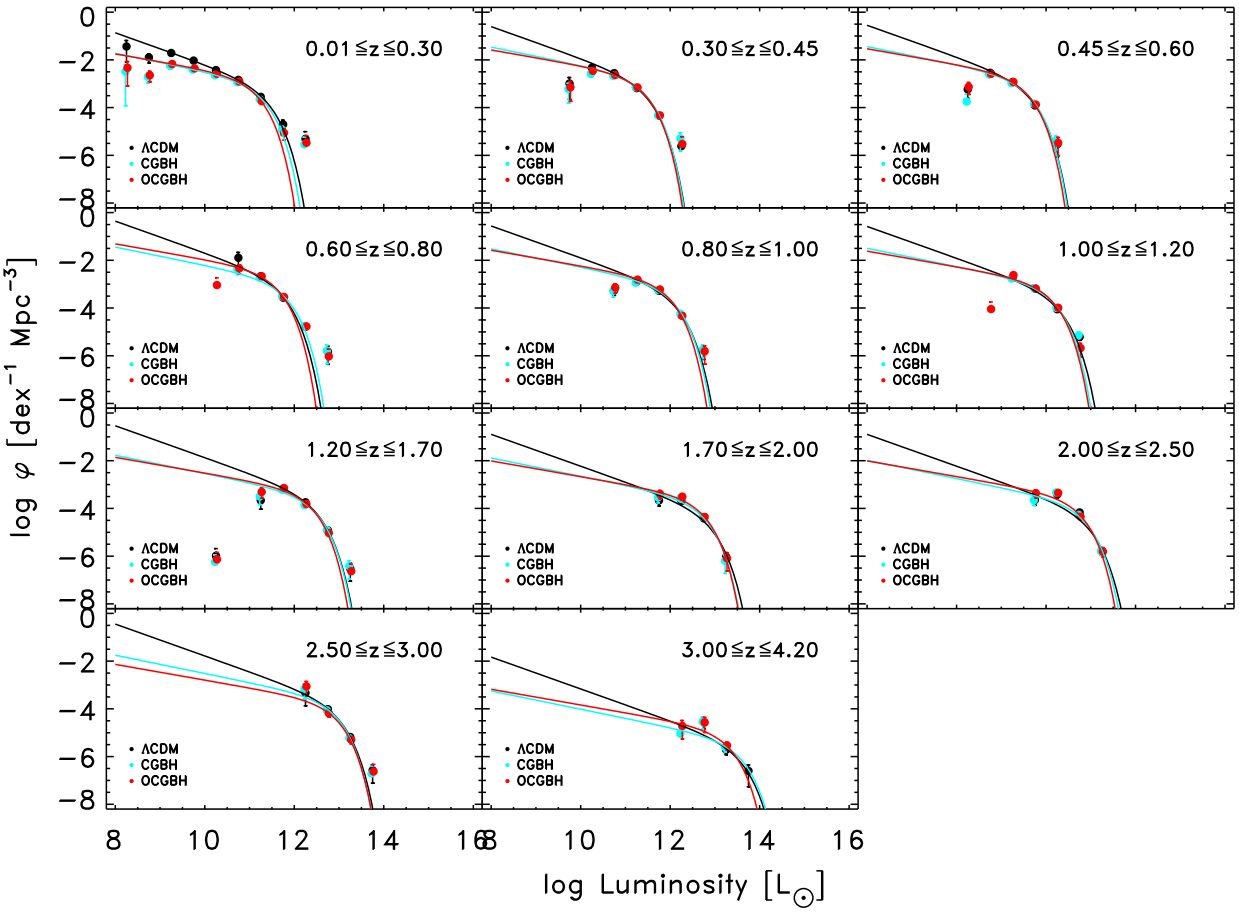

Figure 2.3: Schechter profile fits to the rest-frame total IR luminosity functions computed from the PACS 100 μm $1/V_{max}$ band, assuming the standard (ΛCDM) and the void (GBH) cosmological models.

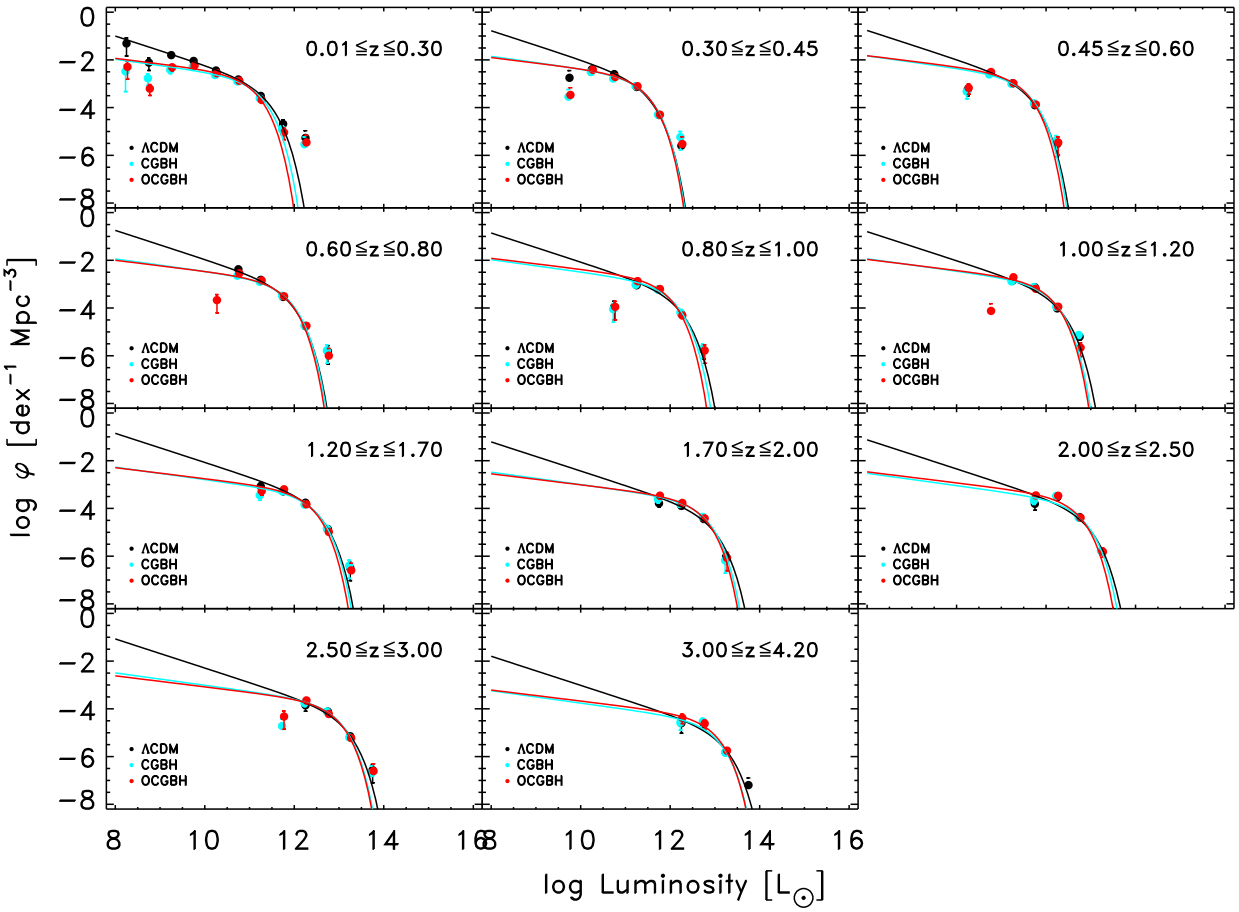

Figure 2.4: Schechter profile fits to the rest-frame total IR luminosity functions computed from the PACS 160 μm $1/V_{max}$ band, assuming the standard (ΛCDM) and the void (GBH) cosmological models.

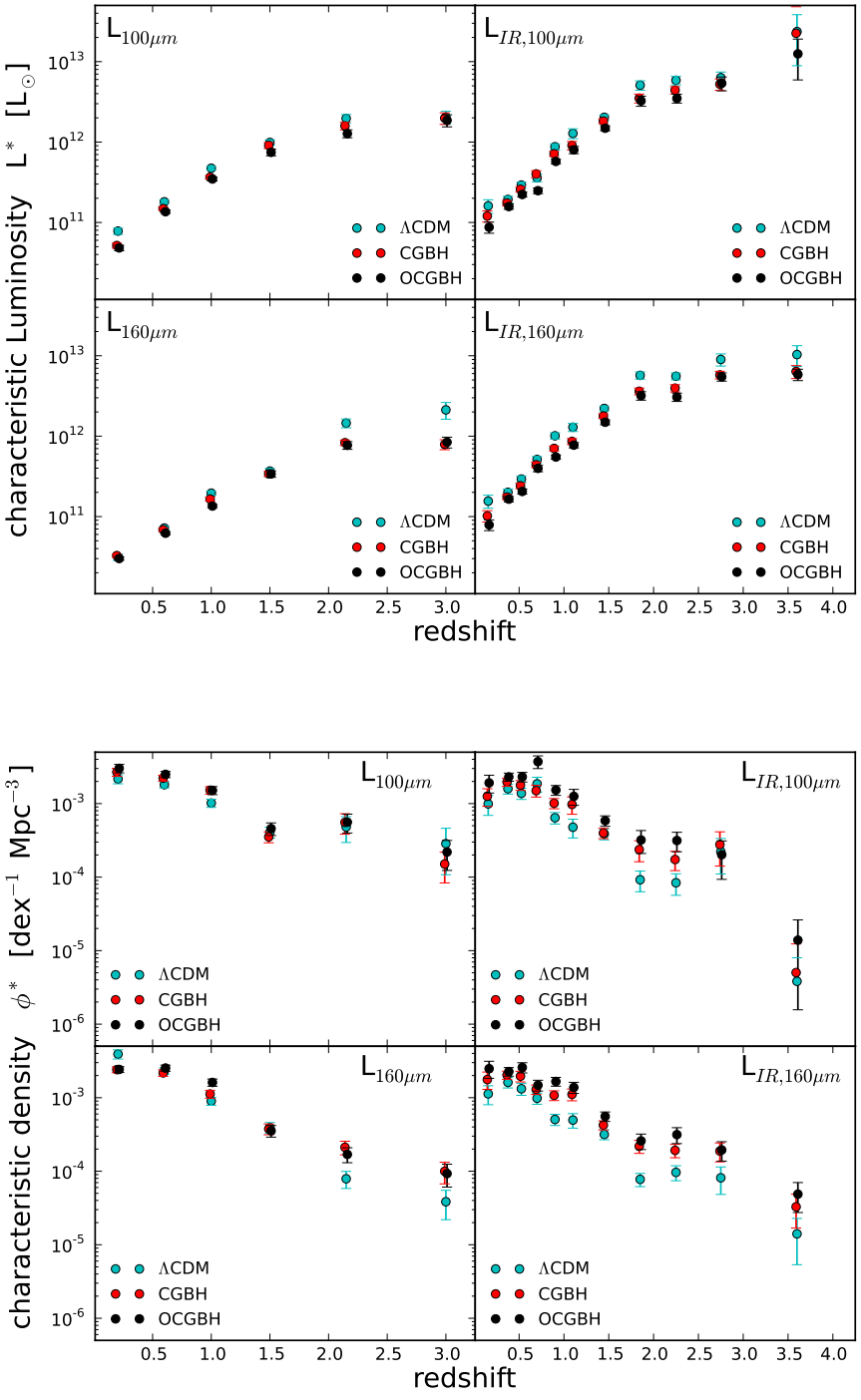

Figure 2.5: *Upper panel:* Redshift evolution of the characteristic luminosity L^* on the four datasets of the present work. *Lower panel:* Redshift evolution of the characteristic luminosity ϕ^* on the same datasets.

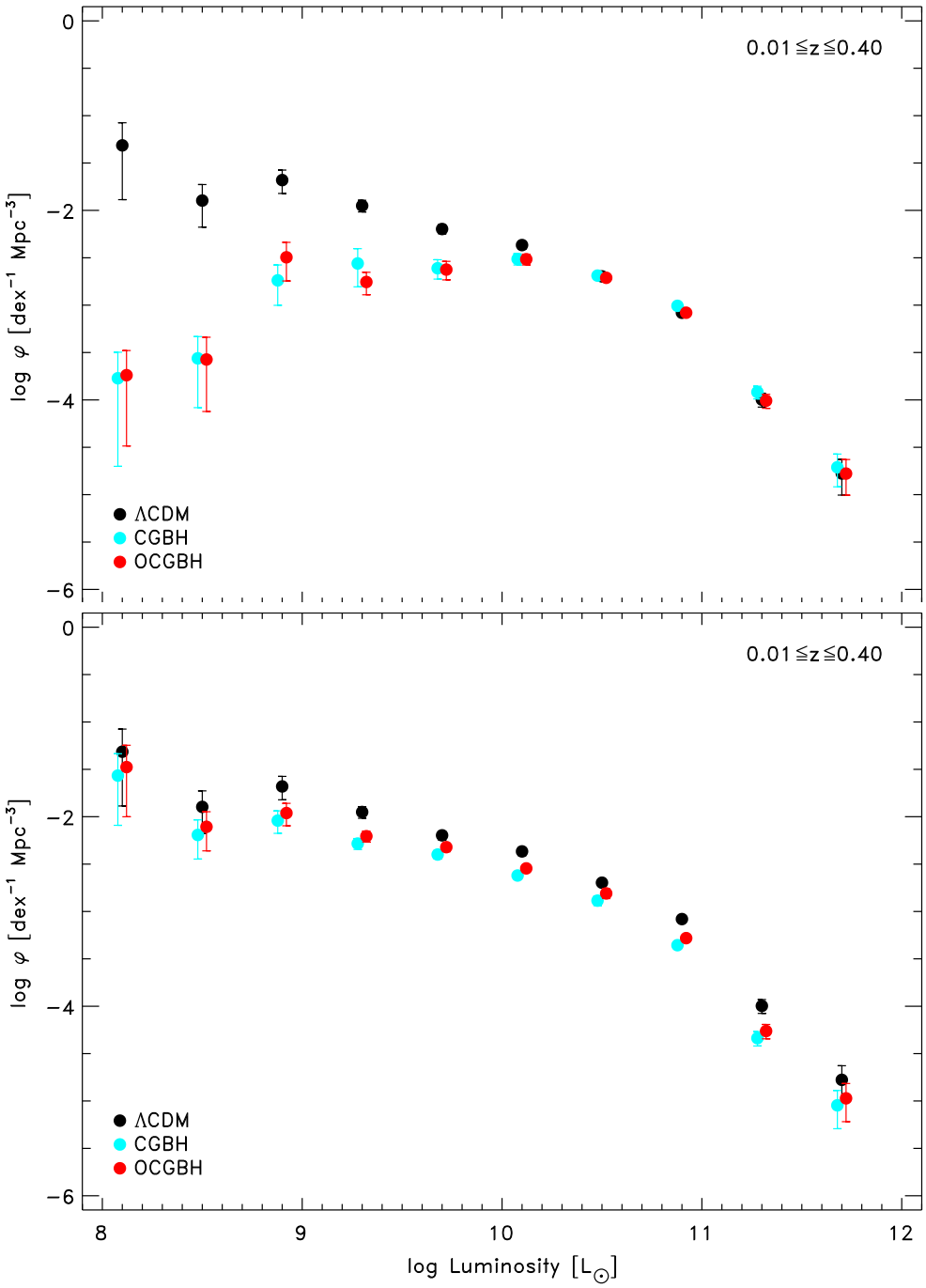

Figure 2.6: *Upper panel:* Effect of the luminosity distance - redshift relation on the shape of the LF. The black points were computed using the $1/V_{max}$ method, assuming both $d_L(z)$ and $r(z)$ relations stemming from the standard model, while the blue and red points kept the $r(z)$ relation for the ΛCDM model, changing only the $d_L(z)$ relation for that in the listed void model. The effect of the $d_L(z)$ relation on the shape of the LF is clear, especially at the lower luminosity bins. *Lower panel:* Effect of the comoving distance - redshift relation on the shape of the LF. The black points were computed using the $1/V_{max}$ method, assuming both $d_L(z)$ and $r(z)$ relations stemming from the standard model, while the blue and red points kept the $d_L(z)$ relation for the ΛCDM model, changing only the $r(z)$ relation for that in the listed void model. The effect of the $r(z)$ relation on the shape of the LF is found to be much less relevant than that of the $d_L(z)$ relation.

Table 2.1: Rest-frame 100 μm $1/V_{max}$ Luminosity Function assuming the ΛCDM cosmological model. Units are dex^{-1} Mpc^{-3}.

	Average redshift					
Luminosity [$L_\odot$]	0.2	0.6	1.0	1.5	2.1	3.0
5.0E+07	$(4.6 \pm 3.3) \times 10^{-2}$					
1.3E+08	$(4.9 \pm 3.6) \times 10^{-2}$					
3.2E+08	$(1.3 \pm 0.6) \times 10^{-2}$					
7.9E+08	$(2.1 \pm 0.6) \times 10^{-2}$					
2.0E+09	$(1.1 \pm 0.2) \times 10^{-2}$					
5.0E+09	$(6.4 \pm 0.7) \times 10^{-3}$	$(2.9 \pm 2.9) \times 10^{-3}$				
1.3E+10	$(4.3 \pm 0.4) \times 10^{-3}$	$(3.7 \pm 1.5) \times 10^{-3}$	$(1.8 \pm 1.8) \times 10^{-4}$			
3.2E+10	$(2.01 \pm 0.09) \times 10^{-3}$	$(3.4 \pm 0.4) \times 10^{-3}$	$(4.4 \pm 1.8) \times 10^{-4}$	$(7.9 \pm 7.6) \times 10^{-6}$		
7.9E+10	$(8.3 \pm 0.5) \times 10^{-4}$	$(2.3 \pm 0.2) \times 10^{-3}$	$(1.3 \pm 0.2) \times 10^{-3}$	$(6.5 \pm 3.8) \times 10^{-5}$		
2.0E+11	$(1.0 \pm 0.2) \times 10^{-4}$	$(5.2 \pm 0.2) \times 10^{-4}$	$(1.3 \pm 0.2) \times 10^{-3}$	$(8.0 \pm 1.9) \times 10^{-4}$	$(8.1 \pm 3.9) \times 10^{-5}$	
5.0E+11	$(1.7 \pm 0.7) \times 10^{-5}$	$(8.2 \pm 0.7) \times 10^{-5}$	$(3.8 \pm 0.4) \times 10^{-4}$	$(3.9 \pm 0.6) \times 10^{-4}$	$(6.9 \pm 3.8) \times 10^{-4}$	$(1.2 \pm 0.6) \times 10^{-4}$
1.3E+12		$(6.8 \pm 2.0) \times 10^{-6}$	$(4.4 \pm 0.4) \times 10^{-5}$	$(9.3 \pm 0.9) \times 10^{-5}$	$(3.1 \pm 1.2) \times 10^{-4}$	$(5.2 \pm 4.1) \times 10^{-4}$
3.2E+12			$(1.9 \pm 0.8) \times 10^{-6}$	$(1.1 \pm 0.2) \times 10^{-5}$	$(7.7 \pm 2.6) \times 10^{-5}$	$(4.8 \pm 1.5) \times 10^{-5}$
7.9E+12				$(3.7 \pm 2.6) \times 10^{-7}$	$(4.8 \pm 1.3) \times 10^{-6}$	$(3.3 \pm 1.0) \times 10^{-6}$
2.0E+13						$(1.7 \pm 1.2) \times 10^{-6}$

Table 2.2: Rest-frame 100 μm $1/V_{max}$ Luminosity Function assuming the CGBH cosmological model. Units are dex^{-1} Mpc^{-3}.

	Average redshift					
Luminosity [$L_\odot$]	0.2	0.6	1.0	1.5	2.1	3.0
5.0E+07	$(2.8 \pm 1.6) \times 10^{-3}$					
1.3E+08	$(3.6 \pm 3.1) \times 10^{-3}$					
3.2E+08	$(1.8 \pm 0.8) \times 10^{-3}$					
7.9E+08	$(3.8 \pm 1.3) \times 10^{-3}$					
2.0E+09	$(3.6 \pm 0.9) \times 10^{-3}$					
5.0E+09	$(2.7 \pm 0.4) \times 10^{-3}$	$(2.2 \pm 2.2) \times 10^{-4}$				
1.3E+10	$(2.3 \pm 0.2) \times 10^{-3}$	$(8.1 \pm 2.5) \times 10^{-4}$	$(3.8 \pm 3.8) \times 10^{-5}$			
3.2E+10	$(1.4 \pm 0.1) \times 10^{-3}$	$(2.6 \pm 0.4) \times 10^{-3}$	$(4.3 \pm 2.6) \times 10^{-4}$	$(7.6 \pm 7.1) \times 10^{-6}$		
7.9E+10	$(5.6 \pm 0.4) \times 10^{-4}$	$(1.8 \pm 0.2) \times 10^{-3}$	$(1.1 \pm 0.2) \times 10^{-3}$	$(1.2 \pm 0.8) \times 10^{-4}$		
2.0E+11	$(5.7 \pm 0.9) \times 10^{-5}$	$(5.1 \pm 0.3) \times 10^{-4}$	$(1.1 \pm 0.1) \times 10^{-3}$	$(7.2 \pm 2.1) \times 10^{-4}$	$(1.5 \pm 0.6) \times 10^{-4}$	$(1.6 \pm 1.6) \times 10^{-5}$
5.0E+11	$(1.0 \pm 0.4) \times 10^{-5}$	$(8.2 \pm 0.7) \times 10^{-5}$	$(3.5 \pm 0.4) \times 10^{-4}$	$(3.6 \pm 0.5) \times 10^{-4}$	$(5.8 \pm 2.1) \times 10^{-4}$	$(7.5 \pm 5.3) \times 10^{-4}$
1.3E+12		$(5.9 \pm 1.7) \times 10^{-6}$	$(4.7 \pm 0.4) \times 10^{-5}$	$(7.8 \pm 0.6) \times 10^{-5}$	$(2.2 \pm 0.8) \times 10^{-4}$	$(7.2 \pm 2.7) \times 10^{-5}$
3.2E+12			$(2.2 \pm 0.9) \times 10^{-6}$	$(1.2 \pm 0.2) \times 10^{-5}$	$(7.0 \pm 2.1) \times 10^{-5}$	$(5.3 \pm 2.2) \times 10^{-5}$
7.9E+12					$(3.8 \pm 1.4) \times 10^{-6}$	$(2.4 \pm 1.2) \times 10^{-6}$
2.0E+13						$(5.4 \pm 3.9) \times 10^{-7}$

Table 2.3: Rest-frame 100 μm $1/V_{max}$ Luminosity Function assuming the OCGBH cosmological model. Units are dex^{-1} Mpc^{-3}.

	Average redshift					
Luminosity [$L_\odot$]	0.2	0.6	1.0	1.5	2.1	3.0
5.0E+07	$(2.2 \pm 1.6) \times 10^{-3}$					
1.3E+08	$(4.8 \pm 3.8) \times 10^{-3}$					
3.2E+08	$(1.9 \pm 1.0) \times 10^{-3}$					
7.9E+08	$(6.0 \pm 1.8) \times 10^{-3}$					
2.0E+09	$(3.2 \pm 0.5) \times 10^{-3}$					
5.0E+09	$(3.1 \pm 0.4) \times 10^{-3}$	$(3.1 \pm 2.6) \times 10^{-4}$				
1.3E+10	$(2.7 \pm 0.2) \times 10^{-3}$	$(1.6 \pm 0.4) \times 10^{-3}$	$(4.7 \pm 4.7) \times 10^{-5}$			
3.2E+10	$(1.5 \pm 0.2) \times 10^{-3}$	$(2.8 \pm 0.4) \times 10^{-3}$	$(7.1 \pm 3.4) \times 10^{-4}$	$(9.7 \pm 9.1) \times 10^{-6}$		
7.9E+10	$(5.4 \pm 0.4) \times 10^{-4}$	$(2.0 \pm 0.2) \times 10^{-3}$	$(1.5 \pm 0.3) \times 10^{-3}$	$(2.0 \pm 1.1) \times 10^{-4}$	$(4.0 \pm 2.4) \times 10^{-5}$	
2.0E+11	$(5.4 \pm 0.9) \times 10^{-5}$	$(5.1 \pm 0.3) \times 10^{-4}$	$(1.3 \pm 0.2) \times 10^{-3}$	$(1.0 \pm 0.3) \times 10^{-3}$	$(5.6 \pm 2.5) \times 10^{-4}$	$(9.1 \pm 6.0) \times 10^{-5}$
5.0E+11	$(1.1 \pm 0.5) \times 10^{-5}$	$(7.2 \pm 0.7) \times 10^{-5}$	$(2.9 \pm 0.3) \times 10^{-4}$	$(3.3 \pm 0.5) \times 10^{-4}$	$(3.7 \pm 0.9) \times 10^{-4}$	$(8.5 \pm 6.5) \times 10^{-4}$
1.3E+12		$(6.0 \pm 1.9) \times 10^{-6}$	$(4.3 \pm 0.5) \times 10^{-5}$	$(7.5 \pm 0.6) \times 10^{-5}$	$(2.7 \pm 0.9) \times 10^{-4}$	$(1.2 \pm 0.4) \times 10^{-4}$
3.2E+12			$(1.4 \pm 0.8) \times 10^{-6}$	$(8.8 \pm 1.7) \times 10^{-6}$	$(4.2 \pm 1.3) \times 10^{-5}$	$(3.3 \pm 1.6) \times 10^{-5}$
7.9E+12					$(1.1 \pm 0.7) \times 10^{-6}$	$(3.2 \pm 1.5) \times 10^{-6}$
2.0E+13						

Table 2.4: Rest-frame 160 μm $1/V_{max}$ Luminosity Function assuming the ΛCDM cosmological model. Units are dex^{-1} Mpc^{-3}.

	Average redshift					
Luminosity [$L_\odot$]	0.2	0.6	1.0	1.5	2.1	3.0
5.0E+07	$(4.9 \pm 2.8) \times 10^{-2}$					
1.3E+08	$(6.6 \pm 4.3) \times 10^{-2}$					
3.2E+08	$(6.7 \pm 3.2) \times 10^{-3}$					
7.9E+08	$(1.7 \pm 0.5) \times 10^{-2}$					
2.0E+09	$(1.2 \pm 0.2) \times 10^{-2}$					
5.0E+09	$(5.2 \pm 0.6) \times 10^{-3}$	$(6.8 \pm 3.3) \times 10^{-3}$	$(5.4 \pm 5.4) \times 10^{-5}$			
1.3E+10	$(3.0 \pm 0.3) \times 10^{-3}$	$(2.7 \pm 0.4) \times 10^{-3}$	$(1.8 \pm 0.8) \times 10^{-4}$	$(1.8 \pm 1.3) \times 10^{-5}$	$(1.5 \pm 1.5) \times 10^{-5}$	
3.2E+10	$(1.45 \pm 0.07) \times 10^{-3}$	$(2.1 \pm 0.2) \times 10^{-3}$	$(8.4 \pm 1.5) \times 10^{-4}$	$(5.9 \pm 2.3) \times 10^{-4}$	$(3.5 \pm 1.8) \times 10^{-5}$	$(2.2 \pm 1.8) \times 10^{-5}$
7.9E+10	$(2.3 \pm 0.3) \times 10^{-4}$	$(7.0 \pm 0.4) \times 10^{-4}$	$(1.1 \pm 0.1) \times 10^{-3}$	$(9.6 \pm 3.7) \times 10^{-4}$	$(1.2 \pm 0.3) \times 10^{-4}$	$(3.5 \pm 1.3) \times 10^{-5}$
2.0E+11	$(2.6 \pm 0.9) \times 10^{-5}$	$(1.13 \pm 0.08) \times 10^{-4}$	$(3.4 \pm 0.4) \times 10^{-4}$	$(2.8 \pm 0.4) \times 10^{-4}$	$(2.0 \pm 0.5) \times 10^{-4}$	$(1.2 \pm 0.7) \times 10^{-4}$
5.0E+11		$(3.0 \pm 1.3) \times 10^{-6}$	$(5.0 \pm 0.6) \times 10^{-5}$	$(8.6 \pm 1.1) \times 10^{-5}$	$(1.2 \pm 0.5) \times 10^{-4}$	$(6.1 \pm 2.2) \times 10^{-5}$
1.3E+12			$(2.1 \pm 0.9) \times 10^{-6}$	$(9.7 \pm 1.6) \times 10^{-6}$	$(6.3 \pm 1.9) \times 10^{-5}$	$(2.2 \pm 0.6) \times 10^{-5}$
3.2E+12				$(5.8 \pm 3.4) \times 10^{-7}$	$(6.0 \pm 1.6) \times 10^{-6}$	$(5.5 \pm 3.0) \times 10^{-6}$
7.9E+12					$(7.8 \pm 3.5) \times 10^{-7}$	$(1.1 \pm 0.5) \times 10^{-6}$
2.0E+13						

Table 2.5: Rest-frame 160 μm $1/V_{max}$ Luminosity Function assuming the CGBH cosmological model. Units are dex^{-1} Mpc^{-3}.

	Average redshift					
Luminosity [$L_\odot$]	0.2	0.6	1.0	1.5	2.1	3.0
5.0E+07	$(2.3 \pm 1.4) \times 10^{-3}$					
1.3E+08	$(3.5 \pm 2.6) \times 10^{-3}$					
3.2E+08	$(7.8 \pm 2.8) \times 10^{-4}$					
7.9E+08	$(2.6 \pm 1.0) \times 10^{-3}$					
2.0E+09	$(5.3 \pm 1.4) \times 10^{-3}$					
5.0E+09	$(2.7 \pm 0.4) \times 10^{-3}$	$(4.4 \pm 1.8) \times 10^{-4}$	$(4.5 \pm 4.5) \times 10^{-5}$			
1.3E+10	$(2.4 \pm 0.2) \times 10^{-3}$	$(2.3 \pm 0.3) \times 10^{-3}$	$(2.9 \pm 1.4) \times 10^{-4}$	$(1.5 \pm 1.1) \times 10^{-5}$	$(2.0 \pm 2.0) \times 10^{-5}$	
3.2E+10	$(1.0 \pm 0.1) \times 10^{-3}$	$(1.6 \pm 0.2) \times 10^{-3}$	$(7.2 \pm 1.2) \times 10^{-4}$	$(3.5 \pm 1.2) \times 10^{-4}$	$(7.1 \pm 2.9) \times 10^{-5}$	$(5.3 \pm 2.8) \times 10^{-5}$
7.9E+10	$(1.8 \pm 0.2) \times 10^{-4}$	$(6.5 \pm 0.4) \times 10^{-4}$	$(1.1 \pm 0.1) \times 10^{-3}$	$(5.7 \pm 1.4) \times 10^{-4}$	$(1.5 \pm 0.4) \times 10^{-4}$	$(2.8 \pm 1.2) \times 10^{-5}$
2.0E+11	$(1.6 \pm 0.5) \times 10^{-5}$	$(1.18 \pm 0.08) \times 10^{-4}$	$(3.3 \pm 0.4) \times 10^{-4}$	$(2.3 \pm 0.3) \times 10^{-4}$	$(2.9 \pm 0.7) \times 10^{-4}$	$(1.0 \pm 0.4) \times 10^{-4}$
5.0E+11		$(4.1 \pm 1.5) \times 10^{-6}$	$(5.1 \pm 0.6) \times 10^{-5}$	$(7.2 \pm 1.0) \times 10^{-5}$	$(1.2 \pm 0.6) \times 10^{-4}$	$(5.6 \pm 1.7) \times 10^{-5}$
1.3E+12			$(2.4 \pm 1.0) \times 10^{-6}$	$(1.0 \pm 0.2) \times 10^{-5}$	$(7.8 \pm 2.6) \times 10^{-5}$	$(1.6 \pm 0.5) \times 10^{-5}$
3.2E+12				$(2.9 \pm 2.9) \times 10^{-7}$	$(4.3 \pm 1.1) \times 10^{-6}$	$(2.2 \pm 0.8) \times 10^{-6}$
7.9E+12					$(8.8 \pm 4.4) \times 10^{-7}$	$(8.1 \pm 4.1) \times 10^{-7}$
2.0E+13						

Table 2.6: Rest-frame 160 μm $1/V_{max}$ Luminosity Function assuming the OCGBH cosmological model. Units are dex^{-1} Mpc^{-3}.

	Average redshift					
Luminosity [$L_\odot$]	0.2	0.6	1.0	1.5	2.1	3.0
5.0E+07	$(2.9 \pm 1.8) \times 10^{-3}$					
1.3E+08	$(4.7 \pm 3.1) \times 10^{-3}$					
3.2E+08	$(5.3 \pm 2.4) \times 10^{-4}$					
7.9E+08	$(3.7 \pm 1.2) \times 10^{-3}$					
2.0E+09	$(6.3 \pm 1.6) \times 10^{-3}$					
5.0E+09	$(3.0 \pm 0.4) \times 10^{-3}$	$(9.7 \pm 2.8) \times 10^{-4}$	$(2.0 \pm 1.5) \times 10^{-4}$			
1.3E+10	$(2.6 \pm 0.2) \times 10^{-3}$	$(2.6 \pm 0.4) \times 10^{-3}$	$(3.3 \pm 1.2) \times 10^{-4}$	$(1.9 \pm 1.4) \times 10^{-5}$	$(2.5 \pm 2.5) \times 10^{-5}$	
3.2E+10	$(1.08 \pm 0.06) \times 10^{-3}$	$(2.0 \pm 0.2) \times 10^{-3}$	$(1.1 \pm 0.2) \times 10^{-3}$	$(6.2 \pm 1.8) \times 10^{-4}$	$(1.0 \pm 0.4) \times 10^{-4}$	$(8.2 \pm 3.6) \times 10^{-5}$
7.9E+10	$(1.3 \pm 0.2) \times 10^{-4}$	$(6.6 \pm 0.4) \times 10^{-4}$	$(1.1 \pm 0.1) \times 10^{-3}$	$(5.7 \pm 1.5) \times 10^{-4}$	$(2.2 \pm 0.5) \times 10^{-4}$	$(4.9 \pm 2.2) \times 10^{-5}$
2.0E+11	$(1.5 \pm 0.5) \times 10^{-5}$	$(1.07 \pm 0.09) \times 10^{-4}$	$(3.4 \pm 0.4) \times 10^{-4}$	$(3.0 \pm 0.4) \times 10^{-4}$	$(4.1 \pm 1.1) \times 10^{-4}$	$(1.2 \pm 0.4) \times 10^{-4}$
5.0E+11		$(6.8 \pm 6.8) \times 10^{-7}$	$(4.0 \pm 0.5) \times 10^{-5}$	$(7.0 \pm 0.7) \times 10^{-5}$	$(7.2 \pm 1.3) \times 10^{-5}$	$(5.0 \pm 1.5) \times 10^{-5}$
1.3E+12				$(1.1 \pm 0.2) \times 10^{-5}$	$(9.5 \pm 3.2) \times 10^{-5}$	$(1.7 \pm 0.6) \times 10^{-5}$
3.2E+12					$(2.9 \pm 1.0) \times 10^{-6}$	$(2.5 \pm 0.9) \times 10^{-6}$
7.9E+12					$(5.5 \pm 3.9) \times 10^{-7}$	$(7.8 \pm 4.5) \times 10^{-7}$
2.0E+13						

Table 2.7: Rest-frame total IR $1/V_{max}$ Luminosity Function in the PACS 100 μm band, assuming the ΛCDM cosmological model. Units are dex^{-1} Mpc^{-3}.

	Average redshift										
Luminosity [$L_\odot$]	0.2	0.4	0.5	0.7	0.9	1.1	1.5	1.9	2.2	2.8	3.6
1.8E+08	$(3.7 \pm 2.8) \times 10^{-2}$										
5.6E+08	$(1.3 \pm 0.5) \times 10^{-2}$										
1.8E+09	$(1.9 \pm 0.5) \times 10^{-2}$										
5.6E+09	$(9.3 \pm 1.3) \times 10^{-3}$	$(1.0 \pm 0.8) \times 10^{-3}$									
1.8E+10	$(3.7 \pm 0.3) \times 10^{-3}$	$(4.7 \pm 1.1) \times 10^{-3}$	$(5.8 \pm 3.4) \times 10^{-4}$				$(1.0 \pm 1.0) \times 10^{-6}$				
5.6E+10	$(1.46 \pm 0.09) \times 10^{-3}$	$(2.8 \pm 0.2) \times 10^{-3}$	$(2.9 \pm 0.5) \times 10^{-3}$	$(1.3 \pm 0.9) \times 10^{-2}$	$(5.6 \pm 2.2) \times 10^{-4}$						
1.8E+11	$(2.8 \pm 0.4) \times 10^{-4}$	$(6.6 \pm 0.4) \times 10^{-4}$	$(1.2 \pm 0.1) \times 10^{-3}$	$(2.1 \pm 0.2) \times 10^{-3}$	$(1.3 \pm 0.2) \times 10^{-3}$	$(1.9 \pm 0.5) \times 10^{-3}$	$(2.2 \pm 1.2) \times 10^{-4}$				
5.6E+11	$(2.0 \pm 1.0) \times 10^{-5}$	$(4.6 \pm 1.1) \times 10^{-5}$	$(1.2 \pm 0.1) \times 10^{-4}$	$(2.7 \pm 0.2) \times 10^{-4}$	$(5.3 \pm 0.5) \times 10^{-4}$	$(6.6 \pm 1.1) \times 10^{-4}$	$(6.7 \pm 1.0) \times 10^{-4}$	$(2.2 \pm 0.9) \times 10^{-4}$	$(2.3 \pm 0.9) \times 10^{-4}$		
1.8E+12	$(4.9 \pm 4.9) \times 10^{-6}$	$(2.4 \pm 2.4) \times 10^{-6}$	$(2.9 \pm 2.1) \times 10^{-6}$	$(1.7 \pm 0.4) \times 10^{-5}$	$(5.0 \pm 0.5) \times 10^{-5}$	$(8.9 \pm 0.7) \times 10^{-5}$	$(1.8 \pm 0.2) \times 10^{-4}$	$(2.1 \pm 0.5) \times 10^{-4}$	$(3.9 \pm 1.2) \times 10^{-4}$	$(4.6 \pm 3.3) \times 10^{-4}$	
5.6E+12				$(1.5 \pm 1.1) \times 10^{-6}$	$(1.7 \pm 1.0) \times 10^{-6}$	$(6.1 \pm 1.7) \times 10^{-6}$	$(1.2 \pm 0.1) \times 10^{-5}$	$(3.9 \pm 0.8) \times 10^{-5}$	$(6.8 \pm 1.4) \times 10^{-5}$	$(9.8 \pm 2.7) \times 10^{-5}$	$(2.8 \pm 1.4) \times 10^{-5}$
1.8E+13							$(3.0 \pm 2.1) \times 10^{-7}$	$(9.5 \pm 4.7) \times 10^{-7}$	$(1.7 \pm 0.5) \times 10^{-6}$	$(6.6 \pm 1.6) \times 10^{-6}$	$(1.9 \pm 0.7) \times 10^{-6}$

Table 2.8: Rest-frame total IR $1/V_{max}$ Luminosity Function in the PACS 160 μm band, assuming the ΛCDM cosmological model. Units are dex^{-1} Mpc^{-3}.

	Average redshift										
Luminosity [$L_\odot$]	0.2	0.4	0.5	0.7	0.9	1.1	1.5	1.9	2.2	2.8	3.6
1.8E+08	$(4.9 \pm 3.5) \times 10^{-2}$										
5.6E+08	$(7.7 \pm 4.1) \times 10^{-3}$										
1.8E+09	$(1.6 \pm 0.4) \times 10^{-2}$										
5.6E+09	$(9.0 \pm 1.3) \times 10^{-3}$	$(1.8 \pm 1.8) \times 10^{-3}$									
1.8E+10	$(3.6 \pm 0.3) \times 10^{-3}$	$(4.0 \pm 1.0) \times 10^{-3}$	$(5.8 \pm 2.7) \times 10^{-4}$								
5.6E+10	$(1.51 \pm 0.09) \times 10^{-3}$	$(2.5 \pm 0.3) \times 10^{-3}$	$(2.8 \pm 0.4) \times 10^{-3}$	$(4.2 \pm 1.3) \times 10^{-3}$	$(1.1 \pm 0.8) \times 10^{-4}$						
1.8E+11	$(3.1 \pm 0.4) \times 10^{-4}$	$(7.3 \pm 0.5) \times 10^{-4}$	$(1.0 \pm 0.1) \times 10^{-3}$	$(1.5 \pm 0.2) \times 10^{-3}$	$(9.0 \pm 1.5) \times 10^{-4}$	$(1.4 \pm 0.3) \times 10^{-3}$	$(8.5 \pm 3.4) \times 10^{-4}$				
5.6E+11	$(2.1 \pm 1.0) \times 10^{-5}$	$(4.9 \pm 1.1) \times 10^{-5}$	$(1.3 \pm 0.1) \times 10^{-4}$	$(2.9 \pm 0.2) \times 10^{-4}$	$(6.1 \pm 0.6) \times 10^{-4}$	$(7.4 \pm 1.0) \times 10^{-4}$	$(5.2 \pm 0.7) \times 10^{-4}$	$(1.6 \pm 0.5) \times 10^{-4}$	$(1.6 \pm 0.7) \times 10^{-4}$		
1.8E+12	$(5.4 \pm 5.4) \times 10^{-6}$	$(2.5 \pm 2.5) \times 10^{-6}$	$(3.0 \pm 2.1) \times 10^{-6}$	$(1.7 \pm 0.4) \times 10^{-5}$	$(5.7 \pm 0.6) \times 10^{-5}$	$(9.6 \pm 0.7) \times 10^{-5}$	$(1.7 \pm 0.2) \times 10^{-4}$	$(1.3 \pm 0.3) \times 10^{-4}$	$(2.9 \pm 0.5) \times 10^{-4}$	$(1.4 \pm 0.6) \times 10^{-4}$	$(2.5 \pm 1.6) \times 10^{-5}$
5.6E+12				$(1.5 \pm 1.1) \times 10^{-6}$	$(1.7 \pm 1.0) \times 10^{-6}$	$(6.3 \pm 1.7) \times 10^{-6}$	$(1.4 \pm 0.2) \times 10^{-5}$	$(3.6 \pm 0.3) \times 10^{-5}$	$(4.4 \pm 0.6) \times 10^{-5}$	$(7.7 \pm 1.8) \times 10^{-5}$	$(2.5 \pm 0.8) \times 10^{-5}$
1.8E+13							$(3.2 \pm 2.3) \times 10^{-7}$	$(9.6 \pm 4.8) \times 10^{-7}$	$(1.6 \pm 0.5) \times 10^{-6}$	$(7.1 \pm 1.1) \times 10^{-6}$	$(1.6 \pm 0.5) \times 10^{-6}$

Table 2.9: Rest-frame total IR $1/V_{max}$ Luminosity Function in the PACS 100 μm band, assuming the CGBH cosmological model. Units are dex^{-1} Mpc^{-3}.

	Average redshift										
Luminosity [$L_\odot$]	0.2	0.4	0.5	0.7	0.9	1.1	1.5	1.9	2.2	2.8	3.6
1.8E+08	$(3.3 \pm 3.1) \times 10^{-3}$										
5.6E+08	$(2.0 \pm 0.9) \times 10^{-3}$										
1.8E+09	$(5.6 \pm 1.4) \times 10^{-3}$										
5.6E+09	$(3.9 \pm 0.5) \times 10^{-3}$	$(6.0 \pm 4.4) \times 10^{-4}$									
1.8E+10	$(2.3 \pm 0.2) \times 10^{-3}$	$(2.6 \pm 0.6) \times 10^{-3}$	$(1.8 \pm 1.8) \times 10^{-4}$				$(5.7 \pm 5.7) \times 10^{-7}$				
5.6E+10	$(1.1 \pm 0.1) \times 10^{-3}$	$(2.2 \pm 0.2) \times 10^{-3}$	$(2.4 \pm 0.4) \times 10^{-3}$	$(4.2 \pm 1.7) \times 10^{-3}$	$(5.3 \pm 2.4) \times 10^{-4}$						
1.8E+11	$(2.2 \pm 0.3) \times 10^{-4}$	$(7.1 \pm 0.4) \times 10^{-4}$	$(1.07 \pm 0.09) \times 10^{-3}$	$(1.9 \pm 0.2) \times 10^{-3}$	$(1.2 \pm 0.2) \times 10^{-3}$	$(1.8 \pm 0.5) \times 10^{-3}$	$(3.2 \pm 1.7) \times 10^{-4}$				
5.6E+11	$(1.2 \pm 0.5) \times 10^{-5}$	$(4.8 \pm 1.0) \times 10^{-5}$	$(1.5 \pm 0.1) \times 10^{-4}$	$(3.0 \pm 0.2) \times 10^{-4}$	$(5.7 \pm 0.6) \times 10^{-4}$	$(6.8 \pm 1.2) \times 10^{-4}$	$(6.1 \pm 0.9) \times 10^{-4}$	$(2.9 \pm 1.2) \times 10^{-4}$	$(2.2 \pm 0.9) \times 10^{-4}$		
1.8E+12	$(2.9 \pm 2.9) \times 10^{-6}$	$(5.1 \pm 3.6) \times 10^{-6}$	$(4.1 \pm 2.3) \times 10^{-6}$	$(1.7 \pm 0.4) \times 10^{-5}$	$(5.7 \pm 0.6) \times 10^{-5}$	$(1.02 \pm 0.09) \times 10^{-4}$	$(1.4 \pm 0.1) \times 10^{-4}$	$(2.7 \pm 0.8) \times 10^{-4}$	$(4.7 \pm 1.2) \times 10^{-4}$	$(6.8 \pm 4.2) \times 10^{-4}$	$(9.1 \pm 9.1) \times 10^{-6}$
5.6E+12				$(1.6 \pm 1.1) \times 10^{-6}$	$(1.8 \pm 1.0) \times 10^{-6}$	$(7.3 \pm 2.0) \times 10^{-6}$	$(1.2 \pm 0.2) \times 10^{-5}$	$(4.4 \pm 1.1) \times 10^{-5}$	$(5.4 \pm 1.3) \times 10^{-5}$	$(8.7 \pm 2.6) \times 10^{-5}$	$(3.0 \pm 1.6) \times 10^{-5}$
1.8E+13							$(3.8 \pm 2.7) \times 10^{-7}$	$(6.5 \pm 4.6) \times 10^{-7}$	$(1.7 \pm 0.6) \times 10^{-6}$	$(5.9 \pm 1.6) \times 10^{-6}$	$(2.5 \pm 0.9) \times 10^{-6}$

Table 2.10: Rest-frame total IR $1/V_{max}$ Luminosity Function in the PACS 160 μm band, assuming the CGBH cosmological model. Units are dex^{-1} Mpc^{-3}.

	Average redshift										
Luminosity [$L_\odot$]	0.2	0.4	0.5	0.7	0.9	1.1	1.5	1.9	2.2	2.8	3.6
1.8E+08	$(3.3 \pm 2.8) \times 10^{-3}$										
5.6E+08	$(1.7 \pm 0.8) \times 10^{-3}$										
1.8E+09	$(3.8 \pm 1.2) \times 10^{-3}$										
5.6E+09	$(5.0 \pm 1.1) \times 10^{-3}$	$(2.9 \pm 2.9) \times 10^{-4}$									
1.8E+10	$(2.3 \pm 0.2) \times 10^{-3}$	$(3.1 \pm 0.8) \times 10^{-3}$	$(4.7 \pm 2.4) \times 10^{-4}$								
5.6E+10	$(1.3 \pm 0.1) \times 10^{-3}$	$(1.7 \pm 0.2) \times 10^{-3}$	$(2.5 \pm 0.4) \times 10^{-3}$	$(2.3 \pm 0.4) \times 10^{-3}$	$(8.9 \pm 6.4) \times 10^{-5}$						
1.8E+11	$(2.4 \pm 0.3) \times 10^{-4}$	$(8.0 \pm 0.5) \times 10^{-4}$	$(9.8 \pm 1.2) \times 10^{-4}$	$(1.3 \pm 0.2) \times 10^{-3}$	$(9.4 \pm 1.9) \times 10^{-4}$	$(1.3 \pm 0.2) \times 10^{-3}$	$(3.6 \pm 1.3) \times 10^{-4}$				
5.6E+11	$(1.2 \pm 0.5) \times 10^{-5}$	$(5.1 \pm 1.1) \times 10^{-5}$	$(1.5 \pm 0.2) \times 10^{-4}$	$(3.3 \pm 0.2) \times 10^{-4}$	$(5.9 \pm 0.6) \times 10^{-4}$	$(7.6 \pm 1.1) \times 10^{-4}$	$(5.3 \pm 0.7) \times 10^{-4}$	$(2.4 \pm 0.7) \times 10^{-4}$	$(2.1 \pm 0.7) \times 10^{-4}$	$(1.9 \pm 1.9) \times 10^{-5}$	
1.8E+12	$(2.9 \pm 2.9) \times 10^{-6}$	$(5.8 \pm 4.1) \times 10^{-6}$	$(4.2 \pm 2.4) \times 10^{-6}$	$(1.8 \pm 0.4) \times 10^{-5}$	$(6.5 \pm 0.7) \times 10^{-5}$	$(1.12 \pm 0.09) \times 10^{-4}$	$(1.4 \pm 0.1) \times 10^{-4}$	$(1.5 \pm 0.4) \times 10^{-4}$	$(3.3 \pm 0.6) \times 10^{-4}$	$(1.8 \pm 0.5) \times 10^{-4}$	$(2.7 \pm 1.4) \times 10^{-5}$
5.6E+12				$(1.7 \pm 1.2) \times 10^{-6}$	$(1.9 \pm 1.1) \times 10^{-6}$	$(7.4 \pm 2.1) \times 10^{-6}$	$(1.4 \pm 0.2) \times 10^{-5}$	$(4.4 \pm 0.4) \times 10^{-5}$	$(4.1 \pm 0.4) \times 10^{-5}$	$(7.7 \pm 1.8) \times 10^{-5}$	$(2.9 \pm 1.0) \times 10^{-5}$
1.8E+13							$(4.0 \pm 2.8) \times 10^{-7}$	$(6.7 \pm 4.7) \times 10^{-7}$	$(1.7 \pm 0.6) \times 10^{-6}$	$(6.4 \pm 1.3) \times 10^{-6}$	$(1.5 \pm 0.4) \times 10^{-6}$

Table 2.11: Rest-frame total IR $1/V_{max}$ Luminosity Function in the PACS 100 μm band, assuming the OCGBH cosmological model. Units are dex^{-1} Mpc^{-3}.

	Average redshift										
Luminosity [$L_\odot$]	0.2	0.4	0.5	0.7	0.9	1.1	1.5	1.9	2.2	2.8	3.6
1.8E+08	$(4.7 \pm 3.9) \times 10^{-3}$										
5.6E+08	$(2.3 \pm 1.1) \times 10^{-3}$										
1.8E+09	$(6.7 \pm 1.7) \times 10^{-3}$										
5.6E+09	$(4.4 \pm 0.6) \times 10^{-3}$	$(7.1 \pm 5.3) \times 10^{-4}$									
1.8E+10	$(2.6 \pm 0.2) \times 10^{-3}$	$(3.5 \pm 0.8) \times 10^{-3}$	$(7.4 \pm 3.9) \times 10^{-4}$	$(9.2 \pm 9.2) \times 10^{-4}$			$(7.3 \pm 7.3) \times 10^{-7}$				
5.6E+10	$(1.2 \pm 0.2) \times 10^{-3}$	$(2.3 \pm 0.2) \times 10^{-3}$	$(2.6 \pm 0.4) \times 10^{-3}$	$(4.6 \pm 1.9) \times 10^{-3}$	$(7.3 \pm 3.1) \times 10^{-4}$	$(9.1 \pm 9.1) \times 10^{-5}$					
1.8E+11	$(1.9 \pm 0.3) \times 10^{-4}$	$(7.0 \pm 0.5) \times 10^{-4}$	$(1.2 \pm 0.1) \times 10^{-3}$	$(2.2 \pm 0.2) \times 10^{-3}$	$(1.5 \pm 0.2) \times 10^{-3}$	$(2.4 \pm 0.6) \times 10^{-3}$	$(4.9 \pm 2.3) \times 10^{-4}$				
5.6E+11	$(8.7 \pm 4.4) \times 10^{-6}$	$(4.7 \pm 1.1) \times 10^{-5}$	$(1.3 \pm 0.2) \times 10^{-4}$	$(2.9 \pm 0.2) \times 10^{-4}$	$(6.0 \pm 0.6) \times 10^{-4}$	$(6.5 \pm 1.1) \times 10^{-4}$	$(7.2 \pm 1.0) \times 10^{-4}$	$(4.1 \pm 1.5) \times 10^{-4}$	$(4.4 \pm 1.6) \times 10^{-4}$		
1.8E+12	$(3.4 \pm 3.4) \times 10^{-6}$	$(3.0 \pm 3.0) \times 10^{-6}$	$(3.3 \pm 2.3) \times 10^{-6}$	$(1.7 \pm 0.4) \times 10^{-5}$	$(4.7 \pm 0.6) \times 10^{-5}$	$(1.03 \pm 0.10) \times 10^{-4}$	$(1.5 \pm 0.1) \times 10^{-4}$	$(3.1 \pm 1.0) \times 10^{-4}$	$(4.5 \pm 1.0) \times 10^{-4}$	$(8.8 \pm 5.2) \times 10^{-4}$	$(1.9 \pm 1.4) \times 10^{-5}$
5.6E+12				$(9.4 \pm 9.4) \times 10^{-7}$	$(1.5 \pm 1.1) \times 10^{-6}$	$(2.1 \pm 1.2) \times 10^{-6}$	$(9.3 \pm 1.6) \times 10^{-6}$	$(4.4 \pm 1.4) \times 10^{-5}$	$(4.5 \pm 1.0) \times 10^{-5}$	$(6.6 \pm 2.1) \times 10^{-5}$	$(2.7 \pm 1.7) \times 10^{-5}$
1.8E+13							$(2.3 \pm 2.3) \times 10^{-7}$	$(8.1 \pm 5.7) \times 10^{-7}$	$(1.5 \pm 0.6) \times 10^{-6}$	$(5.1 \pm 1.7) \times 10^{-6}$	$(2.9 \pm 1.1) \times 10^{-6}$

Table 2.12: Rest-frame total IR $1/V_{max}$ Luminosity Function in the PACS 160 μm band, assuming the OCGBH cosmological model. Units are dex^{-1} Mpc^{-3}.

	Average redshift										
Luminosity [$L_\odot$]	0.2	0.4	0.5	0.7	0.9	1.1	1.5	1.9	2.2	2.8	3.6
1.8E+08	$(5.1 \pm 3.6) \times 10^{-3}$										
5.6E+08	$(6.2 \pm 3.0) \times 10^{-4}$										
1.8E+09	$(4.9 \pm 1.4) \times 10^{-3}$										
5.6E+09	$(5.8 \pm 1.3) \times 10^{-3}$	$(3.4 \pm 3.4) \times 10^{-4}$									
1.8E+10	$(2.8 \pm 0.3) \times 10^{-3}$	$(3.9 \pm 1.0) \times 10^{-3}$	$(6.7 \pm 3.1) \times 10^{-4}$	$(2.1 \pm 1.5) \times 10^{-4}$							
5.6E+10	$(1.3 \pm 0.2) \times 10^{-3}$	$(1.9 \pm 0.2) \times 10^{-3}$	$(3.1 \pm 0.5) \times 10^{-3}$	$(2.9 \pm 0.5) \times 10^{-3}$	$(1.1 \pm 0.8) \times 10^{-4}$	$(7.6 \pm 7.6) \times 10^{-5}$					
1.8E+11	$(2.1 \pm 0.3) \times 10^{-4}$	$(7.8 \pm 0.5) \times 10^{-4}$	$(1.0 \pm 0.1) \times 10^{-3}$	$(1.4 \pm 0.2) \times 10^{-3}$	$(1.3 \pm 0.2) \times 10^{-3}$	$(2.0 \pm 0.3) \times 10^{-3}$	$(5.4 \pm 1.8) \times 10^{-4}$				
5.6E+11	$(9.1 \pm 4.6) \times 10^{-6}$	$(5.1 \pm 1.2) \times 10^{-5}$	$(1.3 \pm 0.2) \times 10^{-4}$	$(3.1 \pm 0.2) \times 10^{-4}$	$(6.3 \pm 0.5) \times 10^{-4}$	$(6.4 \pm 0.9) \times 10^{-4}$	$(6.3 \pm 0.8) \times 10^{-4}$	$(3.4 \pm 1.0) \times 10^{-4}$	$(3.5 \pm 0.9) \times 10^{-4}$	$(4.8 \pm 3.4) \times 10^{-5}$	
1.8E+12	$(3.5 \pm 3.5) \times 10^{-6}$	$(3.0 \pm 3.0) \times 10^{-6}$	$(3.4 \pm 2.4) \times 10^{-6}$	$(1.8 \pm 0.4) \times 10^{-5}$	$(4.8 \pm 0.6) \times 10^{-5}$	$(1.14 \pm 0.10) \times 10^{-4}$	$(1.5 \pm 0.1) \times 10^{-4}$	$(1.7 \pm 0.3) \times 10^{-4}$	$(3.4 \pm 0.6) \times 10^{-4}$	$(2.3 \pm 0.6) \times 10^{-4}$	$(4.2 \pm 1.8) \times 10^{-5}$
5.6E+12				$(1.0 \pm 1.0) \times 10^{-6}$	$(1.7 \pm 1.2) \times 10^{-6}$	$(2.2 \pm 1.3) \times 10^{-6}$	$(1.0 \pm 0.2) \times 10^{-5}$	$(3.8 \pm 0.4) \times 10^{-5}$	$(4.1 \pm 0.4) \times 10^{-5}$	$(6.1 \pm 1.4) \times 10^{-5}$	$(2.4 \pm 1.0) \times 10^{-5}$
1.8E+13							$(2.5 \pm 2.5) \times 10^{-7}$	$(8.4 \pm 5.9) \times 10^{-7}$	$(1.5 \pm 0.6) \times 10^{-6}$	$(6.0 \pm 1.3) \times 10^{-6}$	$(1.8 \pm 0.5) \times 10^{-6}$

Table 2.13: Best-fitting Schechter parameters for the rest-frame 100 μm $1/V_{max}$ Luminosity functions.

	ΛCDM		CBGH		OCBGH	
$\bar{z}$	φ^*	L^*	φ^*	L^*	φ^*	L^*
0.2	$(2.2 \pm 0.2) \times 10^{-3}$	$(7.8 \pm 0.7) \times 10^{10}$	$(2.7 \pm 0.2) \times 10^{-3}$	$(5.2 \pm 0.4) \times 10^{10}$	$(3.0 \pm 0.3) \times 10^{-3}$	$(4.8 \pm 0.4) \times 10^{10}$
0.6	$(1.8 \pm 0.1) \times 10^{-3}$	$(1.81 \pm 0.09) \times 10^{11}$	$(2.2 \pm 0.1) \times 10^{-3}$	$(1.49 \pm 0.06) \times 10^{11}$	$(2.5 \pm 0.2) \times 10^{-3}$	$(1.36 \pm 0.06) \times 10^{11}$
1.0	$(1.02 \pm 0.09) \times 10^{-3}$	$(4.7 \pm 0.2) \times 10^{11}$	$(1.5 \pm 0.1) \times 10^{-3}$	$(3.7 \pm 0.2) \times 10^{11}$	$(1.5 \pm 0.1) \times 10^{-3}$	$(3.5 \pm 0.2) \times 10^{11}$
1.5	$(4.1 \pm 0.5) \times 10^{-4}$	$(9.9 \pm 0.7) \times 10^{11}$	$(3.5 \pm 0.4) \times 10^{-4}$	$(9.1 \pm 0.8) \times 10^{11}$	$(4.6 \pm 0.6) \times 10^{-4}$	$(7.4 \pm 0.7) \times 10^{11}$
2.1	$(4.8 \pm 1.4) \times 10^{-4}$	$(2.0 \pm 0.2) \times 10^{12}$	$(5.6 \pm 1.3) \times 10^{-4}$	$(1.6 \pm 0.2) \times 10^{12}$	$(5.6 \pm 1.2) \times 10^{-4}$	$(1.3 \pm 0.1) \times 10^{12}$
3.0	$(2.8 \pm 1.4) \times 10^{-4}$	$(2.0 \pm 0.4) \times 10^{12}$	$(1.5 \pm 0.5) \times 10^{-4}$	$(2.0 \pm 0.3) \times 10^{12}$	$(2.2 \pm 0.7) \times 10^{-4}$	$(1.9 \pm 0.3) \times 10^{12}$

Table 2.14: Best-fitting Schechter parameters for the rest-frame 160 μm $1/V_{max}$ Luminosity functions.

	ΛCDM		CBGH		OCBGH	
$\bar{z}$	φ^*	L^*	φ^*	L^*	φ^*	L^*
0.2	$(3.9 \pm 0.4) \times 10^{-3}$	$(3.1 \pm 0.3) \times 10^{10}$	$(2.4 \pm 0.2) \times 10^{-3}$	$(3.3 \pm 0.2) \times 10^{10}$	$(2.4 \pm 0.2) \times 10^{-3}$	$(3.0 \pm 0.1) \times 10^{10}$
0.6	$(2.3 \pm 0.2) \times 10^{-3}$	$(7.2 \pm 0.3) \times 10^{10}$	$(2.2 \pm 0.2) \times 10^{-3}$	$(6.9 \pm 0.3) \times 10^{10}$	$(2.5 \pm 0.2) \times 10^{-3}$	$(6.2 \pm 0.3) \times 10^{10}$
1.0	$(9.0 \pm 0.8) \times 10^{-4}$	$(2.0 \pm 0.1) \times 10^{11}$	$(1.12 \pm 0.10) \times 10^{-3}$	$(1.65 \pm 0.09) \times 10^{11}$	$(1.6 \pm 0.1) \times 10^{-3}$	$(1.35 \pm 0.06) \times 10^{11}$
1.5	$(3.9 \pm 0.5) \times 10^{-4}$	$(3.7 \pm 0.3) \times 10^{11}$	$(3.8 \pm 0.4) \times 10^{-4}$	$(3.4 \pm 0.2) \times 10^{11}$	$(3.5 \pm 0.5) \times 10^{-4}$	$(3.4 \pm 0.3) \times 10^{11}$
2.1	$(7.9 \pm 1.5) \times 10^{-5}$	$(1.5 \pm 0.2) \times 10^{12}$	$(2.1 \pm 0.3) \times 10^{-4}$	$(8.3 \pm 0.6) \times 10^{11}$	$(1.7 \pm 0.3) \times 10^{-4}$	$(7.7 \pm 0.8) \times 10^{11}$
3.0	$(3.8 \pm 1.2) \times 10^{-5}$	$(2.1 \pm 0.5) \times 10^{12}$	$(1.0 \pm 0.2) \times 10^{-4}$	$(7.9 \pm 1.1) \times 10^{11}$	$(9.3 \pm 2.3) \times 10^{-5}$	$(8.4 \pm 1.3) \times 10^{11}$

Table 2.15: Best-fitting Schechter parameters for the rest-frame total IR $1/V_{max}$ Luminosity functions in the PACS 100 μm band.

	ΛCDM		CBGH		OCBGH	
$\bar{z}$	φ^*	L^*	φ^*	L^*	φ^*	L^*
0.2	$(9.9 \pm 2.2) \times 10^{-4}$	$(1.6 \pm 0.3) \times 10^{11}$	$(1.3 \pm 0.2) \times 10^{-3}$	$(1.2 \pm 0.2) \times 10^{11}$	$(1.9 \pm 0.4) \times 10^{-3}$	$(8.7 \pm 1.4) \times 10^{10}$
0.4	$(1.6 \pm 0.2) \times 10^{-3}$	$(1.9 \pm 0.2) \times 10^{11}$	$(2.0 \pm 0.2) \times 10^{-3}$	$(1.7 \pm 0.1) \times 10^{11}$	$(2.3 \pm 0.2) \times 10^{-3}$	$(1.6 \pm 0.1) \times 10^{11}$
0.5	$(1.4 \pm 0.2) \times 10^{-3}$	$(2.9 \pm 0.3) \times 10^{11}$	$(1.8 \pm 0.2) \times 10^{-3}$	$(2.6 \pm 0.2) \times 10^{11}$	$(2.3 \pm 0.2) \times 10^{-3}$	$(2.2 \pm 0.2) \times 10^{11}$
0.7	$(1.9 \pm 0.3) \times 10^{-3}$	$(3.6 \pm 0.4) \times 10^{11}$	$(1.5 \pm 0.2) \times 10^{-3}$	$(4.0 \pm 0.4) \times 10^{11}$	$(3.7 \pm 0.5) \times 10^{-3}$	$(2.5 \pm 0.2) \times 10^{11}$
0.9	$(6.4 \pm 0.8) \times 10^{-4}$	$(8.7 \pm 0.7) \times 10^{11}$	$(1.0 \pm 0.1) \times 10^{-3}$	$(7.1 \pm 0.5) \times 10^{11}$	$(1.5 \pm 0.2) \times 10^{-3}$	$(5.7 \pm 0.4) \times 10^{11}$
1.1	$(4.8 \pm 1.0) \times 10^{-4}$	$(1.3 \pm 0.2) \times 10^{12}$	$(9.7 \pm 1.8) \times 10^{-4}$	$(9.1 \pm 1.1) \times 10^{11}$	$(1.3 \pm 0.2) \times 10^{-3}$	$(8.0 \pm 0.8) \times 10^{11}$
1.5	$(3.9 \pm 0.5) \times 10^{-4}$	$(2.0 \pm 0.1) \times 10^{12}$	$(4.0 \pm 0.5) \times 10^{-4}$	$(1.8 \pm 0.1) \times 10^{12}$	$(5.9 \pm 0.7) \times 10^{-4}$	$(1.5 \pm 0.1) \times 10^{12}$
1.9	$(9.2 \pm 2.1) \times 10^{-5}$	$(5.1 \pm 0.7) \times 10^{12}$	$(2.4 \pm 0.5) \times 10^{-4}$	$(3.5 \pm 0.4) \times 10^{12}$	$(3.2 \pm 0.8) \times 10^{-4}$	$(3.3 \pm 0.5) \times 10^{12}$
2.2	$(8.4 \pm 2.0) \times 10^{-5}$	$(5.9 \pm 0.7) \times 10^{12}$	$(1.7 \pm 0.4) \times 10^{-4}$	$(4.4 \pm 0.5) \times 10^{12}$	$(3.1 \pm 0.7) \times 10^{-4}$	$(3.5 \pm 0.4) \times 10^{12}$
2.8	$(2.2 \pm 0.8) \times 10^{-4}$	$(6.3 \pm 1.1) \times 10^{12}$	$(2.8 \pm 1.0) \times 10^{-4}$	$(5.2 \pm 0.9) \times 10^{12}$	$(2.0 \pm 0.8) \times 10^{-4}$	$(5.4 \pm 1.1) \times 10^{12}$
3.6	$(3.8 \pm 3.0) \times 10^{-6}$	$(2.4 \pm 1.5) \times 10^{13}$	$(5.0 \pm 5.9) \times 10^{-6}$	$(2.3 \pm 2.6) \times 10^{13}$	$(1.4 \pm 0.9) \times 10^{-5}$	$(1.2 \pm 0.7) \times 10^{13}$

Table 2.16: Best-fitting Schechter parameters for the rest-frame total IR $1/V_{max}$ Luminosity functions in the PACS 160 μm band.

	ΛCDM		CBGH		OCBGH	
$\bar{z}$	φ^*	L^*	φ^*	L^*	φ^*	L^*
0.2	$(1.1 \pm 0.2) \times 10^{-3}$	$(1.6 \pm 0.3) \times 10^{11}$	$(1.8 \pm 0.3) \times 10^{-3}$	$(1.0 \pm 0.2) \times 10^{11}$	$(2.5 \pm 0.5) \times 10^{-3}$	$(7.9 \pm 1.2) \times 10^{10}$
0.4	$(1.6 \pm 0.2) \times 10^{-3}$	$(2.0 \pm 0.2) \times 10^{11}$	$(2.0 \pm 0.2) \times 10^{-3}$	$(1.8 \pm 0.1) \times 10^{11}$	$(2.3 \pm 0.2) \times 10^{-3}$	$(1.6 \pm 0.1) \times 10^{11}$
0.5	$(1.3 \pm 0.2) \times 10^{-3}$	$(2.9 \pm 0.3) \times 10^{11}$	$(2.0 \pm 0.2) \times 10^{-3}$	$(2.4 \pm 0.2) \times 10^{11}$	$(2.6 \pm 0.3) \times 10^{-3}$	$(2.1 \pm 0.1) \times 10^{11}$
0.7	$(9.8 \pm 1.2) \times 10^{-4}$	$(5.1 \pm 0.5) \times 10^{11}$	$(1.3 \pm 0.1) \times 10^{-3}$	$(4.4 \pm 0.3) \times 10^{11}$	$(1.5 \pm 0.2) \times 10^{-3}$	$(4.0 \pm 0.4) \times 10^{11}$
0.9	$(5.1 \pm 0.6) \times 10^{-4}$	$(1.01 \pm 0.09) \times 10^{12}$	$(1.1 \pm 0.1) \times 10^{-3}$	$(7.0 \pm 0.5) \times 10^{11}$	$(1.7 \pm 0.2) \times 10^{-3}$	$(5.5 \pm 0.3) \times 10^{11}$
1.1	$(5.0 \pm 0.8) \times 10^{-4}$	$(1.3 \pm 0.1) \times 10^{12}$	$(1.1 \pm 0.1) \times 10^{-3}$	$(8.6 \pm 0.7) \times 10^{11}$	$(1.4 \pm 0.2) \times 10^{-3}$	$(7.7 \pm 0.6) \times 10^{11}$
1.5	$(3.2 \pm 0.3) \times 10^{-4}$	$(2.2 \pm 0.1) \times 10^{12}$	$(4.2 \pm 0.4) \times 10^{-4}$	$(1.8 \pm 0.1) \times 10^{12}$	$(5.6 \pm 0.6) \times 10^{-4}$	$(1.5 \pm 0.1) \times 10^{12}$
1.9	$(7.8 \pm 1.1) \times 10^{-5}$	$(5.7 \pm 0.6) \times 10^{12}$	$(2.2 \pm 0.3) \times 10^{-4}$	$(3.6 \pm 0.3) \times 10^{12}$	$(2.6 \pm 0.4) \times 10^{-4}$	$(3.2 \pm 0.4) \times 10^{12}$
2.2	$(9.6 \pm 1.6) \times 10^{-5}$	$(5.6 \pm 0.6) \times 10^{12}$	$(1.9 \pm 0.3) \times 10^{-4}$	$(4.0 \pm 0.4) \times 10^{12}$	$(3.1 \pm 0.5) \times 10^{-4}$	$(3.1 \pm 0.4) \times 10^{12}$
2.8	$(8.1 \pm 2.4) \times 10^{-5}$	$(9.0 \pm 1.5) \times 10^{12}$	$(1.9 \pm 0.4) \times 10^{-4}$	$(5.8 \pm 0.6) \times 10^{12}$	$(1.9 \pm 0.4) \times 10^{-4}$	$(5.5 \pm 0.6) \times 10^{12}$
3.6	$(1.4 \pm 0.6) \times 10^{-5}$	$(1.0 \pm 0.3) \times 10^{13}$	$(3.3 \pm 1.2) \times 10^{-5}$	$(6.4 \pm 1.2) \times 10^{12}$	$(4.9 \pm 1.6) \times 10^{-5}$	$(5.8 \pm 0.9) \times 10^{12}$

Table 2.17: Faint-end slope values

dataset	ΛCDM	CGBH	OCGBH
$L_{100\mu m}$	0.42 ± 0.04	0.03 ± 0.05	0.03 ± 0.05
$L_{160\mu m}$	0.25 ± 0.06	0.00 ± 0.05	0.00 ± 0.05
$L_{IR,100\mu m}$	0.67 ± 0.06	0.38 ± 0.08	0.33 ± 0.09
$L_{IR,160\mu m}$	0.61 ± 0.07	0.26 ± 0.09	0.2 ± 0.1

Table 2.18: Comoving number density and characteristic luminosity evolution parameters.

dataset	model	A	B
$L_{100\mu m}$	ΛCDM	$(5.2 \pm 1.0) \times 10^{-1}$	$(-3.3 \pm 0.6) \times 10^{-1}$
	CGBH	$(5.6 \pm 1.0) \times 10^{-1}$	$(-4.5 \pm 0.8) \times 10^{-1}$
	OCGBH	$(5.5 \pm 0.9) \times 10^{-1}$	$(-4.2 \pm 0.7) \times 10^{-1}$
$L_{160\mu m}$	ΛCDM	$(6.8 \pm 0.8) \times 10^{-1}$	$(-7.6 \pm 0.6) \times 10^{-1}$
	CGBH	$(5.4 \pm 0.9) \times 10^{-1}$	$(-5.8 \pm 0.8) \times 10^{-1}$
	OCGBH	$(5.4 \pm 0.9) \times 10^{-1}$	$(-5.8 \pm 0.8) \times 10^{-1}$
$L_{IR,100\mu m}$	ΛCDM	$(6.4 \pm 0.5) \times 10^{-1}$	$(-6.6 \pm 1.0) \times 10^{-1}$
	CGBH	$(6.4 \pm 0.4) \times 10^{-1}$	$(-6.3 \pm 0.9) \times 10^{-1}$
	OCGBH	$(6.3 \pm 0.5) \times 10^{-1}$	$(-6.1 \pm 0.7) \times 10^{-1}$
$L_{IR,160\mu m}$	ΛCDM	$(5.8 \pm 0.7) \times 10^{-1}$	$(-5.9 \pm 0.5) \times 10^{-1}$
	CGBH	$(5.6 \pm 0.7) \times 10^{-1}$	$(-5.1 \pm 0.3) \times 10^{-1}$
	OCGBH	$(5.6 \pm 0.7) \times 10^{-1}$	$(-5.1 \pm 0.3) \times 10^{-1}$

2.5 Standard vs. void models comparison

In Fig. 2.1-2.4 we plot the $1/V_{max}$ LF estimations in the three different cosmologies, together with the best-fit Schechter profiles for each of them. As can be seen in the four figures, the faint-end number densities in the void models are lower then the standard model ones.

If there were a direct correlation between the matter density parameter in the cosmology, and its estimated number density of sources selected in the FIR, then at the lowest redshift bin we should see higher number densities in the void models, since the $\Omega_M(z)$ in those models are bigger in that redshift range than the standard model value (more on that in Appendix A, Fig. A.1).

The difference in the number densities at the lower redshift interval for the different cosmologies does not follow the same relation as the matter density parameters $\Omega_M(z)$. In addition, it shows a dependence on the luminosity, which is more pronounced at the fainter end in both the monochromatic and the total IR LFs.

This dependence produces significant differences in the faint-end slopes of the computed luminosity functions. This can only be attributed to the different geo-

metrical parts of the cosmological models studied here, since the matter content, as discussed above, would only shift the normalization of the LF independently of the luminosity of the sources.

In Table 2.17 we present the best fit values of α for each dataset / model combination. Simple error propagation allow us to write the uncertainty of the difference $\Delta\alpha$ between the faint-end slopes in the standard model (α_Λ) and the void models (α_V) as

$$\delta(\Delta\alpha) = \sqrt{(\delta\alpha_\Lambda)^2 + (\delta\alpha_V)^2}. \tag{2.14}$$

The significance level of this difference can then be obtained by computing $\Delta\alpha/\delta(\Delta\alpha)$. For the monochromatic 100 μm luminosity functions, the difference between the α computed assuming the standard model and the α computed in the GBH models studied here is 6.1-σ, as compared to its propagated uncertainty. For the monochromatic 160 μm luminosity functions, this value is 3.2-σ. For the total-IR 100-μ selected luminosity functions, these values are 2.9-σ for the difference between ΛCDM and CGBH models, and 3.1-σ, for the ΛCDM-OCGBH difference. Finally, for the same differences in the total-IR 160 μm selected dataset, the significances are 3.1-σ and 3.4-σ, respectively.

Could this difference be caused by a limitation of the $1/V_{max}$ method used here? As we show in Appendix A, the matter density parameters in both the ΛCDM and GBH models do not affect the performance of this LF estimator significantly. When the same input LF and matter density are assumed, the $1/\mathrm{V}_{max}$ method obtains values within their error bars for all cosmological models considered. This indicates that the change in the slopes is caused by how the luminosities are computed from the redshifts in the different metrics.

To check this assertion, we investigate the effects of both luminosity and comoving volume separately on the shape of the LF. Starting from the $1/V_{max}$ results for the LF in the interval $0 < z < 0.4$, assuming the standard cosmological model, we compute alternative LFs using the same methodology, but assuming either the luminosity distance of one of the void models and keeping the comoving distance of the standard model, or the luminosity distance of the standard model and the comoving distance of one of the void models. This allows us to assess how each distance definition affect the LF individually. The results are plotted in Fig. 2.6 for the rest-frame 100 μm monochromatic luminosity dataset.

From these plots it is clear that the luminosity is the main cause of change in the shape of the LF. What remains to be investigated is whether the number density in a given luminosity bin is lower in the void models because of a re-arranging of the number counts in the luminosity bins, or because of a possible change in the maximum volume estimate of the sources in each bin. From this inspection, it

turns out that the number counts in all three models are all within their Poisson errors, and therefore the number densities in the void models are lower because the maximum volumes in them are larger.

Looking at Eq. (2.10), we identify two parameters that can introduce a dependency of the maximum volume of a source on its luminosity, the incompleteness corrections $w_k(z)$ and the upper limit of the integral z_{max}.

The incompleteness correction $w_k(z)$ for each source depends on the observed flux that the source would have at that redshift, which is affected by the luminosity distance-redshift relation assumed.

More importantly however, at the higher luminosity bins, the z_{max} of most of the sources there assumes the z_h value for that redshift interval, which does not depend on the luminosity of the source. This renders the V_{max} of the high luminosity sources approximately the same, apart from small changes caused by the incompleteness corrections w_k, as discussed above. At the lower luminosity bins, on the other hand, it happens more often that the z_{max} of a source assumes its ζ value, which in this case depends on its luminosity, as is clear from Eq. (2.8).

In order for that equation to hold, given that f_R and $f_{R,lim}$ are fixed, the $d_L(z)/d_L(\zeta)$ ratio must be the same for all cosmologies. Since the redshift z of each source is also fixed, then it follows that the ζ value that makes the $d_L(z)/d_L(\zeta)$ ratio hold in the void models must be higher then in the standard model (see Fig. 1.3). This, in turn, accounts for the larger maximum volumes and lower number densities at the low luminosity bins in the void models.

From the discussion above we conclude that a change in the luminosity distance - redshift relation changes the z_{max} of the low luminosity sources, which in turn changes the maximum volumes, and finally, the fitted faint-end slope. However, from Fig. 1.3, it is not obvious that such small differences in the $d_L(z)$ relation for the different cosmological models could cause such a significant change in the faint-end slopes, especially at low redshifts. It is useful to remember here that the LF is a non-linear combination of quantities that depend, from a geometrical point of view, on the luminosity distance (through the luminosities of the sources) and on the comoving distances (through their enclosing volumes). Even if the observational constraints on the luminosity-redshift relation, and the additional ones stemming from BAO results, yield both $d_L(z)$ and $r(z)$ that are quite robust under changes of the underlying cosmological models, such small differences in the distances could pile up non-linearly and cause the observed discrepancies in the faint-end slope.

This appears to be the case here, at least in the low redshift interval where we can fit the faint-end slopes with confidence. Rather then following the trend of the matter density parameter, the number densities at those redshifts seem to be predominantly determined by their enclosing volumes, even if at low redshift

the differences in the distance-redshift relations in the different cosmologies is quite small.

Looking at how the distances in Fig. 1.3 have increasingly different values at higher redshifts, it would be interesting to check if the faint-end slopes in the different cosmologies at some point start following that trend. Unfortunately, at higher redshifts the incompleteness caused by different luminosity limits for different populations does not allow us to draw any meaningful conclusion about the faint-end slope of the derived LFs. As it is, all that can be concluded is that the standard model LF would be over-estimating the local density of lower luminosity galaxies if the Universe's expansion rate and history followed that of the LTB/GBH models.

We proceed to investigate the robustness with respect to the underlying cosmology of the redshift evolution of the other two Schechter parameters, the characteristic luminosity L^* and number density ϕ^*. Figure 2.5 presents the redshift evolution of these parameters that we model by means of the simple relations

$$L^*(z) \propto 10^{(1+z)A} \tag{2.15}$$

$$\phi^*(z) \propto 10^{(1+z)B}. \tag{2.16}$$

We use a least-squares technique to fit such evolution functions to their corresponding Schechter parameter results (Richter 1995). Table 2.18 lists the best-fit values for the evolution parameters A and B in the different datasets / cosmologies.

The listed uncertainties for the evolution parameters are the formal 1-σ values obtained from the square root of the corresponding diagonal element of the covariance matrix of the fit. We find no evidence of a significantly different evolution of either L^* or ϕ^* in the void models considered. The monochromatic luminosities, especially the number density of sources in the rest-frame 160 μm, show some mild evidence of being affected by the geometrical effect discussed above, but the evolution parameters in the total IR are remarkably similar. We also note that assuming an open or flat CGBH model makes no significant difference to such parameters. It seems that they are more strongly affected by the intrinsic evolution of the sources, and the secular processes and merging history of galaxy formation than by the expansion rate of the Universe.

Physically speaking, in terms of tracing the redshift evolution of different galaxy populations using the FIR data in the present work, the marginally significant difference in the faint-end slopes, together with the evolution parameters for the characteristic number densities and luminosities, can be understood as follows: assertions about the number density of FIR low-luminosity galaxies, broadly related to populations that are poor in dust content, are still systematically affected by model-dependent corrections due to survey flux limits in the construction of the LF. That

is, there might be less of these galaxies in the local Universe ($z \approx 0.3$) than what we expect based on the underlying standard model. On the other hand, evolution of the FIR high-luminosity end, broadly related to populations with high dust content, is well constrained by the flux limits of the PEP survey where the underlying cosmological model is concerned.

Chapter 3

Comoving densities

Having computed the LF in both cosmologies studied here, we focus our attention next to computing and studying the observed number density we can derive from it.

3.1 Selection functions

Selection functions are an estimate of the number density of galaxies with luminosity above a chosen threshold, L_{lim}. Once computed, the selection functions can be used to estimate the observed number of objects per comoving volume, derived in Sect. 1.2.3, and from that the observed differential and integral densities in the past lightcone.

Following the empirical approach of Iribarrem et al. (2012), we computed selection functions ψ in each redshift interval using each of the three cosmological models (ΛCDM, CGBH, and OCGBH) and the monochromatic 100 μm and 160 μm rest-frame luminosity functions for the combined PEP fields in Iribarrem et al. (2013b) as

$$\psi_{\bar{z}} = \int_{L_{lim,\,\bar{z}}}^{L_{max,\,\bar{z}}} \phi_{\bar{z}}(L)\, dL\,, \tag{3.1}$$

where $L_{max,\,\bar{z}}$ is the brightest source luminosity inside the redshift interval, and $L_{lim,\,\bar{z}}$ is the rest-frame luminosity associated to the flux limit of the observations.

The dataset used in this work was built using combined fields, i.e observations carried out in different sky regions at different depth. The large number of sources per redshift interval allowed us to derive the observed quantities with a better statistics, at the expense of an added difficulty related to the definition of the luminosity limits corresponding to the actual flux limits of the observations. This difficulty stems from the fact that the computation of the rest-frame luminosity involves k corrections, which in turn depends on the spectral energy distribution (SED) of the source. That is, each SED template defines a slightly different luminosity limit for the same flux limit. In the case of the PEP survey, each field – namely GOODS-N,

GOODS-S, COSMOS and ECDF-S – had also a different flux limit, depending on the PACS passband in which the observation was done (Lutz et al. 2011).

To investigate how important are the selection function variations caused by the different SED templates in the datasets, we first computed the selection functions in each redshift interval assuming the lowest computed luminosity among the sources in that interval, and then compared the results to the average, and to the highest luminosities. The variations in the selection functions caused by assuming different luminosity limits were found to be many times larger then the error bars propagated from the luminosity function uncertainties. For example, at $z = 0.2$, the selection function computed using the lowest monochromatic luminosity in the 100-μm dataset read $(9.0 \pm 1.8) \times 10^{-3}$ Mpc^{-3}, while the one computed using the average luminosity read $(3.7 \pm 0.7) \times 10^{-3}$ Mpc^{-3}, and the one using the highest luminosity read $(2.6 \pm 0.5) \times 10^{-3}$ Mpc^{-3}, a variation over three times larger then the combined uncertainties obtained by propagating the ones from the LF parameters. For the same dataset, at $z = 1$, the selection functions read $(2.3 \pm 0.3) \times 10^{-3}$ Mpc^{-3}, $(1.1 \pm 0.1) \times 10^{-3}$ Mpc^{-3}, and $(4.9 \pm 0.6) \times 10^{-4}$ Mpc^{-3}, respectively, a variation almost six times larger then the propagated uncertainties.

Therefore, for every source in each redshift interval, we computed the rest-frame luminosity for the flux limit of the field and filter where it was observed, given its best fit SED and redshift. Next, we computed a set of selection function values in that redshift interval, using the luminosity limits computed above for each source in the interval. Finally, we computed the average over this set of selection function values for a given redshift interval and used this average as the value for the selection function in that same interval. The uncertainties, as discussed above, are dominated by the variation in the luminosity limits, and therefore can be taken simply as the standard deviation over the same set of computed selection function values for each redshift interval. The resulting monochromatic rest-frame 100 μm and 160 μm selection functions are given in tables 3.1 and 3.2.

3.2 Consistency functions

In the empirical framework of Ribeiro & Stoeger (2003); Albani et al. (2007); Iribarrem et al. (2012), the observed quantities computed in the past lightcone of a given cosmological model were obtained from their predicted values through what it was then called a completeness function $J(z)$. This can be somewhat confusing from the observer's point of view, since $J(z)$ is not necessarily related to incompleteness like that of missing sources in a survey, but to the relation between a theoretical prediction for the number counts and the actual measurement of that quantity (Iribarrem et al. 2012). In this sense, this quantity would be better named *consistency*

Table 3.1: Selection functions for the rest-frame 100 μm datasets. Units are Mpc^{-3}.

$\bar{z}$	$\psi^{\Lambda CDM}$	ψ^{CGBH}	ψ^{OCGBH}
0.1	$(4.0 \pm 0.8) \times 10^{-3}$	$(5.0 \pm 1.0) \times 10^{-3}$	$(5.6 \pm 1.1) \times 10^{-3}$
0.3	$(3.6 \pm 0.5) \times 10^{-3}$	$(4.4 \pm 0.6) \times 10^{-3}$	$(5.0 \pm 0.7) \times 10^{-3}$
0.5	$(2.6 \pm 0.4) \times 10^{-3}$	$(3.2 \pm 0.5) \times 10^{-3}$	$(3.6 \pm 0.5) \times 10^{-3}$
0.7	$(2.3 \pm 0.4) \times 10^{-3}$	$(2.9 \pm 0.5) \times 10^{-3}$	$(3.2 \pm 0.6) \times 10^{-3}$
0.9	$(1.3 \pm 0.2) \times 10^{-3}$	$(1.9 \pm 0.3) \times 10^{-3}$	$(1.9 \pm 0.3) \times 10^{-3}$
1.1	$(1.1 \pm 0.3) \times 10^{-3}$	$(1.6 \pm 0.4) \times 10^{-3}$	$(1.6 \pm 0.4) \times 10^{-3}$
1.4	$(4.3 \pm 1.1) \times 10^{-4}$	$(3.7 \pm 1.0) \times 10^{-4}$	$(4.8 \pm 1.2) \times 10^{-4}$
1.6	$(4.1 \pm 1.4) \times 10^{-4}$	$(3.6 \pm 1.2) \times 10^{-4}$	$(4.6 \pm 1.5) \times 10^{-4}$
2.0	$(5.1 \pm 1.6) \times 10^{-4}$	$(5.9 \pm 1.9) \times 10^{-4}$	$(6.0 \pm 1.9) \times 10^{-4}$
2.4	$(4.9 \pm 1.7) \times 10^{-4}$	$(5.6 \pm 2.0) \times 10^{-4}$	$(5.7 \pm 2.0) \times 10^{-4}$
2.8	$(3.3 \pm 1.1) \times 10^{-4}$	$(1.7 \pm 0.5) \times 10^{-4}$	$(2.5 \pm 0.8) \times 10^{-4}$
3.2	$(2.7 \pm 1.1) \times 10^{-4}$	$(1.4 \pm 0.6) \times 10^{-4}$	$(2.1 \pm 0.8) \times 10^{-4}$

Table 3.2: Selection functions for the rest-frame 160 μm datasets. Units are Mpc^{-3}.

$\bar{z}$	$\psi^{\Lambda CDM}$	ψ^{CGBH}	ψ^{OCGBH}
0.1	$(6.0 \pm 1.4) \times 10^{-3}$	$(3.7 \pm 0.9) \times 10^{-3}$	$(3.7 \pm 0.9) \times 10^{-3}$
0.3	$(5.4 \pm 0.9) \times 10^{-3}$	$(3.3 \pm 0.5) \times 10^{-3}$	$(3.3 \pm 0.5) \times 10^{-3}$
0.5	$(2.7 \pm 0.5) \times 10^{-3}$	$(2.6 \pm 0.4) \times 10^{-3}$	$(3.0 \pm 0.5) \times 10^{-3}$
0.7	$(2.5 \pm 0.5) \times 10^{-3}$	$(2.3 \pm 0.5) \times 10^{-3}$	$(2.7 \pm 0.6) \times 10^{-3}$
0.9	$(1.0 \pm 0.2) \times 10^{-3}$	$(1.3 \pm 0.2) \times 10^{-3}$	$(1.8 \pm 0.3) \times 10^{-3}$
1.1	$(9.8 \pm 2.7) \times 10^{-4}$	$(1.2 \pm 0.3) \times 10^{-3}$	$(1.8 \pm 0.4) \times 10^{-3}$
1.4	$(4.6 \pm 1.2) \times 10^{-4}$	$(4.4 \pm 1.2) \times 10^{-4}$	$(4.2 \pm 1.1) \times 10^{-4}$
1.6	$(4.5 \pm 1.3) \times 10^{-4}$	$(4.3 \pm 1.3) \times 10^{-4}$	$(4.1 \pm 1.2) \times 10^{-4}$
2.0	$(1.1 \pm 0.3) \times 10^{-4}$	$(3.0 \pm 0.8) \times 10^{-4}$	$(2.4 \pm 0.7) \times 10^{-4}$
2.4	$(1.3 \pm 0.3) \times 10^{-4}$	$(3.4 \pm 0.9) \times 10^{-4}$	$(2.8 \pm 0.8) \times 10^{-4}$
2.8	$(5.9 \pm 1.9) \times 10^{-5}$	$(1.5 \pm 0.4) \times 10^{-4}$	$(1.4 \pm 0.4) \times 10^{-4}$
3.2	$(3.5 \pm 1.6) \times 10^{-5}$	$(9.2 \pm 4.3) \times 10^{-5}$	$(8.6 \pm 4.0) \times 10^{-5}$

function, a term which we will use from now on. The consistency function $J(z)$ was obtained by relating the prediction for the comoving number density n_C given by the cosmological model

$$n_C(z) = \frac{\rho_M[r(z)]}{\mathcal{M}_g} = \frac{\Omega_M[r(z)]}{\mathcal{M}_g}\,\rho_C, \tag{3.2}$$

to the selection functions for a given galaxy survey $\psi_{\bar{z}}$ in a given redshift interval $\bar{z}$ as Iribarrem et al. (2012),

$$J_{\bar{z}} = \frac{\psi_{\bar{z}}}{n_C(\bar{z})}. \tag{3.3}$$

The values for $J_{\bar{z}}$ can be obtained numerically for the CGBH void models using Eqs. (1.57), and (1.61) combined with the appropriate $r(z)$ table as described in §1.1, and the selection functions computed in §3.1.

As discussed in Iribarrem et al. (2012) the estimation of the comoving number density n_C assumes a constant, average total mass value $\mathcal{M}_g$ for normalisation purpose – that is, getting a correct order-of-magnitude estimation of the number density. Such estimation is not supposed to provide a detailed description of $n_C(z)$, but rather to convey the information on the redshift evolution of the comoving number density caused solely by the cosmological model, through $\rho_M(z)$, on Eq. (3.2). The details of the redshift evolution of the total masses of the sources, missing on this estimation, are imprinted on the observed LF, and inherited by its derived selection functions. By translating this purely theoretical $n_C(\bar{z})$ estimation to the corresponding selection functions $\psi_{\bar{z}}$ through the consistency function $J(\bar{z})$, we allow any theoretical quantity assuming a $n_C(z)$ built on a cosmological model to use the observed values given by the selection functions.

For the purpose of obtaining empirically the relativistic number densities this approach is sufficient. It minimizes the number of theoretical assumptions about the evolution of the sources, such as including a Press & Schechter (1974) formalism, and considers as much information as possible from the observations. Since a Press-Schechter-like formalism is still not implemented on LTB models, the empirical approach described above is the simplest way to work with both standard and void cosmologies in a consistent way.

As mentioned above, Mustapha et al. (1997) showed that any spherically symmetric observation alone, e.g. redshift estimations or number counts, can be fit purely by a general enough LTB dust model, no evolution of the sources required.

In the context of the present discussion their argument can be understood by combining Eqs. (3.2) and (3.3) to write

$$J_{\bar{z}} \;=\; \psi_{\bar{z}}\,\frac{\mathcal{M}_g}{\rho_C\,\Omega_M(\bar{z})} \tag{3.4}$$

Looking at the right-hand side of the equation above one can easily separate its two terms into an observed quantity to the left and a fraction between theoretically obtained quantities to the right. Moreover, one can identify the constant $\mathcal{M}_g$ with the lack of a model for the secular evolution of the average mass of the sources, and $\Omega_{_M}(\bar{z})$ with the evolution of the matter density parameter on a given cosmology. By using the extra degree of freedom in setting the matter density profile in the LTB model, $\Omega_{_M}(z)$, one can obtain a number density $n_{_C}(z)$ that perfectly matches the selection functions without the need to assume an evolving average mass $\mathcal{M}_g(z)$. To constrain this degree of freedom, it is necessary a different set of independent observations. This is precisely what the GBH parametrisation of a giant void in an LTB dust model yields: a matter density profile that is parameterized to best fit the combination of different, independent observations.

We present the evolution of the consistency functions for the different PACS filters and cosmological models in figures 3.1 and 3.2. It is clear from these plots that this quantity evolves with redshift in both standard and void cosmologies. The behaviour of the consistency functions in all models studied here are well fit by a power-law decreasing with redshift. The best fitting slopes are given in table 3.3. These results suggest that not considering the evolution of the sources leads to a systematic trend that increases the inconsistency with z. This is not as obvious as it may seem given the flexibility of the LTB models as discussed above. It is the parametrisation of $\Omega_{_M}(z)$ constrained by combined independent observations that requires $\mathcal{M}_g$ to evolve with z in the LTB models studied here. Only by allowing $\mathcal{M}_g$ to evolve with z can Eq. (3.4) yield a constant consistency function indicating that the theoretical term on the right of the right-hand side of Eq. (3.4) is proportional to the observed term on the left.

We use a Kolmogorov-Smirnoff (KS) two-sample test to check, on a statistical sense, how different are the consistency functions assuming the different cosmological models studied here from a hypothetically constant consistency function. By construction, a constant $J(z)$ indicates that the model for the comoving number density used here, assuming $\mathcal{M}_g(z) = \mathcal{M}_g$, matches the observed number density. The KS test is a non-parametric, distribution-free way to compare two datasets, and assigns to which level of confidence can we refute the hypothesis that they were obtained from the same underlying distribution. The resulting p-value of this test can be understood as the probability that both datasets come from the same distribution. For all cosmologies studied here, the no-evolution hypothesis, $\mathcal{M}_g(z) = \mathcal{M}_g$, is rejected at over 5-$\sigma$ confidence level, with p-values lower then 10^{-5}. This means that an evolving average mass of the sources is also required by the LTB/GBH models studied here.

Next, we use the same KS test to determine how different the consistency func-

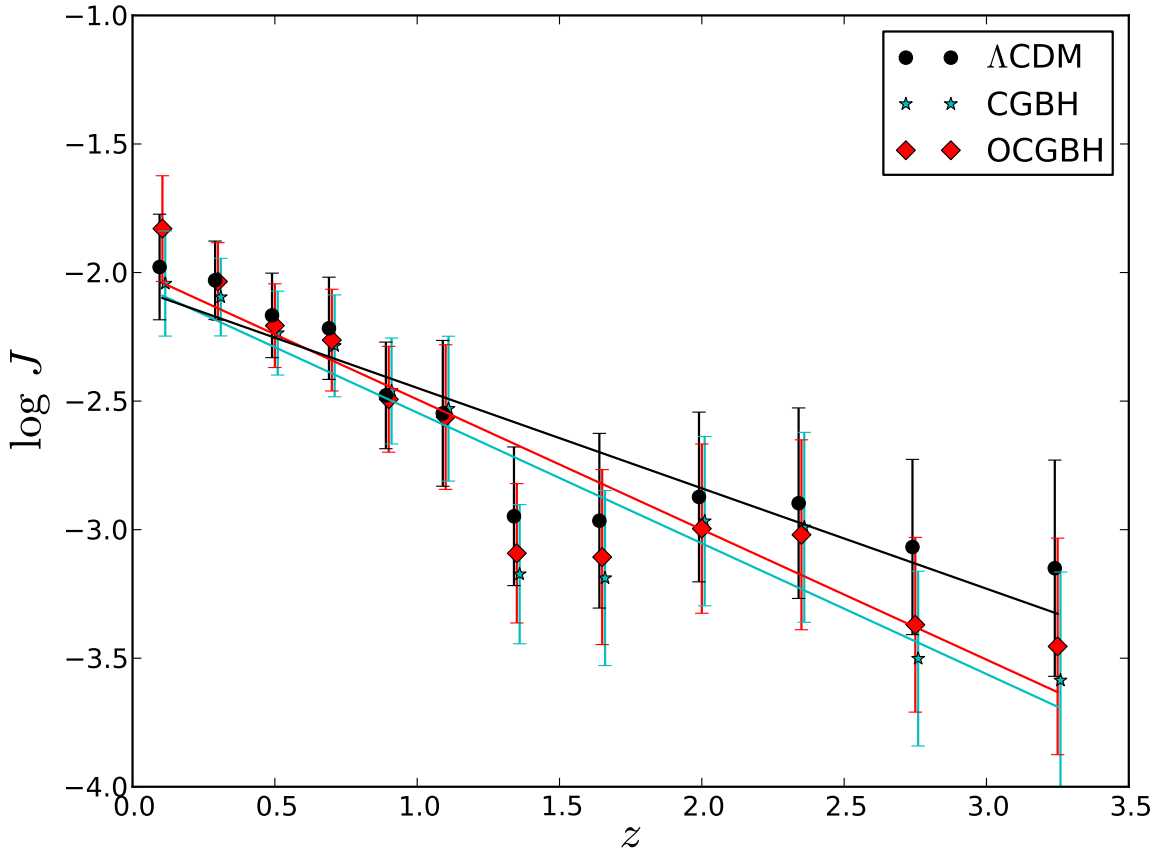

Figure 3.1: Consistency functions for the monochromatic 100 μm luminosity functions computed in the three cosmological models used in the present work.

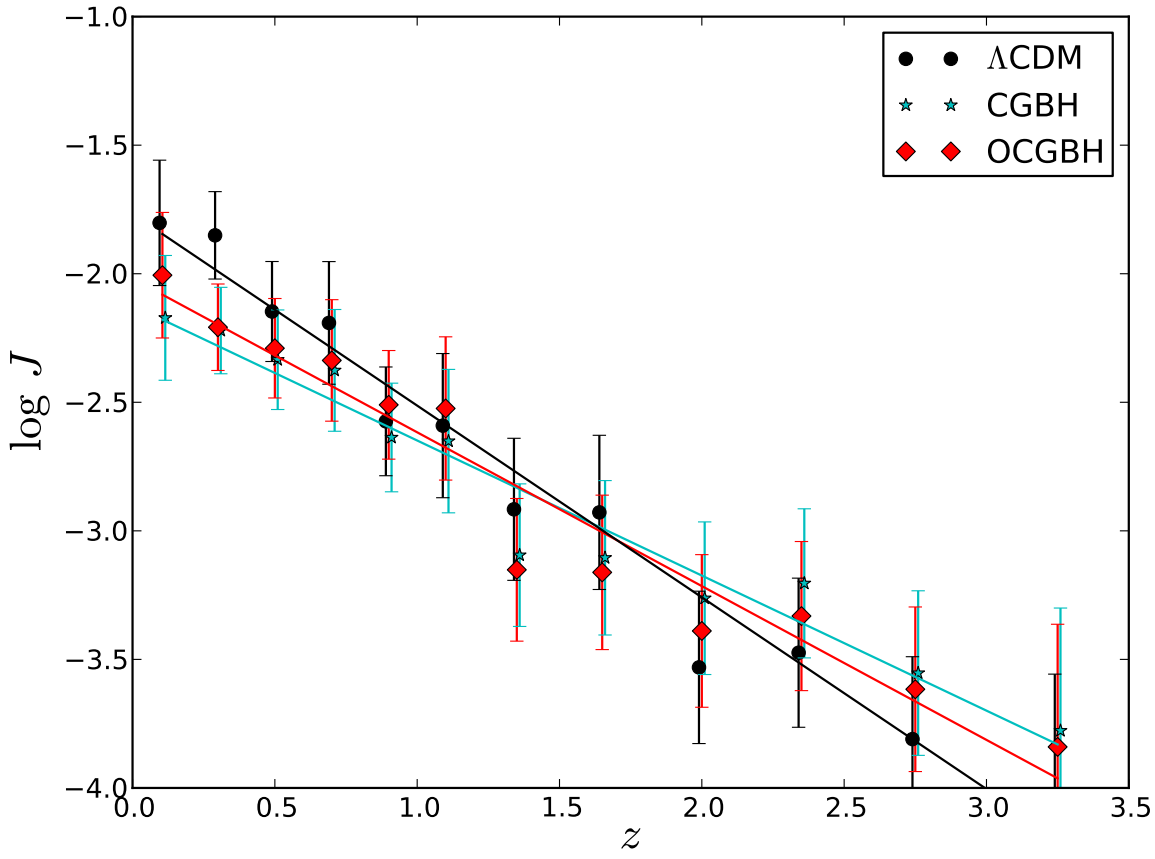

Figure 3.2: The same results as in Figure 3.1 for the monochromatic 160 μm luminosity functions. From these plots, one can see that the difference between the standard model consistency function (black circles), and the void model ones (color circles) is not very significant, since most of the points lie within the error bars. The p_Λ values discussed in §3.1 quantify this conclusion, and agree with it.

Table 3.3: Comoving, differential and integral densities statistics.

dataset	model	p_Λ	$\log J(z)$ slope	$\log \gamma_L$ slope	$\log \gamma_L^*$ slope
$L_{100\,\mu m}$	ΛCDM	1.0	-0.39 ± 0.05	-2.4 ± 0.2	-2.31 ± 0.03
	CGBH	0.43	-0.51 ± 0.06	-3.1 ± 0.6	-2.50 ± 0.04
	OCGBH	0.43	-0.51 ± 0.05	-3.0 ± 0.4	-2.52 ± 0.03
$L_{160\,\mu m}$	ΛCDM	1.0	-0.75 ± 0.03	-4.5 ± 0.3	-2.54 ± 0.06
	CGBH	0.79	-0.53 ± 0.03	-3.7 ± 0.4	-2.48 ± 0.05
	OCGBH	0.79	-0.60 ± 0.04	-3.7 ± 0.3	-2.59 ± 0.06

tions in the void models are from the standard model consistency functions. We present the computed p-values of these tests, p_Λ, in table 3.3. The p_Λ value is the probability that the consistency function for a given void model and the one for the standard model are computed from the same underlying distribution, or, in other words, that their differences are not statistically significant. To establish that such difference is significant, at a 3-σ confidence level, for example, the p_Λ value should be lower then approximately 0.0027. Given the listed p_Λ results, we found that the computed consistency functions in void and standard cosmologies were not significantly different. This means that galaxy evolution proceeds mostly the same, regardless of the differences in the geometry and the composition of the Universe studied here.

Chapter 4

Past lightcone densities

In this chapter we compute the relativistic number densities using the $J_{\bar{z}}$ obtained in section 3.2. By definition, the LF is the number of sources per unit luminosity, per unit comoving volume. This allows us to identify the selection functions in Eq. (3.1) as the differential comoving density of galaxies stemming from the observations, and rewrite Eq. (3.3) as

$$\psi_{\bar{z}} = \left[\frac{dN}{dV_c}\right]_{obs}(\bar{z}) = J_{\bar{z}}\, n_C(\bar{z}) = J_{\bar{z}}\, \frac{dN}{dV_c}(\bar{z}), \tag{4.1}$$

which can still be written as

$$\left[\frac{dN}{dz}\right]_{obs} = J_{\bar{z}}\, \frac{dN}{dz}, \tag{4.2}$$

since the purely geometrical term dV_c/dz cancels out in both sides of the equation. Together with Eqs. (3.3) and (1.67), Eq. (4.2) allows us to obtain the differential number counts $[dN/dz]_{obs}$ from the selection function of a given dataset in the different comoving densities $n_C(z)$ defined by the void model parametrisations considered here.

Because the quantity inside the parentheses in Eq. (1.36) is also a purely geometrical term, we can simply write,

$$[\gamma_i]_{obs}(\bar{z}) = J_{\bar{z}}\, \gamma_i(\bar{z}), \tag{4.3}$$

which allows us to obtain the observed differential densities $[\gamma_i]_{obs}$ in the lightcones of the cosmologies considered here once $J_{\bar{z}}$ is computed.

To obtain the observed integral densities $[\gamma_i^*]_{obs}(\bar{z})$ we substitute dN/dz in,

$$N(z) = \int_0^z \frac{dN}{dz}(z')\, dz'. \tag{4.4}$$

with $[dN/dz]_{obs}$ from Eq. (4.2) and compute the observed cumulative number counts $[N]_{obs}(\bar{z})$. Then we can substitute this result back in Eq. (1.46), since the cosmological distance to redshift relation $d_i(z)$ is also fixed by the geometry of the given Cosmology.

We used the observed differential and integral densities to investigate the effects of the central underdensity prescribed by the GBH models in the redshift distortions caused by the expanding spacetime on the observer's past lightcone.

Our previous studies of these relativistic number densities (Ribeiro 2005; Albani et al. 2007; Iribarrem et al. 2012) suggested a high redshift power-law behaviour for both differential and integral radial distributions. In other words, that the expansion distributes the sources along the lightcone in a self-similar manner. This is a purely geometrical effect, as discussed in Sect. 1.1 that may or may not be dominant, because the hierarchical build-up of galaxies also plays a role in how the sources distribute along the lightcone. Given that some of the alternative void models are built assuming an LTB line element instead of the standard model FLRW one, we aim in this section to better characterise those power-laws, and to investigate how they are affected by the secular evolution of the sources and by the direct effect of the expansion of the different geometries. We focused the discussion on the densities computed using the luminosity distance, since the results for the other distance definitions are all qualitatively the same.

As can be seen in Figs. 1.5 and 1.6, the geometrical effect increases with the redshift, deviating both the theoretical differential and the cumulative number densities away from a constant, homogeneous behavior at high redshifts. At redshifts lower then z $\approx$ 0.1 this geometrical effect is less pronounced, and both $\gamma_L(z)$ and $\gamma^*_L(z)$ shown follow the constant average galactic mass $\mathcal{M}$ assumed in their computation, as discussed in Sec. 3.1.

It follows that there must be a region in redshift space at which occurs a transition between the power-law behavior induced by the expansion at high redshift, and the behavior defined by the underlying density parameter $\Omega_M(z)$ combined with the evolution of the sources stemming from the LF. However, the exact size and range of this region cannot be predicted with the empirical approach for the comoving number densities used in this work. Therefore, if we are to characterize the power-law behavior of the high-redshift end of our number densities, we must allow our fitting procedure to search for the best redshift at which the power-law behavior begins to dominate.

To characterize the high redshift power-laws, we compute in an iterative way the best linear fit to the $\log \gamma_L$ vs. $\log d_L$ tables. Starting with the LF values derived for the highest three redshift bins, we perform the same fit, including in each iteration one extra LF value, in decreasing order, until we have included all

points. Then, we select the fit with the lowest reduced χ^2 value. The selected fits for the different dataset and cosmology combinations are plotted in figure 4.1. The listed uncertainties are formally obtained taking the square root of the linear term in the covariance matrix of the fitted power-law.

To quantify how significant are the differences in the slopes of the power-laws obtained, we can start by first computing the uncertainty of the difference $\Delta_{a,b}$, between the α_a slope of $\log \gamma_L$ using a given dataset/cosmology combination a and that of a different combination b as

$$\delta\Delta_{a,b} = \sqrt{(\delta\alpha_a)^2 + (\delta\alpha_b)^2}. \tag{4.5}$$

The significance of this difference in terms of its uncertainty is then obtained from $\Delta_{a,b}/(\delta\Delta_{a,b})$. Next we use the approach above to obtain comparisons between standard vs. void cosmologies, 100 μm vs. 160 μm datasets, and differential densities γ vs. integral densities γ^*.

4.1 Comparison with the LTB/CGBH models

Results for the significance of the difference between slopes of the high redshift power-law fits to the differential densities γ, and the integral densities γ^*, given a fixed cosmological model, were highly dependent on the dataset. They were fairly insignificant on the 100 μm data for all cosmologies (ΛCDM: 0.3-σ, CGBH: 0.9-σ, OCGBH: 1.1-σ); whereas they were all at least marginally significant in the 160 μm data (ΛCDM: 5.2-σ, CGBH: 3.0-σ, OCGBH: 3.4-σ).

Such differences in the slopes between the high redshift power-law fits to γ and to γ^* can be understood by checking at Eqs. (1.36), and (1.46). We note that γ is proportional to dN/dz whereas γ^* is proportional to N. Since N is a cumulative quantity, it can only increase or remain constant with increasing redshift. That is, even if there are regions in the volume where N is defined, which have a lower density of detected sources, N itself will remain constant. On the other hand, dN/dz is sensitive to such local density variations, which adds up to a higher degree of non-homogeneity in the higher redshift part of the past lightcone probed by the survey and as a consequence a steeper power-law slope of γ.

The differences between the slopes of the high redshift power-law fits to the relativistic densities computed using the 100 μm, and the 160 μm PEP blind-selected datasets were fairly insignificant when assuming the void models studied here (CGBH: 0.7-σ for γ, and 0.3 for γ^*; OCGBH: 1.3-σ for γ, and 1.0 for γ^*), whereas, those differences showed a moderate-to-strong significance if the ΛCDM model was assumed (4.6-σ for γ, and 3.0-σ for γ^*).

The differences in the slopes obtained using different datasets can be understood as the effect on the past lightcone distributions caused by different redshift-evolving luminosity limits of detection. The results above indicated that the distributions on the past lightcone of the void models were significantly less different, and therefore less affected by the detection limits of the PEP datasets, then their counterparts computed on the past lightcone of the standard model.

Finally, we computed the significance of the differences obtained by comparing the same slopes computed in two different cosmological models. The only marginally significant ($\geq$ 3-σ) difference we found is for the comparison between standard and void models, for the integral density γ^* slopes, using the 100 μm dataset: 3.7-σ for the ΛCDM vs. CGBH comparison, and 4.3-σ for the ΛCDM vs. OCGBH one. Given the striking concordance of the other γ^* slopes around a tentative value of -2.5 $\pm$ 0.1 it is possible that the oddly small values of the slope of γ^* in the 100 μm dataset and its uncertainty be an artifact caused by our fitting procedure.

How to combine the results from all of those different comparisons in a coherent picture? Iribarrem et al. (2013b) showed that the corrections needed to build the LF using a flux-limited survey rendered the results sensitive to the differences caused by changing the underlying cosmological model. Detection limits seem to play a major role in the fully-relativistic analysis used here as well. On one hand, we found significant differences caused by the kind of statistics used (γ or γ^*) with the 160 μm blind-selected catalogue. On the other hand, we found that the cosmology assumed (FLRW/ΛCDM or LTB/GBH) caused significant differences on both γ and γ^*, using the 100 μm dataset instead. Some of these discrepancies could be caused by the way we fit the power-laws to the high-redshift parts of the distributions. Future observations with lower flux limits will help us to check which of these discrepancies were caused by the present flux limits.

4.2 Comparison with other LTB models

It is important to notice that the results in Chapter 3 together with the discussion presented above, are valid only for a very special case of LTB models, namely, the parameterization for the CGBH model obtained by Zumalacárregui et al. (2012). It is not in the scope of the present work to present a complete analysis of other LTB models in the literature, which would require first recomputing the Luminosity Functions presented in Iribarrem et al. (2013b) from the start, but given some recent advancements in better exploiting the flexibility of these models, a qualitative discussion of their possible impact on our results is pertinent here.

Assuming different non-homogeneous cosmologies can affect the present analyses in three different ways. First, in terms of building the LF from the observations,

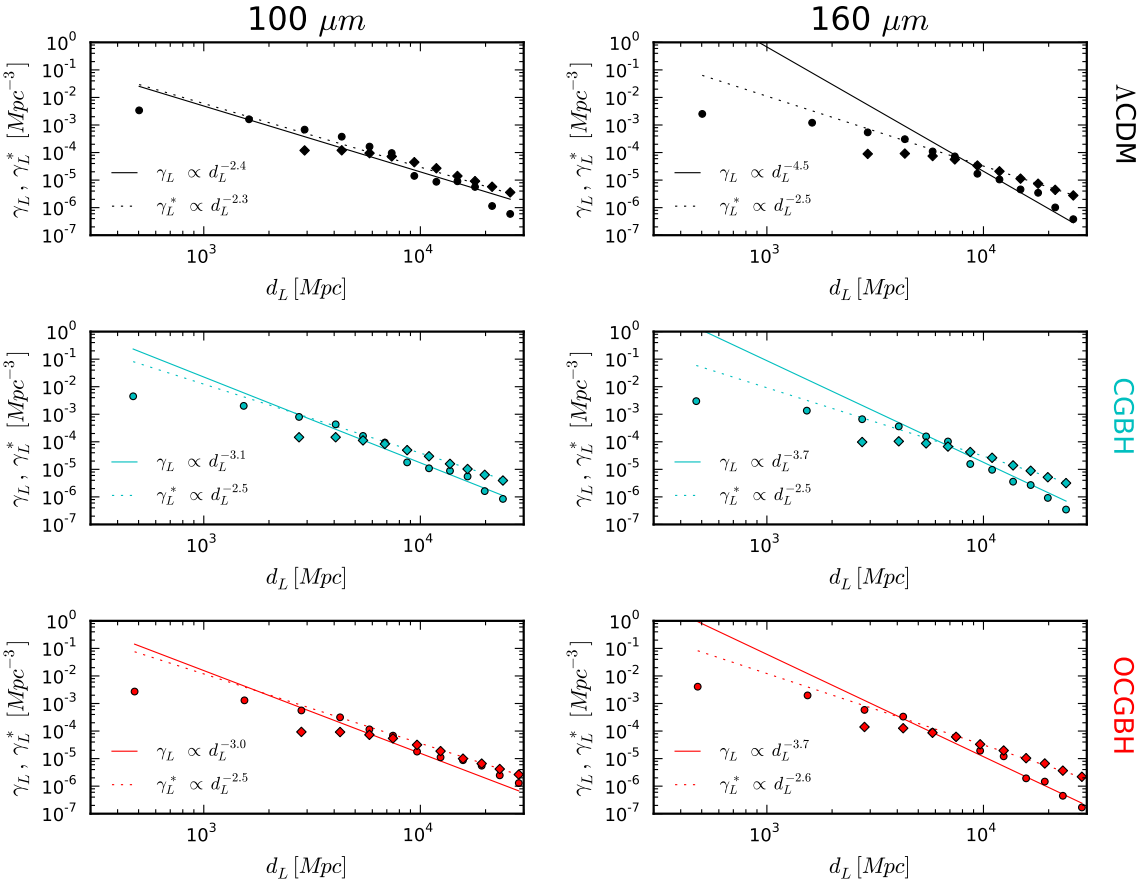

Figure 4.1: Best fit power-laws to the differential density γ_L (dots), and the integral density γ_L^* (diamonds). The left panels show the plots for the 100 μm LF, while the right ones show the plots for the 160 μm LF, in the three cosmological models / parameterisations studied here. Full lines show the best fit high redshift power-law for the differential densities, while the dashed lines show the best fit ones for the integral densities.

a model with a matter density profile $\Omega_M(r)$ different enough from the ones studied here could possibly render invalid the average homogeneity assumption at the heart of the $1/V_{max}$ LF estimator. Using mock catalogues, Iribarrem et al. (2013b) shows that the void shapes of the CGBH models used in their LF does not affect significantly the ability of the $1/V_{max}$ estimator of recovering the underlying LF.

Second, different distance-to-redshift relations could also affect the LF results, and thus its redshift evolution, through the computation of the maximum observable redshift of each source z_{max}, which is used in the computation of the $1/V_{max}$ value of the LF in each redshift bin. As discussed in Iribarrem et al. (2013b), this comes as a result of the fainter part of the galaxies in a survey having fluxes near the limit of observation in the field, and is affected mainly by differences in the luminosity distance-to-redshift relation. Also, at luminosities $L \approx L^*$, the z_{max} of the sources is safely hitting the higher z limit of the redshift bin, rendering their volume correction independent of their luminosity, and thus, of the $d_L(z)$ relation.

Finally, the expected number densities in the past-lightcone γ_i and γ_i^*, as computed in Sect. 1.2.3 are both sensitive to the distance-to-redshift relations, as shown in Figs. 1.5 and 1.6. The differences caused on the number densities by the different distance relations might be large enough to be detected, given the observational uncertainties stemming from the LF. Considering the present results, such differences in the expected number densities should be larger then the CGBH-to-FLRW ones studied here, if we were to detect a significant effect on the observed number densities due to their expected values alone.

February et al. (2010) argue that CMB and BAO constraints may be significantly distorted by differences in the evolution of primordial perturbations caused by the curvature inside the voids. They go on to fit a number of different shapes for the inner matter profile, considering only local Universe data, namely, SNe Ia and the reconstruction of $H(z)$ through passively evolving galaxies. They show that all their models mimic the FLRW $d_L(z)$ to sub-percent level, which should render the changes on the maximum redshift estimates and on the expected number densities caused by assuming such models comparable to the ones we observe here.

The authors show in their Fig. 9 that up to redshift $z \approx 1$, their best fit models follow very closely the distance modulus, and thus the $d_L(z)$ relation, of ΛCDM. Looking at the same plot, we can see that the luminosity distances grow increasingly smaller when compared to their standard model counterparts at higher redshifts. Looking at Eq. (1.34), we can expect that this could potentially lead to higher values of γ^* and, consequentially, a smaller value for its best fit power-law.

Also, their best fit voids are much larger then the ones used here, as can be seen by comparing the upper left panel of their Fig. 7 versus the upper panel of Fig. 1 in Iribarrem et al. (2013b), which shows the best fit voids of Zumalacárregui et al.

(2012). Mock catalogue tests should be used to make sure these larger voids don't bias the $1/V_{max}$ method used here. However, as argued in Iribarrem et al. (2013b), if the large underdense profiles used here varied smoothly enough not to significantly bias the LF estimator, we don't expect that the larger voids of February et al. (2010) will.

Clarkson & Regis (2011) discuss the implications of allowing for inhomogeneity in the early time radiation field and how it affects the constraining power of CMB results for inhomogeneous models. They show, for example, that even models that are asymptotically flat at the CMB, can be made to fit if the matter density profile includes a low density shell around the central void. An underdense shell like this could possibly lead the $1/V_{max}$ method to over-estimate the volume correction of sources with maximum observable comoving volume inside or beyond the shell, because such corrections are based on the assumption of an average homogeneous distribution. To test in detail how accurately would this LF estimator recover the underlying distribution we would need to build mock catalogues that assume the matter distribution of these models, but we expect that such differences, if present, would show more prominently at mid- to high redshift, according to the size of the shell, and make the faint-end slope steeper by assigning higher over-corrections to the fainter sources. Depending on how non-homogeneous the matter profile is, an over-estimation of the characteristic number density parameter ϕ^* might also be detected.

Varying bang-time functions $t_{bb}(r)$ were also studied (Clifton et al. 2009) and shown to be an extra degree of freedom that helps LTB models to reconciliate with CMB + H_0 constraints. Bull et al. (2012) however, show that models with varying $t_{bb}(r)$ constrained by the combination of SNe + CMB + H_0 should produce a kinetic Sunyaev-Zel'dovich effect which is orders of magnitude stronger then its expected upper limits. It is not clear how allowing for this extra degree of freedom would change the key quantities shown to affect our results: the $d_L(z)$ and $r(z)$ relations, and the shape of the central underdense region. Only a full-fledge analysis, starting from the building up of the LF, assuming a model with a varying bang-time fit by the observations would allow us to make any reasonable comparison with the results presented in this work.

Conclusions

In this work we aimed at studying the redshift evolution of the comoving and relativistic number densities obtained from the FIR Luminosity Functions for the PEP survey blind selected catalogues. In our analyses, we compared the results from the LFs computed assuming the standard FLRW/ΛCDM and the void LTB/CGBH cosmological models, both fit by the combination of SNe + CMB + BAO observations.

In Chapter 1 we derived the theoretical results needed to compute the differential and integral densities along the past lightcone of FLRW and LTB dust models. We applied these results to compute the theoretical predictions for such quantities in the CGBH parametrisations of Zumalacárregui et al. (2012).

In Chapter 2 we have computed the far-IR luminosity functions for sources in the PEP survey, observed at the Herschel/PACS 100 and 160 μm bands. We computed both monochromatic and total IR luminosities assuming both the ΛCDM standard and GBH void cosmological models, with the aim of assessing how robust the luminosity functions are under a change of observationally constrained cosmologies.

We concluded that the current observational constraints imposed on any cosmological model by the combined set of SNe + CMB + BAO results are enough to yield robust estimates for the evolution of FIR characteristic luminosities L^* and number densities, ϕ^*.

We found, however, that estimations of the faint-end slope of the LF are still significantly dependent on the underlying cosmological model assumed, despite the above-mentioned observational constraints. In other words, if there is indeed an underdense region around the Milky Way, as predicted by the GBH models, causing the effective metric of the Universe at Gpc scale to be better fit by an LTB line element, then assuming the spatial homogeneous ΛCDM model in the computation of the LF would yield an over-estimated number density of faint galaxies, at least at lower redshifts (up to $z \approx 0.4$).

The characteristic number density and the characteristic luminosity parameters of the FIR luminosity functions derived here are made robust by the present constraints on the cosmological model. The faint-end slope, however, still shows significant differences among the cosmologies studied here.

We showed that these differences are caused mainly by slight discrepancies in the luminosity distance - redshift relation, still allowed by the observations. The $1/V_{max}$ methodology studied here is a necessary way to compute the LF using a flux-limited survey like PEP. This methodology, as we showed, is not biased by the kind of under-dense regions proposed by the alternative cosmologies studied here. On the other hand, the necessary volume corrections intrinsic to the method are still dependent enough on the underlying assumptions about the geometry and expansion rate of the Universe at Gpc scale to yield significant ($\approx$ 3-σ) discrepancies in their results. In other words, the systematic dispersion in the values of the low luminosity LF points, caused by the (arguably still) remaining degree of freedom in the choice of the underlying cosmological model, combined with the current flux limits, is still significantly larger than the statistic uncertainty assumed in the computation of the error bars of those points, causing the differences in the LF values to be larger than the combination of their computed uncertainties.

Surveys with lower flux limits would allow lower FIR-luminosity sources to be fully accounted for, reducing the marginally significant dependency of the FIR LF on the cosmological model still detected here.

In Chapter 3 we computed the selection functions stemming from the far-IR LFs of Iribarrem et al. (2013b), which allowed us to establish at an over 5-σ confidence level that geometry alone is not able to fit their behaviour. This finding confirms the need to allow for evolution of the sources (either in number or in luminosity) in these void models as well. We found no strong evidence for a dependence of this evolution on the cosmological models studied here. In other words, the combined merger tree and barionic processes needed to reproduce the redshift evolution of the FIR LF in the GBH void models are not significantly different from the hierarchical build up and astrophysical processes in the standard model.

Finally, in Chapter 4 we computed the observed differential and integral densities in the past lightcone of both standard and void cosmologies, and fitted their high redshift *observational non-homogeneities* using power-laws. We show that the systematic dependency of the LF methodology on the cosmology that was discussed in Iribarrem et al. (2013b) could still lead to significant differences on these relativistic number densities. The integral densities showed a somewhat consistent slope across all combinations of blind-selected datasets and cosmological models studied here. On the other hand, the differential densities were found to be sensible to a change in the cosmological model assumed in their computation. These results confirmed the power-law behavior of the galaxy distribution on the observer's past lightcone of the LTB/GBH models and allowed to obtain a tentative value of -2.5 $\pm$ 0.1 for the power-law index of the cumulative radial statistics γ_i^* of this distribution, regardless of the cosmological model assumed.

Appendix A

Mock catalogues

In this appendix we test whether the $1/V_{max}$ LF estimator is reliable in studying Gpc scale voids like the ones predicted by the GBH models, embedded in an LTB dust model. We follow the general approach by Takeuchi et al. (2000) who made use of mock catalogues built assuming, in the case of the void distribution, a (non-central and small) void with a radius of 1.6 Mpc at a distance of 0.8 Mpc, and at a limiting redshift of $z = 0.1$. Our mock catalogues are built using different distributions as predicted by the GBH models, and as shown in figure 1.1. Also, the redshift range of our interest is 4 times larger, since it is in the interval $\Delta z = [0.01, 0.4]$ that we fit the faint-end slope of the luminosity functions.

Mock catalogues are built reproducing the detection limits and SED distributions in the GOODS-S and COSMOS fields, in the PACS 100 and 160 μm filters, as listed in Gruppioni et al. (2013). We chose those two fields for better representing the whole of the data used in this work: GOODS-S is the field with the lowest flux limits in the PEP survey, while COSMOS is the one with the widest effective area.

Naïvely one might decide to use matter density profiles in figure 1.1 to randomly assign comoving distances to the sources in the mock catalogue. However, given the large redshift interval we aim to cover in our simulations, the redshift evolution of the density profiles must be fully considered.

For each of the present time, rest-frame (z=0) matter density profile, $\Omega_{_M}(r)$, defined in a constant time coordinate hipersurface, and predicted by both the standard model and the void models (see figure 1.1), we compute the corresponding redshift evolution, $\Omega_{_M}(z)$, defined in the past light-cone of the same cosmological model. In the FLRW spacetime, the dimensionless density parameters $\Omega_{_M}$ and $\Omega_{_M}(z)$ are related as follows:

$$\Omega_{_M}(z) = \Omega_{_M} \left[\frac{H_0}{H(z)}\right]^2 a(z)^{-3}, \tag{A.1}$$

where $H(z)$ is the Hubble parameter at redshift z, carried over from the definition of the critical density $\rho_c = 3H_0^2/8\pi G$, and $a(z)$ the scale factor, both as functions

of the redshift. Similarly, following the definition of $\Omega_M(r)$ used in GBH and Zumalacárregui et al. (2012), one may write an analogue equation in the void-LTB models as,

$$\Omega_M(z) = \Omega_M[r(z)] \left\{ \frac{H_{\perp 0}[r(z)]}{H_\perp[t(z), r(z)]} \right\}^2 a_\perp[t(z), r(z)]^{-3}, \tag{A.2}$$

where $H_\perp[t(z), r(z)]$ and $a_\perp[t(z), r(z)]$ are now the transverse Hubble parameter and scale factor, respectively. Figure A.1 shows the redshift evolution of the density parameters in the three models considered in the present work. Note, however, that there's an ambiguity in the definition of equation (A.2), due to the fact that the LTB geometry possesses radial expansion rate and scale factor that are in general different from their transverse counterparts. For the purpose of building mock catalogues that are consistent with the void-LTB parametrisations used in this work, the transverse quantities are the ones to be used, because that was the one used in Zumalacárregui et al. (2012), from where the best fit parameters used in this work were derived.

Next, we randomly assign redshifts using a probability distribution based on the one of those $\Omega_M(z)$ profiles, rest-frame luminosities based on a same Schechter LF with parameters $L^*=10^{11}$ $L_\odot$, $\phi^*=10^{-3}$ $dex^{-1}.Mpc^{-3}$ and α = -1/2 and a typical empirical SED from the Poletta templates, drawn from the same distributions reported in Gruppioni et al. (2013). In this way, we can test first the validity of the $1/V_{max}$ estimator itself for the purposes of the present work, and second, the possible effects of the different predicted density profiles on the values recovered of the LF.

Having assigned a redshift, a luminosity and a SED for each Monte Carlo (MC) realisation, we proceed to compute k-corrections and fluxes, using the luminosity distance-redshift relation consistent with the density parameter in each cosmology. We include the source in the mock catalogue if its observed flux is larger than the detection limit of the field. We repeat such process until we have a catalogue with a number of selected MC realisations equal to the number of sources in the redshift interval $\Delta z = [0.01, 0.4]$, for a given field.

We then compute the $1/V_{max}$ LF following the same methodology described in §2.3, using 100 mock catalogues built as above. To assess the goodness-of-fit of the $1/V_{max}$ LF versus the input Schechter profile, we compute the one-sided Kolmogorov-Smirnov (KS) statistic of the normalised residuals against a Gaussian with zero mean and unit variance. We plot the estimation of the LF using the mock catalogues against the input Schechter LF in figures A.2, A.3, and A.4. The KS statistic for each mock/input comparison is listed between parentheses, in the plots.

We find that the density profiles of interest don't change significantly the LF results, as can be seen by comparing different panels in a same figure. We note what appears to be a general bias towards under-estimating the characteristic luminosity L^*, in agreement with Smith (2012) results.

Comparison between the $1/V_{max}$ LF results for the GOODS-S mocks built using either the present time density profiles (figure A.2) or the proper redshift evolution of those (figure A.3), shows that the method successfully takes into consideration the redshift distortion in the matter distribution, yielding points in both cases that recover the input LF profile qualitatively close in respect to each other, from the point of view of the KS statistic. However, the $1/V_{max}$ estimator significantly underestimates the LF in lower luminosity bins. This effect, however, is found on all cosmologies studied in this paper, and cannot therefore account for the significant difference in the LF faint-end slopes reported in §2.4.

Comparison between the mocks for the GOODS-S and COSMOS fields built using the redshift evolution of the density parameter in the different cosmological models shows the $1/V_{max}$ estimator fares slightly better in the deeper GOODS-S field, as compared to the wider COSMOS one.

Summing up, even if the method is not perfectly robust under a change in the cosmological model, the variations caused by a change in the underlying cosmology in the results obtained with the $1/V_{max}$ estimator are not enough to explain the differences in the shape of the LF at the considered redshift interval, $\Delta z = [0.01, 0.4]$.

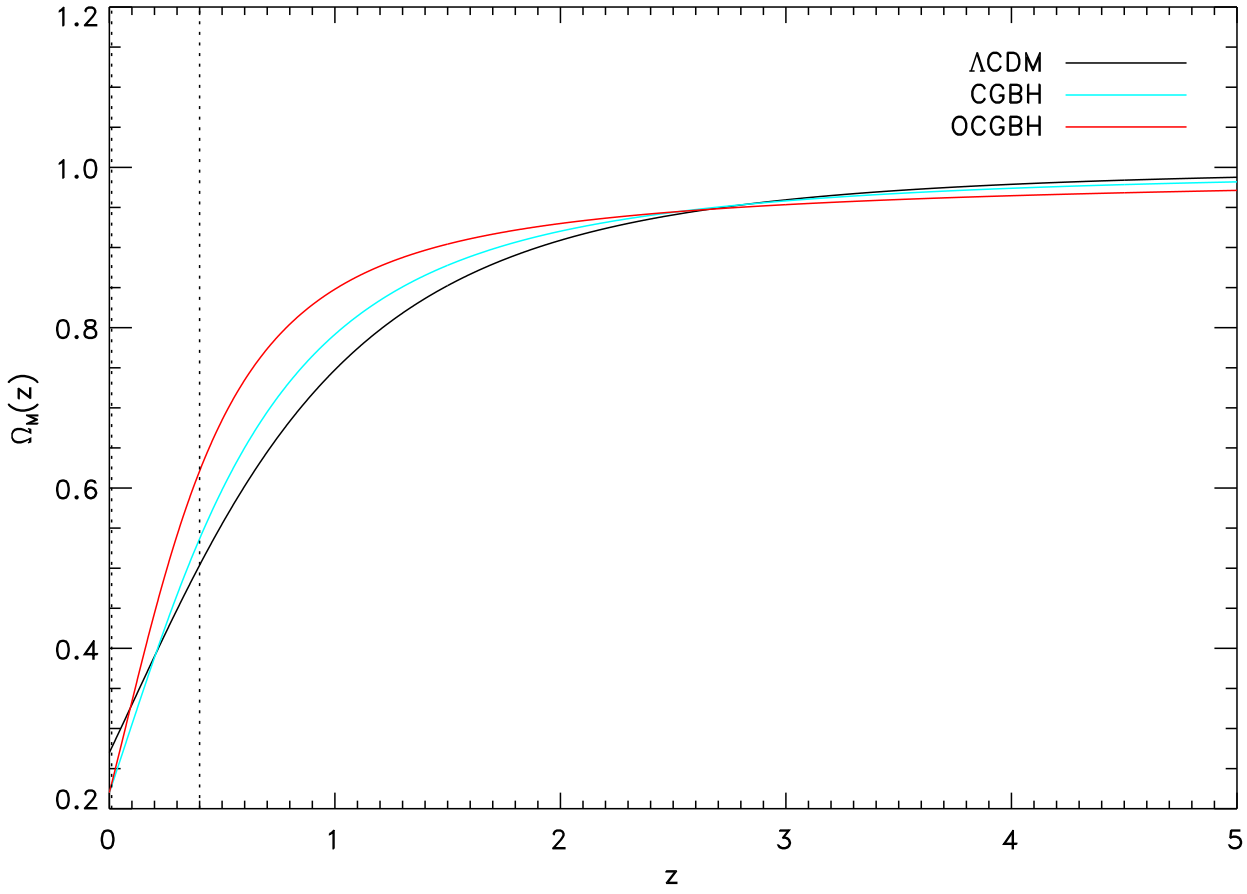

Figure A.1: Redshift evolution of the dimensionless matter density parameters in the standard (ΛCDM) and the void (GBH) cosmological models. The dotted vertical lines delimit the lowest redshift interval considered in the computation of the LF, at which the faint-end slopes are fit.

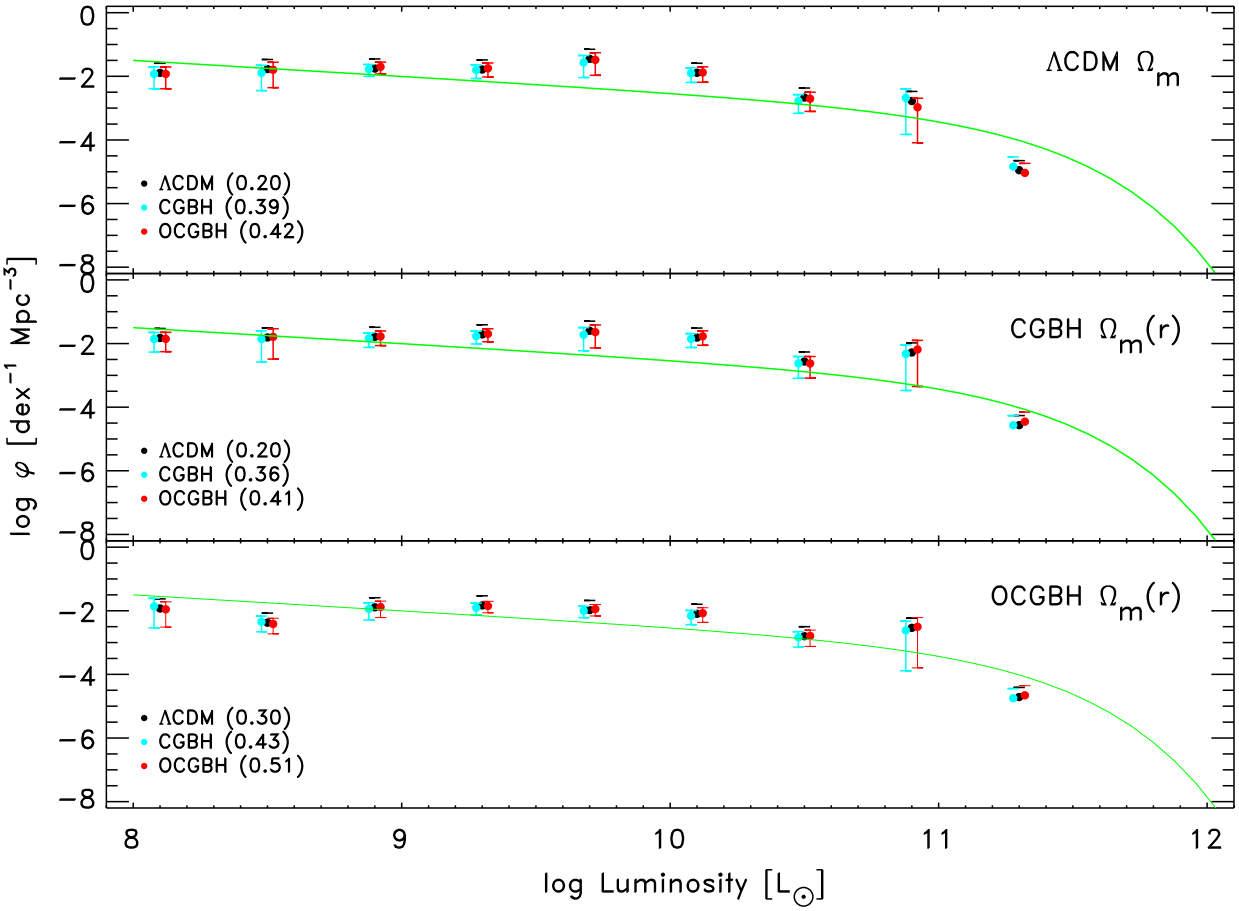

Figure A.2: Results for the $1/V_{max}$ LF estimator, computed from mock catalogues assuming a constant density profile $\Omega_M = 0.27$ (ΛCDM), and the underdense profiles of equation (1.61) for the GBH void models (figure 1.1). Sources luminosities in the mock catalogue are drawn from the Schechter LF (here shown in green dashed line, with parameters $L^*=10^{11}$ $L_\odot$, $\varphi^*=10^{-3}$ $dex^{-1}.Mpc^{-3}$ and α = -1/2). Flux limits and SED are taken from the results of Gruppioni et al. (2013) for the PEP survey dataset in the GOODS-S field.

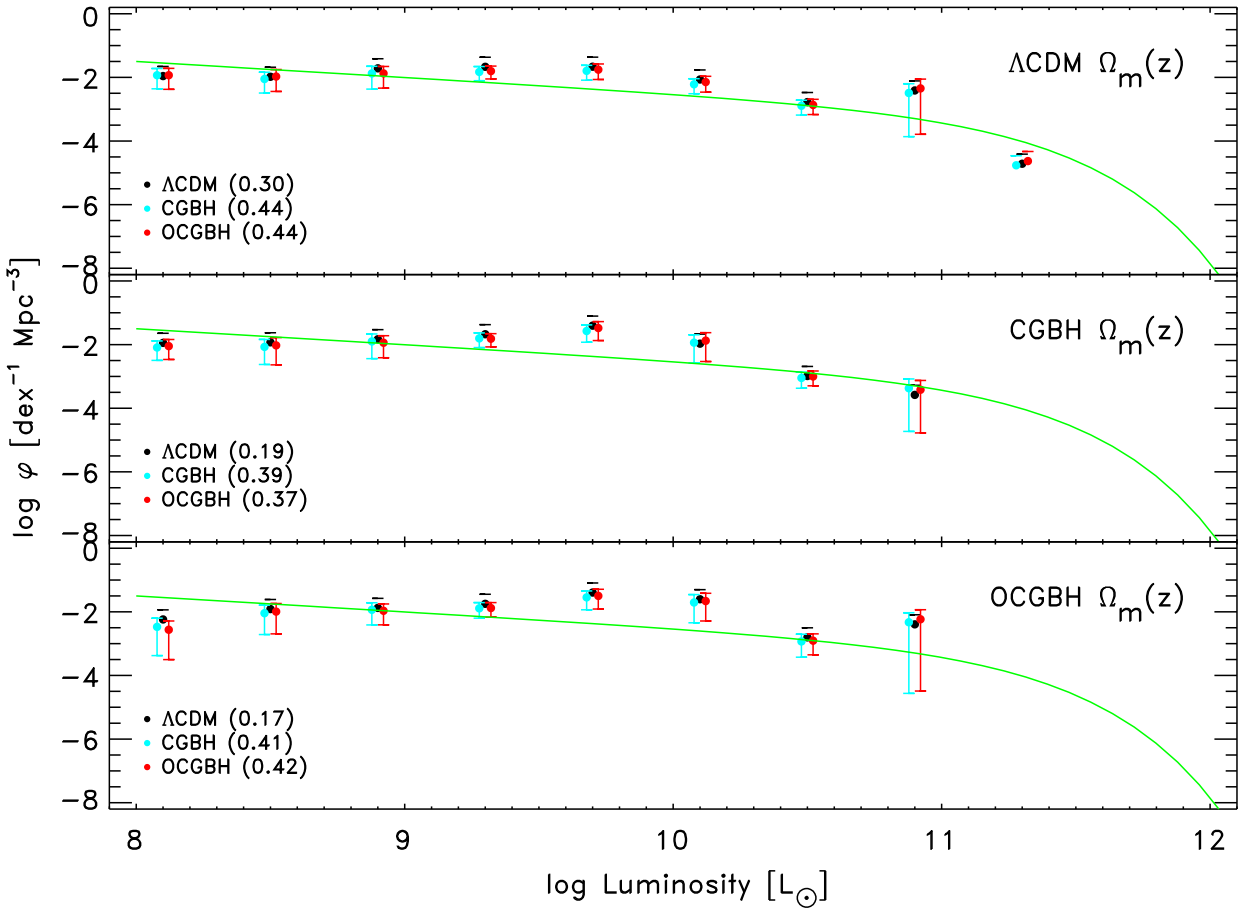

Figure A.3: Same as Figure A.2 but assuming the redshift evolution of the matter density profiles in both the standard (ΛCDM), and the void-LTB models as in Figure A.1.

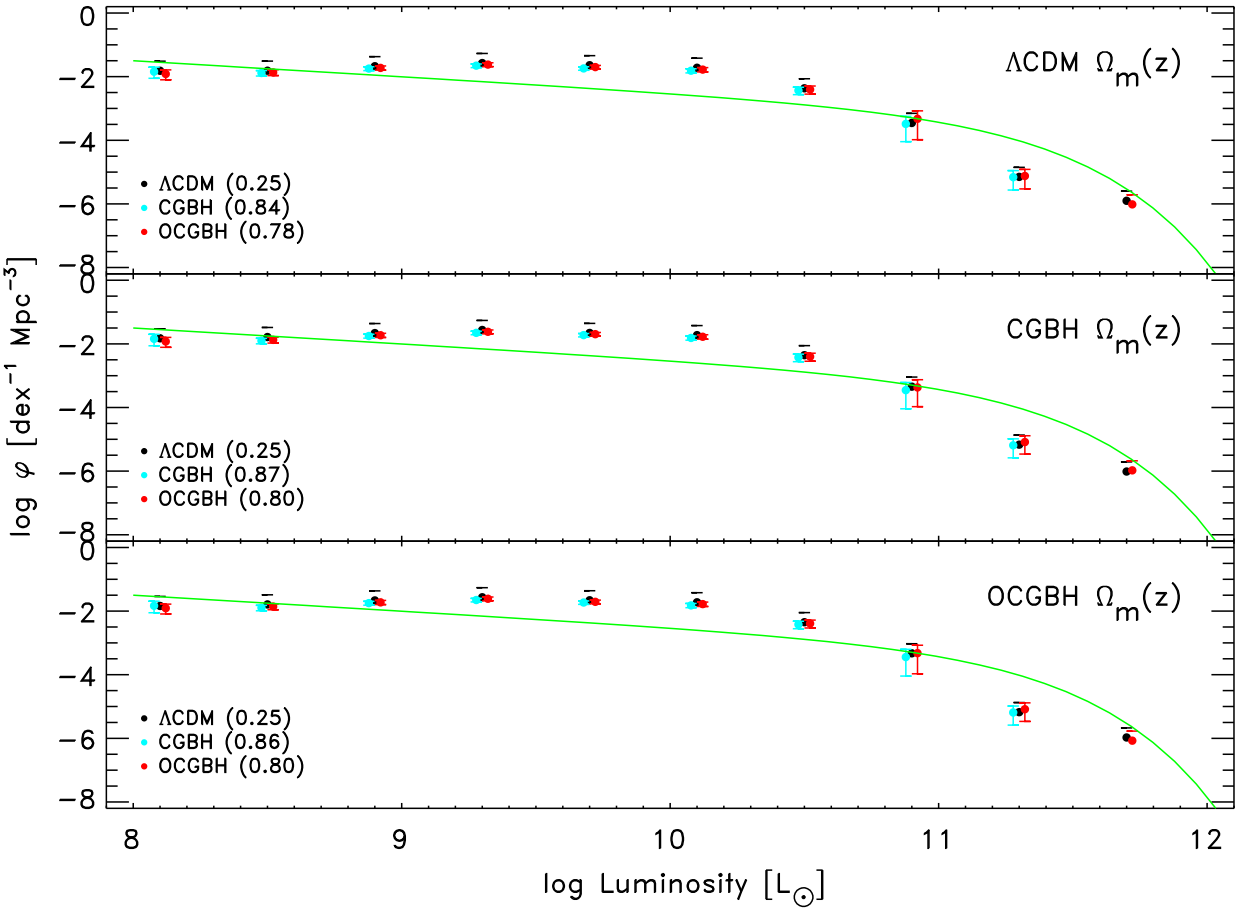

Figure A.4: Same as Figure A.3 but for the PEP survey dataset in the COSMOS field.

Bibliography

Albani, V. V. L., **Iribarrem, A. S.**, Ribeiro, M. B., & Stoeger, W. R. 2007, ApJ, 657, 760

Alfedeel, A. H. A. & Hellaby, C. 2010, General Relativity and Gravitation, 42, 1935

Arnouts, S., Cristiani, S., Moscardini, L., et al. 1999, MNRAS, 310, 540

Avni, Y. & Bahcall, J. N. 1980, ApJ, 235, 694

Babbedge, T. S. R., Rowan-Robinson, M., Vaccari, M., et al. 2006, MNRAS, 370, 1159

Benson, A. J., Bower, R. G., Frenk, C. S., et al. 2003, ApJ, 599, 38

Berta, S., Magnelli, B., Lutz, D., et al. 2010, A&A, 518, L30

Berta, S., Magnelli, B., Nordon, R., et al. 2011, A&A, 532, A49

Béthermin, M., Daddi, E., Magdis, G., et al. 2012, ApJ, 757, L23

Blanton, M. R. & Roweis, S. 2007, AJ, 133, 734

Bolejko, K., Célérier, M.-N., & Krasiński, A. 2011a, Classical and Quantum Gravity, 28, 164002

Bolejko, K., Hellaby, C., & Alfedeel, A. H. A. 2011b, J. Cosmology Astropart. Phys., 9, 11

Bondi, H. 1947, MNRAS, 107, 410

Bonnor, W. B. 1972, MNRAS, 159, 261

Boylan-Kolchin, M., Bullock, J. S., & Kaplinghat, M. 2012, MNRAS, 2657

Boylan-Kolchin, M., Springel, V., White, S. D. M., Jenkins, A., & Lemson, G. 2009, MNRAS, 398, 1150

Bull, P. & Clifton, T. 2012, Phys. Rev. D, 85, 103512

Bull, P., Clifton, T., & Ferreira, P. G. 2012, Phys. Rev. D, 85, 024002

Busti, V. C. & Lima, J. A. S. 2012, MNRAS, L504

Caputi, K. I., Lagache, G., Yan, L., et al. 2007, ApJ, 660, 97

Célérier, M.-N. 2007, New Advances in Physics, 1, 29

Chary, R. & Elbaz, D. 2001, ApJ, 556, 562

Chávez, R., Terlevich, E., Terlevich, R., et al. 2012, MNRAS, 425, L56

Clarkson, C., Ellis, G., Larena, J., & Umeh, O. 2011, Rept. Prog. Phys., 74, 112901

Clarkson, C., Ellis, G. F. R., Faltenbacher, A., et al. 2012, MNRAS, 426, 1121

Clarkson, C. & Regis, M. 2011, J. Cosmology Astropart. Phys., 2, 13

Clarkson, C. & Umeh, O. 2011, Classical and Quantum Gravity, 28, 164010

Clifton, T., Ferreira, P. G., & Zuntz, J. 2009, J. Cosmology Astropart. Phys., 7, 29

Clifton, T., Rosquist, K., & Tavakol, R. 2012, Phys. Rev. D, 86, 043506

Conde-Saavendra, G., **Iribarrem, A.**, & Ribeiro, M. B. 2013, Physica A, submitted

Cool, R. J., Eisenstein, D. J., Kochanek, C. S., et al. 2012, ApJ, 748, 10

de Putter, R., Verde, L., & Jimenez, R. 2012, ArXiv e-prints, astro-ph.CO 1208.4534

Elbaz, D., Cesarsky, C. J., Chanial, P., et al. 2002, A&A, 384, 848

Ellis, G. F. R. 1971, in General Relativity and Cosmology, ed. R. K. Sachs, 104–182, reprinted in Gen. Rel. Grav., 41, 581, 2009

Ellis, G. F. R. 2007, General Relativity and Gravitation, 39, 1047

Ellis, G. F. R. 2011, Classical and Quantum Gravity, 28, 164001

Ellis, G. F. R., Nel, S. D., Maartens, R., Stoeger, W. R., & Whitman, A. P. 1985, Phys. Rep., 124, 315

Enqvist, K. & Mattsson, T. 2007, J. Cosmology Astropart. Phys., 2, 19

Etherington, I. M. H. 1933, Philosophical Magazine, 15, 761, reprinted in Gen. Rel. Grav., 39, 1055, 2007

February, S., Larena, J., Smith, M., & Clarkson, C. 2010, MNRAS, 405, 2231

Flender, S. F. & Schwarz, D. J. 2012, Phys. Rev. D, 86, 063527

Fleury, P., Dupuy, H., & Uzan, J.-P. 2013, Physical Review Letters, 111, 091302

Franceschini, A., Aussel, H., Cesarsky, C. J., Elbaz, D., & Fadda, D. 2001, A&A, 378, 1

Freedman, W. L., Madore, B. F., Gibson, B. K., et al. 2001, ApJ, 553, 47

Gabasch, A., Bender, R., Seitz, S., et al. 2004, A&A, 421, 41

Gabasch, A., Hopp, U., Feulner, G., et al. 2006, A&A, 448, 101

Garcia-Bellido, J. & Haugbølle, T. 2008, J. Cosmology Astropart. Phys., 4, 3

Grazian, A., Fontana, A., de Santis, C., et al. 2006, A&A, 449, 951

Griffin, M. J., Abergel, A., Abreu, A., et al. 2010, A&A, 518, L3

Gruppioni, C., Pozzi, F., Andreani, P., et al. 2010, A&A, 518, L27

Gruppioni, C., Pozzi, F., Rodighiero, G., et al. 2013, MNRAS, 432, 23

Gruppioni, C., Pozzi, F., Zamorani, G., & Vignali, C. 2011, MNRAS, 416, 70

Heinis, S., Buat, V., Béthermin, M., et al. 2013, MNRAS, 429, 1113

Hellaby, C. 2012, J. Cosmology Astropart. Phys., 1, 43

Hellaby, C. & Alfedeel, A. H. A. 2009, Phys. Rev. D, 79, 043501

Hogg, D. W., Baldry, I. K., Blanton, M. R., & Eisenstein, D. J. 2002, ArXiv Astrophysics e-prints, astro-ph/0210394

Hoyle, B., Tojeiro, R., Jimenez, R., et al. 2013, ApJ, 762, L9

Hubble, E. 1929, Proceedings of the National Academy of Science, 15, 168

Humphreys, N. P., Maartens, R., & Matravers, D. R. 2012, General Relativity and Gravitation, 44, 3197

Ilbert, O., Arnouts, S., McCracken, H. J., et al. 2006, A&A, 457, 841

Ilbert, O., Tresse, L., Arnouts, S., et al. 2004, MNRAS, 351, 541

Iribarrem, A., Andreani, P., February, S., et al. 2013a, A&A, submitted

Iribarrem, A., Andreani, P., Gruppioni, C., et al. 2013b, A&A, 558, A15

Iribarrem, A. S. 2009, Master's thesis, Observatório do Valongo, Universidade Federal do Rio de Janeiro

Iribarrem, A. S., Lopes, A. R., Ribeiro, M. B., & Stoeger, W. R. 2012, A&A, 539, A112

Johnston, R. 2011, A&A Rev., 19, 41

Kennicutt, Jr., R. C. 1998, ApJ, 498, 541

Klypin, A., Kravtsov, A. V., Valenzuela, O., & Prada, F. 1999, ApJ, 522, 82

Komatsu, E., Dunkley, J., Nolta, M. R., et al. 2009, ApJS, 180, 330

Komatsu, E., Smith, K. M., Dunkley, J., et al. 2011, ApJS, 192, 18

Lagache, G., Dole, H., Puget, J.-L., et al. 2004, ApJS, 154, 112

Lin, H., Yee, H. K. C., Carlberg, R. G., et al. 1999, ApJ, 518, 533

Liu, G., Lu, Y., Chen, X., et al. 2012, ApJ

Lopes, A. R., **Iribarrem, A.**, Ribeiro, M. B., & Stoeger, W. R. 2013, A&A, submitted

Lutz, D., Poglitsch, A., Altieri, B., et al. 2011, A&A, 532, A90

Magnelli, B., Elbaz, D., Chary, R. R., et al. 2009, A&A, 496, 57

Magnelli, B., Elbaz, D., Chary, R. R., et al. 2011, A&A, 528, A35

Markwardt, C. B. 2009, in Astronomical Society of the Pacific Conference Series, Vol. 411, Astronomical Data Analysis Software and Systems XVIII, ed. D. A. Bohlender, D. Durand, & P. Dowler, 251

Marra, V. & Pääkkönen, M. 2010, J. Cosmology Astropart. Phys., 12, 21

Metcalfe, L., Kneib, J.-P., McBreen, B., et al. 2003, A&A, 407, 791

Meures, N. & Bruni, M. 2012, MNRAS, 419, 1937

Moore, B., Ghigna, S., Governato, F., et al. 1999, ApJ, 524, L19

Moré, S. 1978, in Lecture Notes in Mathematics, Berlin Springer Verlag, Vol. 630, Lecture Notes in Mathematics, Berlin Springer Verlag, ed. G.A. Watson, 105–116

Moresco, M., Cimatti, A., Jimenez, R., et al. 2012, J. Cosmology Astropart. Phys., 8, 6

Moss, A., Zibin, J. P., & Scott, D. 2011, Phys. Rev. D, 83, 103515

Mustapha, N., Hellaby, C., & Ellis, G. F. R. 1997, MNRAS, 292, 817

Neistein, E. & Weinmann, S. M. 2010, MNRAS, 405, 2717

Nishikawa, R., Yoo, C.-M., & Nakao, K.-i. 2012, Phys. Rev. D, 85, 103511

Oliver, S. J., Bock, J., Altieri, B., et al. 2012, MNRAS, 424, 1614

Papastergis, E., Cattaneo, A., Huang, S., Giovanelli, R., & Haynes, M. P. 2012, ApJ, 759, 138

Patel, H., Clements, D. L., Vaccari, M., et al. 2013, MNRAS, 428, 291

Peebles, P. J. E. & Nusser, A. 2010, Nature, 465, 565

Percival, W. J., Reid, B. A., Eisenstein, D. J., et al. 2010, MNRAS, 401, 2148

Pérez-González, P. G., Rieke, G. H., Egami, E., et al. 2005, ApJ, 630, 82

Perlmutter, S., Aldering, G., Goldhaber, G., et al. 1999, ApJ, 517, 565

Pilbratt, G. L., Riedinger, J. R., Passvogel, T., et al. 2010, A&A, 518, L1

Planck Collaboration, Ade, P. A. R., Aghanim, N., et al. 2013, astro-ph.CO: 1303.5090

Plebański, J. & Krasiński, A. 2006, An Introduction to General Relativity and Cosmology

Poglitsch, A., Waelkens, C., Geis, N., et al. 2010, A&A, 518, L2

Polletta, M., Tajer, M., Maraschi, L., et al. 2007, ApJ, 663, 81

Press, W. H. & Schechter, P. 1974, ApJ, 187, 425

Ramos, B. H. F., Pellegrini, P. S., Benoist, C., et al. 2011, AJ, 142, 41

Rangel Lemos, L. J. & Ribeiro, M. B. 2008, A&A, 488, 55

Regis, M. & Clarkson, C. 2012, General Relativity and Gravitation, 44, 567

Reid, B. A., Samushia, L., White, M., et al. 2012, MNRAS, 426, 2719

Ribeiro, M. B. 1992, ApJ, 388, 1

Ribeiro, M. B. 2005, A&A, 429, 65

Ribeiro, M. B. & Stoeger, W. R. 2003, ApJ, 592, 1

Richter, P. H. 1995, Telecommunications and Data Acquisition Progress Report, 122, 107

Riess, A. G., Filippenko, A. V., Challis, P., et al. 1998, AJ, 116, 1009

Rodighiero, G., Vaccari, M., Franceschini, A., et al. 2010, A&A, 515, A8

Roos, M. 1994, Introduction to cosmology (Chichester: Wiley)

Santini, P., Rosario, D. J., Shao, L., et al. 2012, A&A, 540, A109

Saunders, W., Rowan-Robinson, M., Lawrence, A., et al. 1990, MNRAS, 242, 318

Schechter, P. 1976, ApJ, 203, 297

Schmidt, M. 1968, ApJ, 151, 393

Simpson, C., Rawlings, S., Ivison, R., et al. 2012, MNRAS, 421, 3060

Skibba, R. A. & Sheth, R. K. 2009, MNRAS, 392, 1080

Smith, R. E. 2012, MNRAS, 426, 531

Sollerman, J., Mörtsell, E., Davis, T. M., et al. 2009, ApJ, 703, 1374

Sparke, L. S. & Gallagher, III, J. S. 2000, Galaxies in the universe : an introduction (Cambridge, UK: Cambridge University Press)

Springel, V., White, S. D. M., Jenkins, A., et al. 2005, Nature, 435, 629

Stefanon, M. & Marchesini, D. 2013, MNRAS, 429, 881

Takeuchi, T. T., Yoshikawa, K., & Ishii, T. T. 2000, ApJS, 129, 1

Tikhonov, A. V. & Klypin, A. 2009, MNRAS, 395, 1915

Tsujikawa, S. 2010, in Lecture Notes in Physics, Berlin Springer Verlag, Vol. 800, Lecture Notes in Physics, Berlin Springer Verlag, ed. G. Wolschin, 99–145

Valkenburg, W., Marra, V., & Clarkson, C. 2012, ArXiv e-prints, astro-ph.CO 1209.4078

van der Burg, R. F. J., Hildebrandt, H., & Erben, T. 2010, A&A, 523, A74

Wang, H. & Zhang, T.-J. 2012, ApJ, 748, 111

Weinberg, S. 1989, Reviews of Modern Physics, 61, 1

Wiegand, A. & Schwarz, D. J. 2012, A&A, 538, A147

Xu, C., Lonsdale, C. J., Shupe, D. L., O'Linger, J., & Masci, F. 2001, ApJ, 562, 179

Yang, X., Mo, H. J., & van den Bosch, F. C. 2003, MNRAS, 339, 1057

Zehavi, I., Zheng, Z., Weinberg, D. H., et al. 2011, ApJ, 736, 59

Zhang, P. & Stebbins, A. 2011, Physical Review Letters, 107, 041301

Zibin, J. P. 2011, Phys. Rev. D, 84, 123508

Zumalacárregui, M., García-Bellido, J., & Ruiz-Lapuente, P. 2012, J. Cosmology Astropart. Phys., 10, 9